Republic of Iraq

Ministry of Higher Education and

Scientific Research

University of Babylon

Faculty of Materials Engineering

Department of Metallurgical Engineering

Surface Modification of 2101 Lean Duplex Stainless Steel for Biomedical Applications

A Thesis Submitted to the Council of the Faculty of Materials Engineering /University of Babylon in Partial Fulfillment of the Requirements for the Degree of Doctor of Philosophy in Materials Engineering/ Metallurgical Engineering

By

Nesreen Dakhel Fahad Delli

Supervised by

Prof.Dr.Jassim Mohammed Salman **Prof.Dr.Ali Sabea Hammood**

2021 A.D. **1442 A.H.**

بسم الله الرحمن الرحيم

يرفع الله الذين آمنوا منكم والذين

أوتوا العلم درجات

صدق الله العلي العظيم

(سورة المجادلة :الآية 11)

DEDICATION

I dedicated this thesis to

To our God, most gracious and most merciful

To Prophet Mohammed and his family, May god pray him and his family

My Imam Al -Mahdi (Allah hastens his reappearance)

My dear beloved father, Ask God to bestow him in His vast mercy and My kind mother, My husband, brothers, sisters and sons.

To all whom I love and respect.

Nesreen

2021

Acknowledgements

*After thanking "**Allah**", I would like to express my gratitude and appreciation to my supervisors Dr. **Jassim Mohammed Salman** and late Dr. **Ali Sabea Hmmood** (may God have mercy on him) for their valuable efforts, guidance, support and encouragement throughout this thesis.*

Many people have guided me throughout this study and I would like to thank them here. I would like to express my gratitude to them.

My thanks go to the staff of Materials Engineering Department at the Faculty of Engineering - University of Kufa for their inestimable help

*Special thanks go to Assist Lec. **Mahmood shakir Naser, Furqan Wahhab Abdulsada** and **Maytham Saad Ali** for help me accomplish this work.*

Also I'd like to thank all those who contributed, even with something little to show this research as required.

Nesreen

2021

Supervisors Certification

We certify that this thesis entitled " **Surface Modification of 2101 Lean Duplex Stainless Steel for Biomedical Applications** " had been carried out under our supervision at the at the University of Babylon / Faculty of Materials Engineering / Department of Metallurgical Engineering in partial fulfillment of the requirements for the degree of Doctor of Philosophy in Materials Engineering / Metallurgical Engineering.

Supervisor

Signature:

Prof. Dr. Jassim mohammed Salman

Date: / / 2021

Supervisor

Signature:

Prof. Dr. Ali Sabea Hammood

Date: / / 2021

Examination Committee Certification

We certify that we had read this thesis entitled (**Surface Modification of 2101 Lean Duplex Stainless Steel for Biomedical Applications**) and as an Examination Committee examined the student (**Nesreen Dakhel Fahad**) in its contents and that in our opinion it meets the standard of a thesis and is adequate for the award of the Degree of Doctor of Philosophy in Materials Engineering/ Metallurgical Engineering.

Signature:
Prof. Dr. Ahmed O.Al-Roubaiy
University of Babylon
Date: / / 2021
(Chairman)

Signature
Prof. Dr. Nawal Mohammed Dawood
University of Babylon
Date: / /2021
(Member)

Signature
Ass.Prof.Dr. Mohammed Abdulrazzaq
University of Al-Qadisiyah
Date: / /2021
(Member)

Signature
Ass.Prof. Dr. Abdulsameea J.Al-Kilabi
University of Babylon
Date: / /2021
(Member)

Signature
Ass.Prof.Dr. Fatimah Jaffar Al-hasani
University of Technology
Date: / /2021
(Member)

Signature
Prof. Dr. Jasim Mohammed Salman
University of Babylon
Date: / / 2021
(Supervisor)

Signature
Prof. Dr. Ali Sabea Hammood
University of
Date: / /2021
(supervisor)

Approval of Metallurgical
Engineering Department
Head of the Department

Signature

Prof. Dr. Saad Hameed Al-Shafaie

Date : / /2021

Approval of Material´s
Engineering College
Dean of the College

Signature

Prof. Dr. Imad Ali Disher

Date : / /2021

List of Contents

List of Figures

List of Tables

List of Abbreviations

Abbreviations Symbol	***Definition***
AFM	Atomic Force Microscopy
AISI	American Iron and Steel Institute
ASTM	American Society for Testing and Materials
BCC	Body Center Cubic
CPT	Critical Pitting Temperature
CrN	Chromium nitride
DSS	Duplex Stainless Steel
DGON	Dragon Coatings
EDS	Energy Dispersive Spectroscopy
E_{pit}	pit nucleation potential
FCC	Face Center Cubic
HV	Vickers hardness
HVOF	High Velocity Oxygen Fuel coating
i_{pitt}	pitting current
i_{corr}	corrosion current
I_{pp}	protection current
LDX	Lean Duplex Stainless Steel
OCP	Open circuit polarization
OM	Optical Microscope
PM	Powder Metallurgy
PREN	pitting resistance equivalent number
R_E	re-passivation potential
SBF	Simulated body fluid
SCC	Stress Cracking Corrosion
SEM	Scanning Electron Microscopy
Ta_2O_5	Tantalum Oxide
TaN	Tantalum Nitride
TTT	Time Temperature Transformation diagram
WE	working electrode

Symbol	***Definition***
α	Ferrite phase
γ	Austenite phase
σ	Sigma phase
χ	Chi phase
γ_N	expanded austenite
Ta_2O_5	Tantalum oxide
TaN	Tantalum nitride

Abstract

Lean duplex stainless steel 2101 is an alloy of stainless steel with a chromium of (21%) and nickel of (1%) content that has strong mechanical properties, good corrosion resistance, and various industrial applications. The low nickel content of this alloy gives a positive medical advantage (less than 316L stainless steel) because the amount of toxic nickel ions emitted inside the human body would be low, in addition to its relatively low cost (it is considered one of the cheapest types of stainless steel due to the few alloying elements present in the alloy).

The weakness of the bone Osseo-integration in the bone tissue and the consequent risks of surface contact between the metal implant and human body fluids lead to severe corrosion. In order to bypass these limitations, in this thesis, various surface modifications were performed on the LDX 2101 DSS alloy, and then the effect of the type of surface modification and its parameters were studied on improving the mechanical properties, surface properties, anti-bacterial activity, adhesion strength, and corrosion resistance of the surface layer formed as a result of these surface modifications and determining the optimal values for those parameters.

Three surface modification treatments for duplex stainless steel alloy (LDX 2101 DSS) were used with different conditions for each treatment: plasma nitriding technique at a voltage of (400) v and a current of (30) mA with times of (5,10,15,20,25) hrs; deposition of tantalum oxide using a plasma sputtering technique at a voltage of (3500) v and a current of (10) mA with times of (2,4,6,8,10) hrs, and deposition of tantalum nitride using a plasma sputtering technique at a voltage of (3500) v and a current of (10) mA with times of (2,4,6,8,10) hrs.

The mechanical properties of the formed surface layer were studied using the Vickers micro-hardness test, while the surface characteristics

were studied by scanning electron microscope (SEM and FESEM) and atomic force microscopy (AFM), in addition to examining the chemical composition of the distribution of the elements on the surface of the formed layer using energy dispersive spectroscopy (EDS). As for the phases formed as a result of surface treatments on the formed layer, they were analyzed by X-ray diffraction (XRD).

After that, the formed layer was tested for its resistance to harmful bacteria, E.Coli, as well as its resistance to adhesion. Finally, the behavior of surface modified samples in the fluid simulating the human body (Ringer solution) was studied using open circuit potential and electrochemical dynamic and cyclic polarization tests.

The results showed an improvement of (65%, 52%, and 85%) in the hardness values for nitrided samples and sputtered samples with Tantalum Oxide and Tantalum Nitride, respectively. The scanning electron microscope (SEM) images showed the formation of a surface layer with a dense, coherent structure free of cracks or defects. The results of (XRD) and (FE-SEM) revealed the formation of new phases in the surface layer (expanded austenite S, Ta_2O_5, TaN), which indicates that the surface modification conditions were very good, while the results of (AFM) displayed an increase in the surface roughness values of the surface modified samples with the increase in the treatment time.

The results of the antibacterial activity test with E.Coli strains showed that the formed layer from surface modifications has a strong antibacterial effect to prevent bacterial growth. As for the results of the adhesion resistance test, it was shown that the modified layer for all types of surface treatments used had an acceptable adhesion strength.

The results of the polarization curves showed an increase in the corrosion resistance of the surface modified samples compared to the untreated

samples. The results revealed that the best condition for plasma nitriding was at time (10) hrs, where the nitrided layer has the lowest corrosion rate (0.057 mpy) in Ringer's solution, while the best condition for deposition of tantalum oxide using plasma sputtering technique was at time (8) hrs, where the deposited layer has the lowest corrosion rate (0.0492 mpy). On the other hand, the best time (8 hrs) for deposition of tantalum nitride using plasma sputtering technique was when the precipitated layer had the lowest corrosion rate (0.022 mpy).

Finally, the gray relational analysis (GRA) method was used to determine the optimum conditions for surface parameters (type of surface modification, voltage, current, time) and responses (corrosion rate, surface layer thickness, Vickers hardness, surface roughness). To accomplish this study, the program (Minitab17 Microsoft) was used. Experiment 14, which has a surface treatment of tantalum nitride deposition with a plasma sputtering technique, was recorded with the optimal response factors being time (8 hrs), voltage (3500) volts, and current (10 mA).

The treatments and surface modifications that were used to develop LDX 2101 DSS in mechanical and surface properties and corrosion resistance will meet the future requirements of applying the alloy as a strong and alternative competitor for orthopedic biomedical applications.

Chapter One

Introduction

1.1 Introduction

Like other materials, biomaterials can be classified into four main categories polymers, ceramics, composites, and metals. Pure metals and alloys are among the metallic alloys. Stainless steels, pure titanium and its alloys, Cobalt base alloys, also a few another metals are the most widely used metals and alloys for medical device applications [1,2].

Metallic biomaterials are typically applied for applications as load bearing, and therefore should be of high strength, hardness, fracture toughness and fatigue strength. When used in services, the most critical property of a metals as a biomaterial is it doesn't have a negative effect., i.e., it is biocompatible. Good mechanical properties "hardness, tensile strength, Young's modulus, and elongation" are also necessary, as well as Osseo incorporation, high corrosion resistance, and excellent wear resistance [3].

The formation of an invisible and adherent chromium rich oxide surface coating gives stainless characteristics. This passive film serves as a barrier to corrosion processes in alloy systems that would otherwise experience very high corrosion rates [4].

First stainless steel used for implants includes 18wt% Cr and 8wt% Ni making it stronger and more corrosion resistant than steel. The corrosion resistance of stainless steel type 316 has been increased by the addition of molybdenum (Mo). Then, the carbon (C) content was lowered from 0.08 to 0.03 wt% resulting in 316L which increased corrosion resistance to chloride solution [5].

Figure 1.1 shows the noticeable progress in the development of biomaterials and implants for a variety of applications in the body

Figure 1.1 (a) An implant for total shoulder replacement. (b) An implant for total hip replacement (c) An implant for total knee replacement (d) The development of root form designs of titanium implants and (e) a photograph of several designs used in clinical practice [4,5].

In the "Schaeffler Delong" scheme, the effects of the alloyed elements on the structure of steel are summarized (Figure 1.2). The diagram is based on the fact that the alloying elements can be classified into ferrite stabilizers and austenite-stabilizers, it becomes possible to calculate the total ferrite and austenite stabilizing effect of the alloying elements in the steel. This gives the so-called chromium and nickel equivalents in the Schaeffler-

Delong diagram. The Schaeffler-Delong diagram is not the only diagram for assessment of ferrite contents and structure of stainless steels [6].

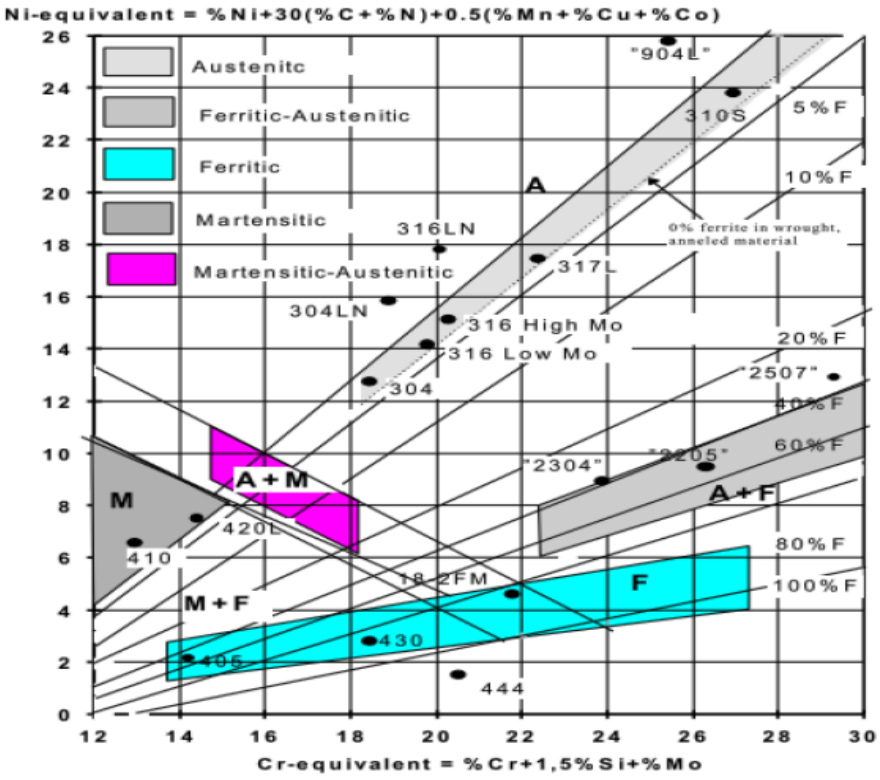

Figure 1.2 The Schaeffler-Delong diagram [6].

For implantations the most often used stainless steels were austenitic stainless steels 316 and 316L which were alloyed with molybdenum and have a stronger resistance to crevice and pitting corrosion in chloride environments than 304 steels. The function of the nickel is to stabilize the austenitic structure of the steel at room temperature and below. The minimum nickel content that required to stabilize the austenitic is approximately 8%. Nickel can also reduce the rate of general corrosion since it is a more noble metal than chromium or iron [7].

1.2 Duplex Stainless Steels

Duplex stainless steel groups have a biphasic microstructure (Figure 1.3), typically "austenitic" and "ferritic" and include about equal fractions of these phases and combining many of the benefits of single phase alloys

while avoiding some of the disadvantages. The adding of N to modern duplex stainless steels improves their good toughness, good stress corrosion properties, high strength and a lower alloy cost [8-11].

Figure 1.3 Microstructure of duplex stainless steel [12].

In the two-phase region in phase diagram, high Cr content (17.30%) and relatively low Ni contents (1.7%) produce about equal amounts of austenite and ferrite after heat treatment. Mo and N are most common alloying elements that are utilized to improve strength, resistance of corrosion, and microstructure balance. Duplex stainless steels often combine the characteristics of both austenitic and ferritic steels [13].

When the temperature of a common duplex stainless steel alloy drops below the melting point, a two-phase field known as the partially melted zone forms, which is a mixture of liquid and solid ferrite phase. This is due to the high temperature, which promotes ferrite formation. As the ferrite matrix cools more, austenite regions appear (Figure 1.4). Because austenite is formed from ferrite, it is thermodynamically impossible for the alloy to go above the austenite equilibrium level. With duplex, the highest problem forms brittle intermetallic phases like Chi, Sigma, Alpha Prime and R extremely quickly [12].

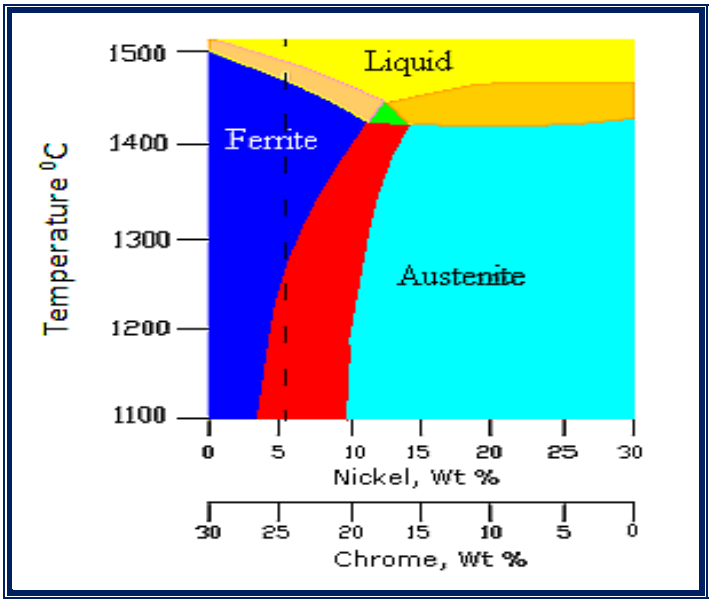

Figure 1.4 Fe-Cr-Ni Phase Diagram [12].

TTT diagram (Figure 1.5) shows precipitation phenomena in duplex stainless steels and the influence of the different alloying elements. From all these precipitates, the most damaging is the sigma (σ) and Chi (χ) phases. The sigma phase is a chromium-rich inter-metallic phase. Its precipitation depletes the surrounding material from chromium, and rends the alloy less corrosion resistant. The Chi phase is similar to the sigma phase but contains more molybdenum [14].

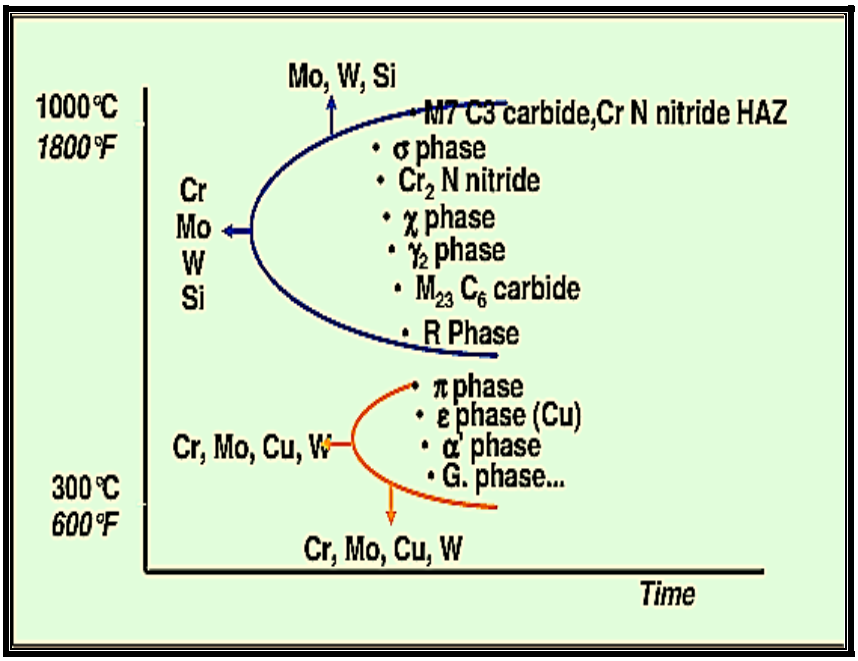

Figure 1.5 TTT diagram of secondary precipitates in duplex [14].

Duplex austenitic ferritic steels combine some of the features of each phase: they are higher tensile, high weldability; their toughness are greater of the ferritic steels but lower to that of the austenitic steels, and their strength is superior than the austenitic steels by a factor of about two and resistant to stress corrosion cracking due to the existence of the austenitic phase, it's have good resistance of corrosion [8,10].

1.2.1 Evolution History of Duplex Stainless Steels

This section is summarized and classified into two parts: duplex stainless steel and lean duplex stainless steel [15-19]:

DSS has been available for a long time, but recently starts to increase sharply. From the **1960**s **to 1970**s a nickel shortage drove up the price of austenitic stainless steels, so stimulating the use of duplex grades. Other developments favored their wider use: the introduction of the vacuum and argon oxygen decarburization (VOD and AOD) made it possible to reduce carbon levels and control nitrogen content. In the **1980**s a second generation of duplex grades came into being, in which nitrogen assumed a central role.

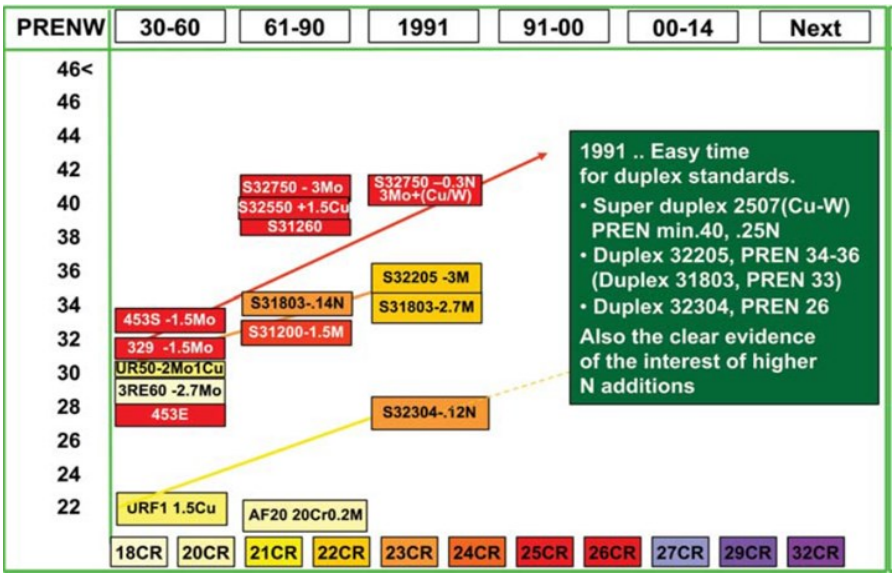

Figure 1.6 The evolution of duplex stainless steel chemistries between the 1930s and1990s [16].

It is not appropriate to replace austenitic grades with duplex grades as the benefits do not justify the extra cost. Thus there arose the need to develop lean (low-nickel, low-molybdenum) duplex grades. Austenitic replacement and the desire to avoid over specification of stronger duplex grades are two of the most important factors driving development today. The Super- and Hyper-duplex grades have a dual goal to improve corrosion resistance while lowering susceptibility to detrimental intermetallic phases.

The second advancement was the use of lean duplex stainless steel grades with no Mo or Ni in applications where austenitic stainless steel grades 304 or 316 could be used. Since approximately 2000, the addition of (Mn) has been considered to have created a new family of DSS. Ni additions are substituted with Mn additions and additional (N) additions in those grades. Optimization of alloying and further cost reduction pressures were driving forces for the development of leaner duplex grades. More recently Outokumpu has proposed the UNS S 82441 (LDX 2404) grade presenting higher mechanical properties through increased N additions by taking advantage of almost 3% Mn and 24% Cr additions. Lean duplex stainless steel (LDSS) was considered to be a modern grade.

1.2.2 Grades of Duplex Stainless Steel

Recent Duplex Stainless Steels have developed into groups [20,21]:

- ***Lean grades***

Lean grades have low Ni and often no Mo are presented in these grades, which have strong mechanical properties but poor resistance to chloride localized corrosion, lowest pitting resistance.

- ***Regular grades***

These grades have > 4% Nickel and >2.5% Molybdenum, good mechanical properties, and much greater localized corrosion resistance than lean

grades. 3RE60 (UNS S31500) and 2205 (UNS S32205/S31803) are classic regular grades.

- ***Super grades***

These grades have > 5% Ni and > 3% Mo, very high resistance to localized corrosion and higher strength than regular duplex grades.

- ***Specialized "hyper-duplex" grades***

These grades that resist chloride localized corrosion in all marine applications are existing in limited product forms. Its efforts are being made to develop new "Hyper duplex" grades, which existing, in some applications, corrosion resistant properties higher than 6% Mo. The hyper duplex grades have been mostly used in the manufacture of seamless tubes. They promise cost effective replacements to super austenitics, nickel based alloys for exchangers cooled by seawater.

1.2.3 Duplex Steels Structure

A two phase structure of DSS is divided into four structure types (as shown in Figure 1.7) as follows [22]:

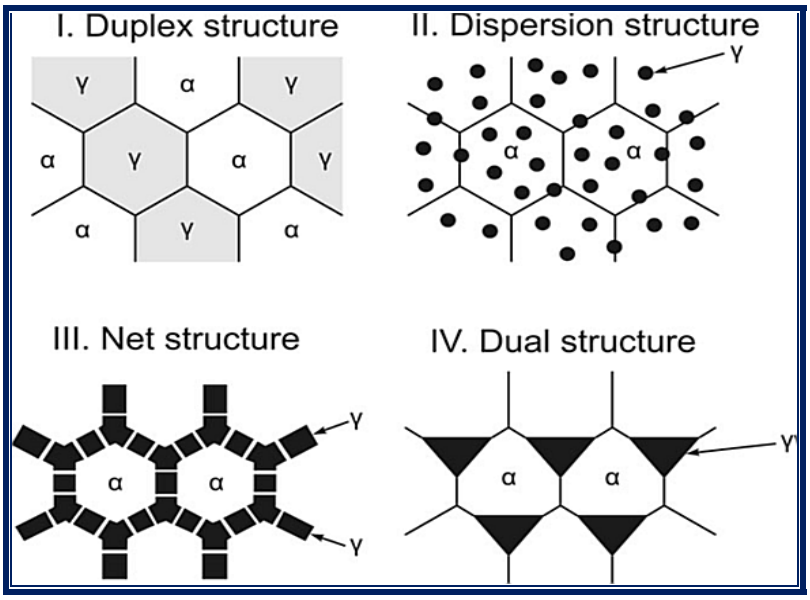

Figure 1.7 Four types of two-phase structures [22].

The structure of crystal comprises of α (BCC) and γ (FCC). The following parameters may be used for determining the characteristics of two phase materials:

• Duplex-structures: Two structure components γ and α lie as crystals of the similar size statistically distributed next to each other.

• Dispersion structure: All parts of the "γ" phase lie isolated in the basic "α" matrix.

• Net structure: The second phase "γ" precipitates only on the grain boundaries of the basic "α" matrix.

• Dual phase structure: The volume of the γ and α grains is equal, and their distribution is uniform and independent of the volume ratio, similar to duplex structures. The "γ" phase must be separated from the "α" phase [22].

Compared to single phased austenitic and ferritic alloys, the advantages and disadvantages of DSS, may be stated as follows:

- Thermal conductivity is superior than austenitic grades.
- Strength is higher than austenitic grades.
- Precipitation and transformation are complex behavior
- Due to formation of nitrides, carbides, and intermetallic phases, it's have high tendency to embrittlement
- Impact value is higher than ferritic grades.
- Resistance of hydrogen embrittlement higher than ferrites
- Increased resistance of pitting, intergranular, stress-corrosion cracking and crevice corrosion.
- Increased resistance of general corrosion.

1.3 Lean Duplex Stainless Steel

Duplex stainless steel use has been rising gradually worldwide, and the variations in nickel prices in recent years have caused further growth.

Outokumpu lean duplex grade "LDX 2101" (EN 1.4162), "UNS S32101" is a low Ni amount that is alloyed with N and Mn to get a balanced microstructure. LDX 2101 (EN 1.4162), "UNS S32101", and 2304 (EN 1.4362), "UNS S32304", successfully replaced austenitic steel of type 304 (EN 1.4301) and AISI 316L (EN 1.4404). The transformation to austenite happens in the solid phase and is governed by N diffusion. DSS is often solidified in a ferritic mode. Austenite precipitates first at grain boundaries. Examples of lean grades are 2002 (UNS S32002), 2101 (UNS S32101) and 2304 (UNS S32304). The first two numbers are Cr content and Ni content are the last two [13,23,24].

Duplex stainless steels can suffer large microstructural modification at room temperature as a consequence of either thermo-mechanical treatment, nitride precipitation, ferrite decomposition, which causes "S" and "X" phase formation or plastic deformation, austenite transformation into stress induced martensite "SIM". These minor phases abnormally affect the properties of "2101" LDX, so are of huge industrial interest [25].

The total consumption of stainless steel still duplex stainless steel accounts for only a small portion. One of the most recent developments is the penetration by duplex grades (especially lean grades). In both, the mixture of lightness and strength is an important advantage [26].

Nowadays the chief aim is the improvement of lean duplex stainless steels, which have far less alloying elements than the standard "2205" duplex grade. LDX has been substituting "304" and even "316" groups. "2202" and "2304" LDX grades were produced by Industeel, which offer excellent cost effective alternatives to "304L" and "316L" in a variety of applications. The chemistries of some of these alloys are existing in Table 1.1 [25,27].

Table 1.1 New lean duplex grades compared to 304L and 316L [27].

USA	EN	Cr	Ni	Mo	N	Cu	Mn	PREN
304L	1.4307	18	9	-	-	-	1	18
316L	1.4401	17	10-14	2.5	-	-	1	24
S32001		20	1.7	0.3	0.15	0.3	5	23
S32101	1.4162	21.5	1.5	0.3	0.2	0.3	5	26
S32202	1.4062	22.7	2	0.3	0.21	0.2	1.3	26/27
S32003		20	3.5	1.7	0.15	-	2	28

1.4 Applications of Lean Duplex

Duplex stainless steels are essential for many applications such as [23,28,29]:

- Heat exchangers, Pressure vessels, piping systems and tankers, tanks
- Air Pollution Control
- Beverage and Food Process Equipment
- Biofuels, Biodiesel, tanks and Ethanol plants
- Bridges, Infrastructure, sluice gates, flood gates
- Seawater Treatment, Wastewater and Water.

Figure 1.8 Lean duplex allows Vossloh to reduce weight and maintenance on its Tramlink and Lean duplex rebar was used on the Gateway Upgrade Project in Brisbane, Queensland, Australia [26].

1.5 Scope and Objectives

The overall objective of this PhD thesis is to study the response to plasma technique to deposit suitable layers of nanocomposite coatings of (nitride, Ta_2O_5 and TaN) on a new medical grade duplex stainless steels 2101 in order to enhance their surface properties for orthopedic biomedical applications and investigates of the most essential variables to obtain the best properties of coating in order to improve the performance of the biomedical implant. Exactly, the main objectives of the present study are:

1- Characterization and evaluation of the coating layer by studying the parameters of the surface modification process that effect on the coating such as deposition time.

2- Attaining surface layers with good homogeneity and morphology to produce bioactive coatings.

3- Getting multi-properties surface layers gathering high mechanical properties and biocompatibility.

4- To study the microstructure, surface morphology, phase identification, antibacterial activity, adhesion strength as well as the corrosion behavior of modified and unmodified 2101 Lean Duplex Stainless Steel after immersing in Ringer's solution by linear potentiodynamic and cyclic polarizations.

Chapter Two

Theoretical and Literature Review

2.1 Introduction

The requirements for the biomaterials are very severe due to the human body; they are exposed to the aggressive effects of body fluids and external factors. A number of mechanical properties such as tensile strength, hardness, elasticity, suitable density, wear resistance, etc. are also essential. According to implant interaction with the host tissue they can be categorized into bioinert, bioactive and bioresorbable materials. The bioactive materials evoke a specific biological response and make connections with the host tissue [30].

The common reasons for implant failure are stress shielding and stress concentrations, corrosion and toxicity risk, Infection and Implant loosening and Osseo integration. Nickel is known to be carcinogenic and has been observed to cause allergic, cytotoxic, and mutagenic responses. Ion release can also cause formation of a membrane around the implant, which prevents or disrupts the integration of the implant with surrounding bone tissue, a process that may lead to failure of the implant. Solid implants have less contact surface than porous implants. The amount of nickel released from porous implants has been observed to be higher than in solid, nonporous material, perhaps due to the higher surface area. For implants additional surface modifications and coatings are possible solutions [31].

2.2 Important Considerations on Biocompatible Metals

To produce safe implants with a long lifetime and without inducing rejection, the biomaterials should possess desirable characteristics including [32-36]:

1. *Biocompatibility*

Biocompatibility is defined as the ability or capacity of the material to be used in close connection with living tissue without causing adverse effects to them. The materials used as implants are expected to be highly non-toxic and should not cause any inflammatory or allergic reactions in the human body. The body parts coming into contact with the implants should avoid any physical irritation, inflammation, and toxicity, mutagenic or carcinogenic action. The greater the corrosion of the implants, the more toxic ion rates are released into the body. Surface topography is also very essential for the biocompatibility of implant material [37].

The biocompatibility requirements are strict and complex; altering the particular medical applications resulting in the release of the toxic metallic ions. Thus, the biocompatibility of a medical appliance envelops equally in the compatibility and design of materials utilized, including the device mechanics, electrical control, and geometry. Concerning the biocompatibility of implant materials, these include the physical impacts on the tissues surrounding the implanted material or the mechanical properties of the materials. Bioactive materials are widely chosen since they promote high integration with adjoining bone. Ideally, to develop a biomedical alloy, the non-toxic elements must be chosen as the alloying elements [38].

2. *Mechanical Compatibility*

It refers to the appropriate mechanical properties according to the function to be performed and the site to be implanted. In addition, bio-implants shall have appropriate mechanical strength to withstand all forces and related loads. Primarily, the material selected for bio application must have the ability to withstand the load; therefore, they will not be susceptible to fracture. Tensile strength, hardness, Osseo integration, modulus of elasticity, resistance to corrosion wear is some of the properties that are of

fundamental importance. Biomechanical incompatibility that leads to the death of bone cells is called the stress shielding effect. Therefore, a material with excellent combination of high strength and low Young's modulus closer to the bone should be used for implantation.

3. *High corrosion resistance*

The presence of body fluids allows metal implants to release metallic ions that may accumulate in nearby tissues or be transported to other parts of the body. Corrosion is one of the major processes that affect the life and service of orthopedic appliances made of metals and alloys used as implants in the body. Corroded implants in the human body cause excess of harmful and toxic metal ions such as Fe, Cr, Ni, Co, and Ti released into the body fluid. When the oxide layer on the metal is broken, corrosion occurs and a metal ion is released.

The atmosphere within the human body is dissimilar to ambient conditions, both chemically and physically. Therefore, a metal that presents well and is passive or inert in the air can undergo brutal corrosion in the body. In fact, stainless steel is the most corrosion resistant metal but normally causes toxic reactions and chronic allergy in the host body.

4. *High wear resistance*

The low wear resistance leads to the release of wear debris from the implant into the surrounding tissue which can produce an adverse cellular response leading to the release of harmful enzymes, inflammation, osteolysis, infection, and pain and bone resorption. The wear resistance of the material plays a significant role in the biomaterial proper functioning, avoiding loosening of the implant and reactions in the tissue in which it is deposited. Then in the incongruent joints, for example, the ankle and knee joints, the relationship between the hard surfaces of these two

incongruences make very heterogeneous or strong stresses (Figure 2.1). The friction between the implant and other tissues may increase the release of ions. Thus, the development of implants with high resistance to corrosion and wear is of prime importance [39,47].

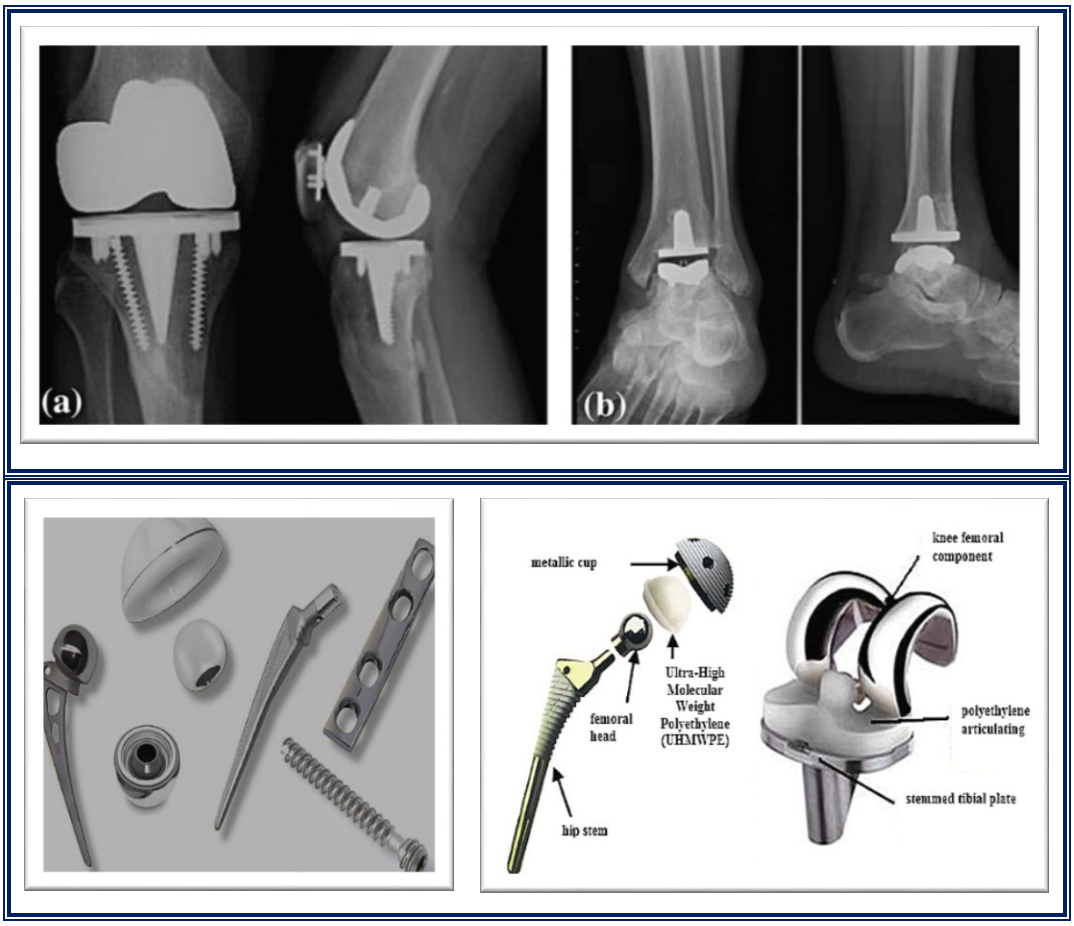

Figure 2.1 Schematic diagram of the SS implant in (a) knee, (b) ankle, (c) examples of different orthopedic devices, (d) artificial hip joint and knee implant [39].

5. *Osseo-integration*

Osseo-integration is the practice of bone healing and new bone development, which is a fundamental condition in orthopedics. The creation of fibrous tissue around the implant makes an implant surface incapable of bonding to other tissues and adjacent bone because of micro motions that promote the prosthesis loosening. Hence, a suitable surface is necessary for an implant to mix well with adjacent bone. The surface roughness, topography, and chemistry are the measured aspects for a good

Osseo-integration. Osseo integration refers to a phenomenon where an implant becomes so fused to the bone that it cannot be separated without a fracture, and when an implant is Osseo-integrated there is no progressive relative movement between it and the bone, with which it has direct contact. Among other factors, roughness and wettability are very important in Osseo-integration. It is defined as the direct anchoring of an implant by the formation of bone tissue around the implant without fibrous tissue growth at the bone implant interface [40].

2.3 Surface Modifications for Biomedical Materials

Surface engineering technology is a suitable method for coatings on the metal surfaces or performing surface modification treatment, this can improve corrosion resistance and biocompatibility of metals [41].

Surface modification is a process that changes a material's surface composition, structure and morphology, leaving the bulk mechanical properties intact. With surface modification, the tissue compatibility of the surface layer can be improved [42].

Surface modifications of biomaterials have led to improvements in device multi-functionality, tribological and mechanical properties, and the biocompatibility of artificial devices, while avoiding the need for additional costs and time. It changes the physiochemical properties of the materials such as surface charge, surface energy and surface composition [43].

The biological characteristics of implants can be enhanced by adding materials with desired properties, changing the composition, or removing unwanted materials from the implant surface. These methods are known as surface treatments and can be classified into four categories: mechanical, physical, chemical, and biochemical surface modifications. Machining, grinding, polishing, and blasting are mechanical surface modifications.

Physical surface treatments include thermal spraying, physical vapor deposition, ion implantation and deposition, and glow discharge plasma treatment. Chemical surface modifications include chemical treatment (acid, hydrogen peroxide, alkaline, etc), anodic oxidation, sole gel processes, and chemical vapor deposition [44]. The bio functionality of metallic biomaterials is generally poor because the biomaterials do not directly fuse with living tissue [45].

Physical modification of the oxide surface increases cell adhesion. Surface modification is generally accepted as a route to enhance cell functions for biomaterials and tissue engineering applications. Consideration must be given to modifying cell morphology to enhance cell behavior, density or orientation of the modifier and stability of the modifier on the surface. Surface modifications are needed [46,47]:

- To improve the functional lifetime of an implant by decreasing the rate of degradation due to corrosion and wear.
- To promote and improve fixation by improving the strength of adhesion to host bone and to accelerate the rate of bonding.
- To promote Osseo integration by influencing the attachment and differentiation of osteoblasts.
- In the case of restorable graft materials, to permit the attachment of osteoclasts, formation of resorption lacunae and eventual remodeling.
- To deliver cells, biomolecules or drugs to the implant site to promote healing and prevent infection

The type of growth surface has a crucial effect on the cells' binding to the substrate. With the surface modification, it is possible to control the behavior of the cells, to increase the adhesion of one type of cell and limit the growth of the other types of cells. The applied surface modification

would simplify the binding of the cells to the surface and generally enable their good spreading [48].

The biological response from living tissues to the biomaterials is reliant on the surface properties such as chemical composition, cleanliness, topography, surface energy, corrosion resistance, and the tendency to denaturalize neighboring proteins. The surface properties are the major factors that determine rejection or acceptance of a biomaterial in the body because the surface is the interface where the biomaterials meet and interact with the biological environment. It is rare that a biomaterial with bulk properties possesses appropriate surface characteristics for medical applications, and very few surfaces are biocompatible, therefore a biocompatible modified layer with suitable wear and corrosion resistance would ease the above problems [49].

The surface properties are surface chemistry, surface wettability, surface texture and surface charges. The surface chemistry of most of the commonly used metallic biomaterials is primarily determined by the chemical composition of a surface oxide layer. Surface texture is available on metals in macroscale, microscale, and nanoscale. The surface charges of metals can be positive, negative, or neutral. The surface modification typically contains either altering the original surface or depositing a coating on the existing surface. In both the cases, all the surface properties including surface chemistry will then depend on the nature of modified surfaces [50].

2.4 Surface Modification Techniques

Surface engineering is processing of the surface characteristics of the object obtained through removing or adding the material. The surface engineering processes are majorly classified into two categories: surface

modification (treatment, cladding, and machining) and surface finishing (polishing and grinding). To enhance the service life of biomaterials, by the special treatment or technique used on the surface to increase the productivity of biomaterial in the harsh human body environment. Table 2.1 presents the various surface modification techniques and their own advantages and drawbacks. Bioactive materials are active to form chemical bond with human bones. Bioactive materials are blend of oxides (SiO_2, CaO, MgO, Ta_2O_5, etc.) which stimulates the composition of bones and proved excellent treatment results [51].

Table 2.1 Surface modification techniques for metallic alloy as a biomedical implant [44,52].

Surface modification methods	**Modified layer**	**Objective**
Mechanical methods • Machining • Grinding • Polishing • Blasting	The rough or smooth surface formed by the subtraction process	Produce specific surface topographies; Clean and roughen surface; improve adhesion in bonding
Chemical methods • Acidic treatment • Alkaline treatment	<10 nm of the surface oxide layer ~1 μm of sodium titanate gel ~5 nm of dense inner oxide and porous outer layer	Remove oxide scales and contamination Improve biocompatibility, bioactivity, or bone conductivity
Sol-gel	~10 μm of the thin films, such as CaP, TiO_2, and silica	Improve biocompatibility, bioactivity, or bone conductivity
Anodic oxidation	~10 nm to 40 μm of TiO_2 layer,dsorption, and incorporation of electrolyte anions	Produce specific surface topographies; improve corrosion resistance and biocompatibility

Chemical vapor deposition	~1 μm of TiN, TiC, TiCN, diamond, and diamond-like carbon thin film	Improve wear resistance, corrosion resistance, and blood compatibility
Glow discharge plasma	~1 nm to ~100 nm of surface modified layer	Clean, sterilize, nitride surface; remove the native oxide layer
Biochemical methods	Modification through silanized titania, self-assembledmono layers, photochemistry, protein resistance, etc.	Induce specific cell and tissue response by means of surface immobilized peptides, proteins, or growth factors
Physical methods • Thermal spray • Flame spray • HVOF • DGON	~30 to 200 μm of coatings, such as titanium, HA, calcium silicate, Al_2O_3, ZrO_2, TiO_2	Improve wear resistance, corrosion resistance, and biological properties
PVD • Evaporation • Ion plating • Sputtering	~1 μm of TiN, TiC, TiCN, diamond, and diamond-like carbon thin film	Improve wear resistance, corrosion resistance, and blood compatibility
Ion implantation and deposition Beam-line ion implantation and P-III	~10 nm of the surface modified layer and/or ~μm of thin film	Modify surface composition; improve wear, corrosion resistance, and biocompatibility

Since surface modification for medical implants is primarily used to improve or optimize the properties of a biomaterial, the various modification techniques should generally be simple, robust, and cost effective. Surface modification techniques can generally be classified into two groups, subtractive modifications and additive modifications. Subtractive surface modifications refer to a change in the surface as a result of removal of the surface layer (physical modifications). It includes

abrasive blasting and plasma treatments. In contrast, additive surface modifications refer to a change in the surface as a result of depositing films or biological factors on the biomaterial surface (coating or chemical modifications). Surface properties altered could include chemistry, grain size, crystallographic orientation, defects, stress concentration, film adhesion, surface topography, and biology–biomaterials interactions [53].

Plasma coating is a state of matter that is partially or fully ionized, and contains charged particles of free ions, electrons, radicals, as well as neutral particles of atoms and molecules. Plasma could be divided into thermal (high-temperature/hot/equilibrium) one and non-thermal (low-temperature/cold/non equilibrium) one. The thermal plasma is nearly fully ionized, and electrons and heavy particles have the same temperature. For non-thermal plasma, only a small fraction of the gas molecules is ionized, and ions and neutrals are at a much lower temperature (room temperature). The plasma used for the surface modification of biomaterials is the non-thermal one [54]. Some commonly used surface modification techniques and their effects (Figure 2.2).

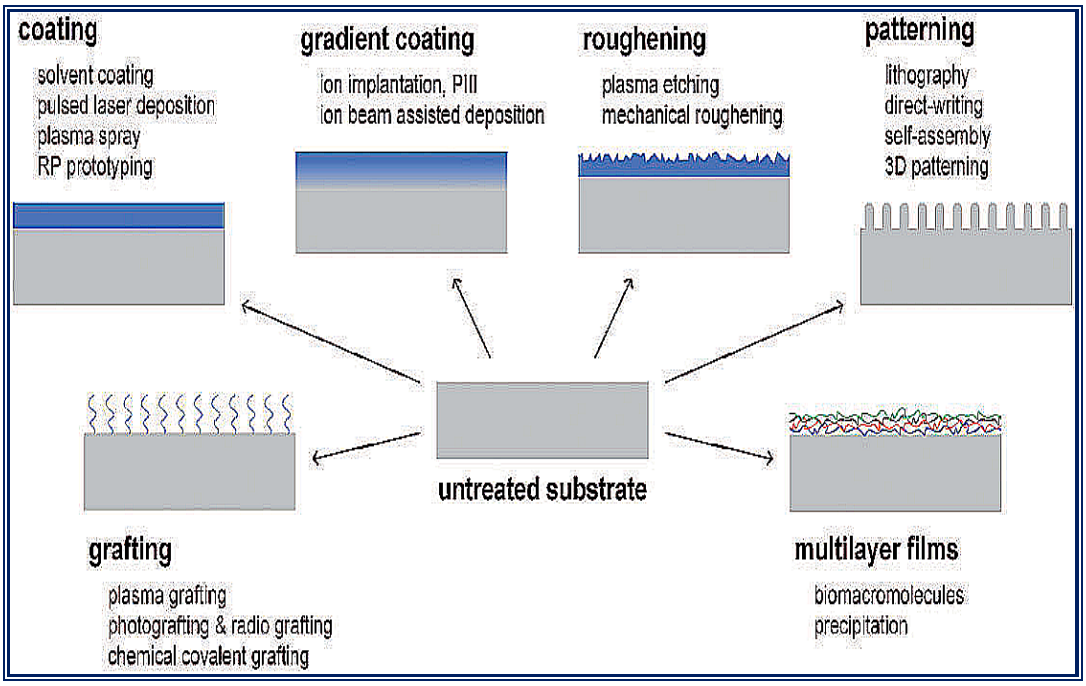

Figure 2.2 Schematic diagrams of surface modification techniques [54].

Physical modification techniques are divided into two distinct categories; the first involves chemical alteration of surface structures, while the second involves deposition of an additional external layer to the surface of the substrate. Chemical modification of metallic biomaterials mainly depends on the chemical reactions occurring at the interface between biomaterials and reactive solutions. The common methods are hydrogen peroxide, acid, alkali, and thermal oxidation treatments [55].

2.4.1 Sputtering Processes

Sputtering is a variant of PVD, which possesses similar line-of-sight requirements, but does not involve direct material vaporization. Instead, a flood of plasma-charged particles (ions) is generated. Ions are then driven toward the substrate from the target by electrostatic acceleration. It is always performed in vacuum. Sputtering may also sometimes make use of reactive precursors, thus named reactive sputtering. In contrast to evaporative PVD or CVD, coatings formed by sputtering are typically much denser owing to the much higher energy of deposition experienced by the ions during the coating process. However, owing to the lack of topography by sputtering alone, they tend to be coupled to methods. In some instances, optimization of the sputtering process (working distance and power) appears to be capable of generating *in situ* roughened super hydrophobic coatings [56].

The sputtering method also involves the use of ion beams, where the ions are accelerated toward a target, causing atoms to be ejected which are then deposited on the surface of a substrate. The treatment is used to form inorganic coatings, though the surface treated must be heat resistant to prevent deformation. This limits the application to heat-resistant metal implants. This treatment leads to good adhesion of the coating to the substrate and has been used to improve biocompatibility [57-59].

2.4.2 Plasma Processes

Plasma surface-modification techniques are depicted in Figure 2.3. Each of these techniques alters the surface properties of biomaterials to a different extent through surface cleaning, surface functionalization and deposition of materials. Metallic plasma is generated separately or simultaneously using vacuum arc plasma sources. More than one element can be introduced into the plasma system at any one time [60,61].

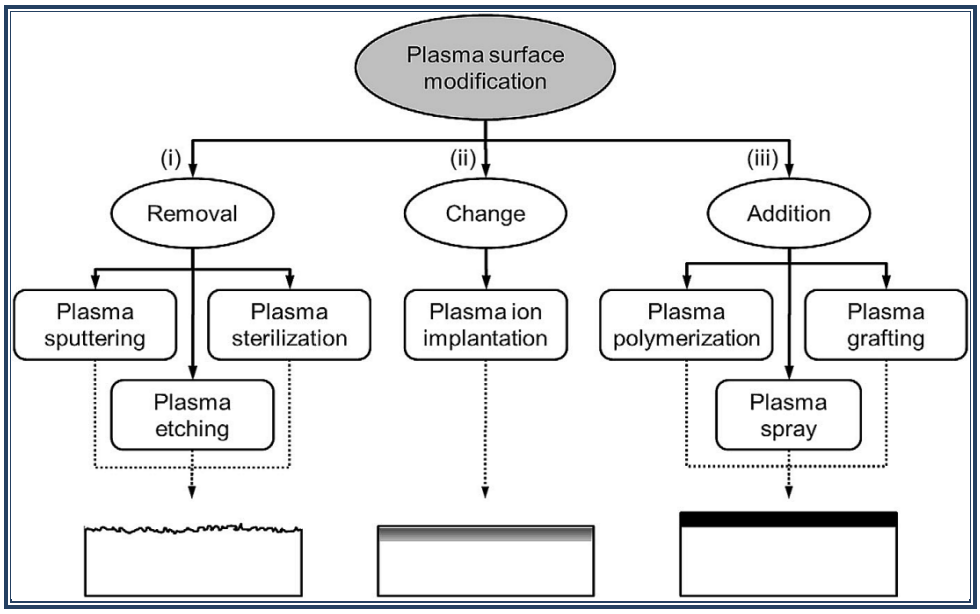

Figure 2.3 Classification of plasma surface-modification techniques [61].

2.4.3 Nitriding Processes

Nitriding are widely used technique for surface hardening of iron alloys and steels. Low temperature nitriding allow the formation of an expanded austenite. Expanded austenite is merely a metastable supersaturated solid solution of nitrogen in which the precipitation of nitrides is avoided if the processing temperature is lower than 450°C for nitriding. The nitrogen atoms dissolved in SS matrix are accommodated in the octahedral sites of the "FCC" stainless steel crystal structure. The concentrations are significantly higher than the maximum solid solubility and lead to a

substantial increase in the stainless steel lattice parameter crystallography of expanded austenite. The crystal structure of expanded austenite was defined as a compound layer having a M_4N (M=Fe, Cr, Ni) structure or as a combination of austenite and [$(Fe, Cr, Ni)_4M$] [62].

Nitriding is a heat treating process that diffuses nitrogen into the surface of a metal to create a case-hardened surface. It is effective way to strengthen the surface of materials and improve their surface hardness, tribological and corrosion properties. A number of different techniques are conventionally applied such as salt bath nitriding, nitriding and carburizing and plasma nitriding. However, increased treatment temperature can lead to the formation of chromium nitride precipitates in the nitrogen enriched layer, and thus worsen corrosion resistance. Therefore, gas composition, temperature and time have a main role in producing expanded austenite and formation of chromium nitride [63].

Nitriding is an act of bombarding nitrogen atom into lattice or interstices of a parent material to form solid solution. It involves ionized nitrogen gas from high-concentration region to low-concentration region. It requires high activation energy from temperature and pressure to overcome barrier since is a nonspontaneous reaction. Composition of other gas such as hydrogen, ammonia, or methane gas in nitriding of SS has better and improved mechanical properties than single gas nitriding. Hydrogen plays a role of removing oxide layer that might impair in-depth of nitrogen. Increase in N_2 composition increases the case depth, hardness, and the surface roughness of treated material [64].

The typical structure of a nitrided layer includes a gradient of nitride compounds followed by an interstitial diffusion layer and finally the bulk (Figure 2.4). The composition and proportion of the compounds present within the layer is highly dependent on both the process parameters and the

alloy composition (ε-$Fe_{3-2}N$, γ′-Fe_4N, CrN in SS). Higher temperatures and longer treatment duration lead to an increase in thickness of the compound layer. Gas nitriding relies on the use of ammonia or ammonia-hydrogen mixtures (eq.8), which first requires the removal of the surface oxide layer. Later, a thin Ni or Fe layer is plated to prevent re-passivation. Ni and Fe also act as catalysts for the decomposition ammonia during the heat treatment.

$NH_3 \rightarrow [N] + 3/2H_2$ …… (8)

After the diffusion of atomic N, the catalyst layer is removed by acid and passivation can be restored [65].

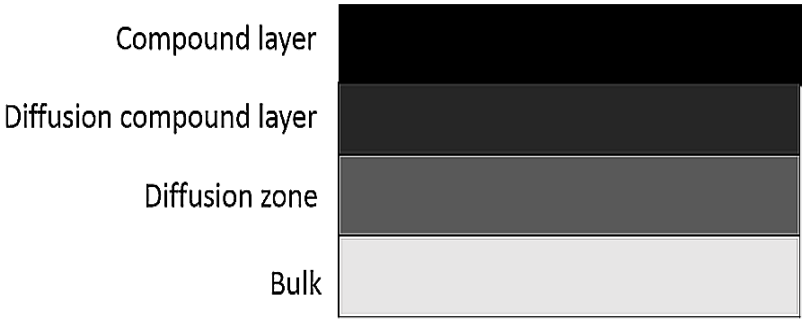

Figure 2.4 Schematic structure of a nitrided layer [65].

During the low temperature nitriding (below 500◦C), it is possible to obtain layers which are both wear and corrosion resistant. The layer which is formed on DSS is composed of the S phase only. The increase in nitriding temperature in the range of 400 –500◦C makes fine CrN precipitate from 'expanded martensite' reducing the corrosion resistance, but small size of nitrides allows high hardness. Layers nitrided above 500◦C are mostly composed of CrN and iron nitride, but still, S phase is present there [65].

Moreover, the increase of the nitrogen content leads to obtain of thick nitrided layers with higher hardness. The γN phase consists of a nitrogen supersaturated austenite, consequence of the possible presence of interstitial elements as N. γN phase have an Fcc structure where nitrogen

atoms are located in random octahedral sites, that generate compressive residual stresses and stacking faults production. In fact, although the addition of the nitrogen stabilizes the austenite, the presence of Cr element, especially at high concentration and temperatures higher than 450 ◦C, favors the precipitation of CrN [66].

2.4.3.1 Plasma Nitriding

Plasma nitriding is a thermochemical treatment associated with nitrogen incorporation into the bulk material. Notably, plasma-assisted nitriding at temperature below 500 ◦C improves not only the surface hardness, but also the corrosion resistance by producing the metastable FCC composed of supersaturated nitrogen atoms in the SS matrix. It is well known that nitrogen is a beneficial austenite-stabilizing element, which efficiently intensifies the resistance to localized corrosion [67].

The parts to be treated (the charge) form the cathode, and the furnace wall is the anode. The supplied gas is ionized in the electric field. On the surface area that is directly charged by the ions, nitrogen-rich nitrides are formed and decomposed, releasing active nitrogen onto the surface [68,69].

The process is popular because it requires less gas compared to gas nitriding and is more environmentally friendly. A different kind of process was developed, called active screen plasma nitriding (ASPN) to solve the limitations. The wear rate was increasing with an increase in the nitrogen content on the gas mixture. Moreover, both the thicker layer and the higher hardness are advantageous [70,71].

Expanded austenite formed during low temperature plasma nitriding is known for its excellent wear and corrosion resistance. Very fine and dispersed CrN nano sized precipitates are formed in the nitrogen rich region of the expanded austenite layer, after exposure to higher than 400 °C

where the N supersaturated austenite decomposes into a lower N austenite + CrN. When carried out at temperatures below 450°C, plasma and gas nitriding can increase the surface hardness, while avoiding chromium nitrides precipitation and chromium depletion in the matrix granting corrosion resistance. This behavior is due to formation of N enriched metastable phases expanded austenite also called S phase [72].

The nitrided layers situated in the austenitic phase (γ) were thinner than which in the ferritic phase (α) at low temperatures. The nitrogen atom has a higher diffusion rate in the ferritic phase during plasma nitriding treatment. The hardness increases with the increasing nitriding temperature, which is caused by the thicker nitrided layers and the higher nitrogen content in layers at high temperatures. The hardness increased by approximately 3 times compared with the matrix. Both α and γ phase of the matrix transformed into γ_N after plasma nitriding [73].

Expanded austenite phase is hard, wear resistant and a paramagnetic to ferromagnetic transition takes place for nitrogen content higher than 14 at. %. Another particular feature of the expanded austenite is nitrogen depth profiles in the nitrided layer, resulting in a hardness gradient which provides a good intermediate transition to enhance the adhesion of hard coatings on soft substrates [74].

Low temperature nitriding lead to nitrogen super saturation and formation of expanded austenite, expanded ferrite or expanded martensite. Such super saturation results in expansion of the crystal lattice and creation of very intense compressive residual stresses leading to an increase of the surface hardness due to the formation of these expanded phases. S phase uniformly formed on both austenitic and ferritic phases. The expanded ferrite layer is thicker than expanded austenite layer [75].

2.4.3.2 Mechanism of Plasma Nitriding

The most common plasma nitriding mechanism was nitrogen atoms diffusion takes place mainly as a result of the metastable M (Fe)N nitride decomposition, formed in the reaction of nitrogen atoms with sputtered from the surface Fe atoms in the cathode potential drop. On the other hand, hydrogen ions, nitrogen ions and argon ions are implanted in the subsurface layer depending on their energy values, and they create clusters that cause the nitrogen concentration growth effect and lead to an initiation of its inward diffusion processes. A further stage of the process is atomic nitrogen diffusion from the surface to the material core, which completely controls the thickness of the diffusion layer in plasma nitriding [76].

The mechanism for hardening by plasma nitriding is as follows: First of all, the interaction of atomic nitrogen with surface results in the formation of FeN. This nitride phase is unstable and is transformed to α and γ′ nitrides; therefore, the compound layer is formed. Moreover, with diffusing of nitrogen toward the core, the diffusion layer is formed (Figure 2.5). Plasma process allows both bulk and grain-boundary diffusion compared to only grain-boundary diffusion in gas nitriding [77].

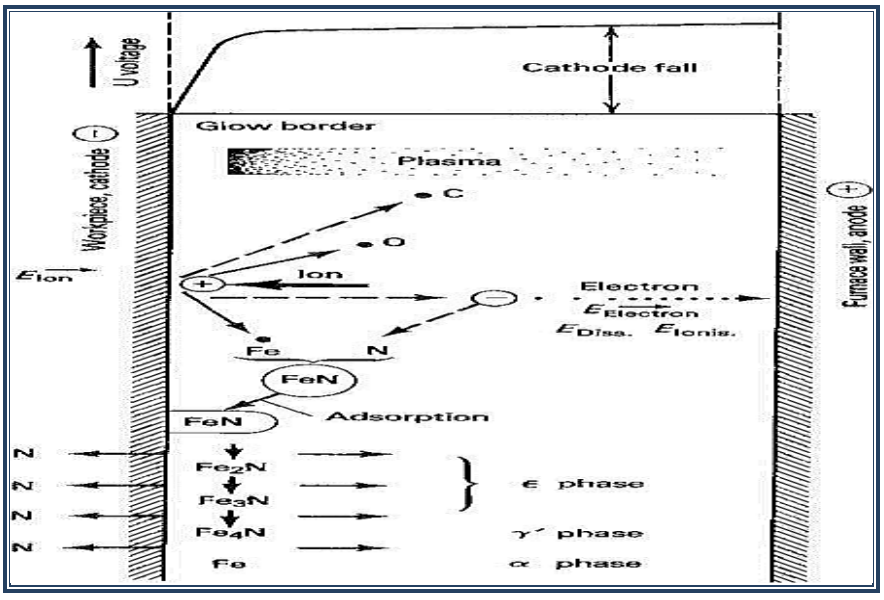

Figure 2.5 The proposed mechanism for plasma nitriding [77].

2.4.3.3 Parameters of Plasma Nitriding

There are several parameters influencing plasma nitriding process [77]:

- **Gas Mixture**

The usual gas mixture used for plasma nitriding is 25 % N_2 + 75 % H_2. If the nitrogen amount raises to 50 %, the growth rate of case is increased. Further increment in nitrogen amount results in the thickening of compound layer. The role of hydrogen in the nitriding process positive can be increased reaction rate, thickness of nitrided case, and density of active nitriding species in the plasma.

- **Temperature, Time, Pressure, and Plasma Power**

The parameters of nitriding are time, temperature, pressure and AC frequency. The temperature for plasma nitriding plays a key role in nitriding depth and should be in the range of 350–580 °C. Higher pressure positively influences corrosion resistance. As nitrogen content rises, it becomes more difficult due to the gradient of nitrogen concentration along the depth and, usually, the increase in the number of phases [78].

An increase in the thickness of the nitriding layer is observed with increasing treatment time. Lower treatment times generate a high concentration of nitrogen in the surface, which increases its hardness. As the treatment time is increased, the concentration of nitrogen on the surface decreased diffusing to the substrate, which causes the increase of diffusion depth. With the formation of the compounds layer, especially expanded austenite, compressive residual stresses are generated in the outermost layers of the material, increasing the wear resistance and hardness of the material [79].

Effective nitriding time was defined as the total actual nitriding duration minus the time required removing the passive layer from the surface. Longer duration of the chemical etching and lower stability of the passive layer (inferior corrosion property) were useful in obtaining the longer effective nitriding time and hence, higher thickness of the nitrided layer.

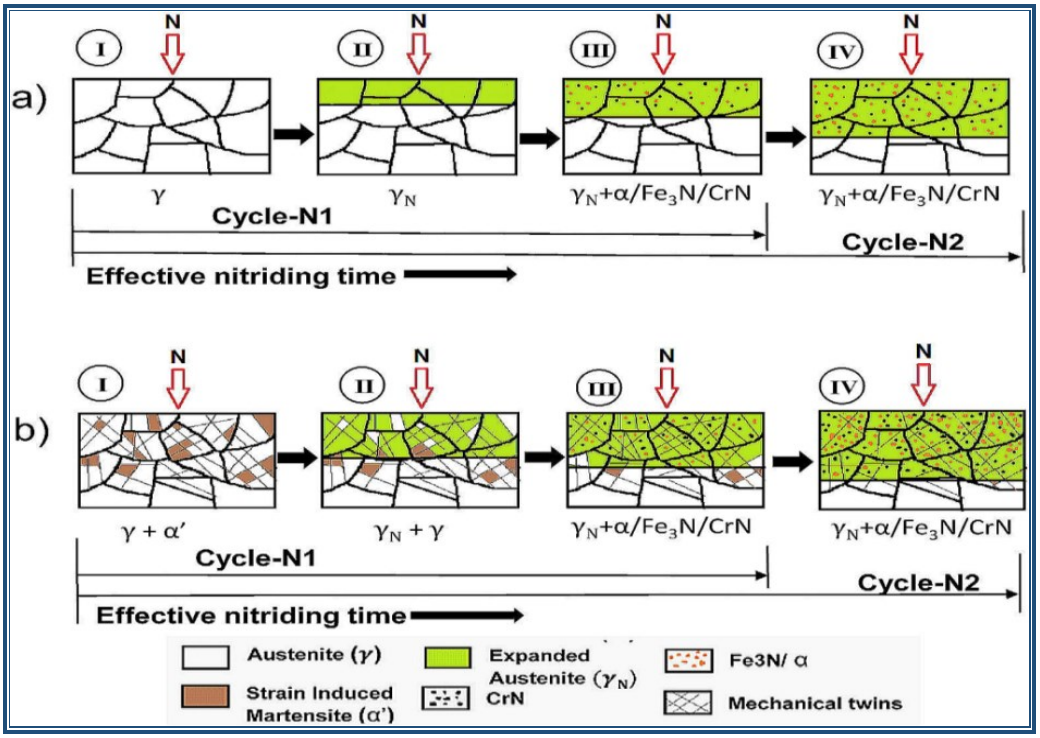

Figure 2.6 Schematic for the mechanism of nitrided layer formation and transformation in a) non-SMATed and b) SMATed AISI 304L steel specimens [80].

Higher effective nitriding time promoted the higher decomposition of γN phase into CrN, Fe_3N and α. The surface hardness of the nitride layer was decreased with the increase in the decomposition of γN phase (Figure 2.6) [80]. Increased treatment time significantly contributes to the formation of CrN. In addition, the formation of CrN in the nitride layer at a specific range of temperature and time could lead to increasing of hardness. The longer time and higher temperature of nitriding process has developed high amount of nitrogen element diffused in the nitride alloy layer of DSS. The N reacted with Cr to form CrN precipitate which led to the depletion of Cr

in the solid solution phase of the nitrided alloy layer and leads to the deterioration in corrosion resistance of DSS. The compound layer thickness increased by increasing the nitriding temperature and time [81].

2.4.3.4 Parts of a Plasma Nitriding System

As shown schematically in Figure 2.7, the main parts of a plasma nitriding system are a vacuum chamber, a power supply, and a process gas system with a gas-mixing panel or other mass flow controls. The power supply as the most important part of the system must provide an output voltage and an output current depending on the size of the vessel and workload. Arcing can occur in the form of an arc because the glow discharge process causes the removal of surface impurities, in which a sudden decrease in voltage and increase in current is occurred. The appropriate value of voltage and current density for plasma nitriding called "Glow discharge". To obtain this glow discharge in the nitriding process, the components to be treated are placed in the discharge vessel and charged to a potential of 400–1000 V, with respect to the wall of the vessel which acts as the anode of the circuit [77].

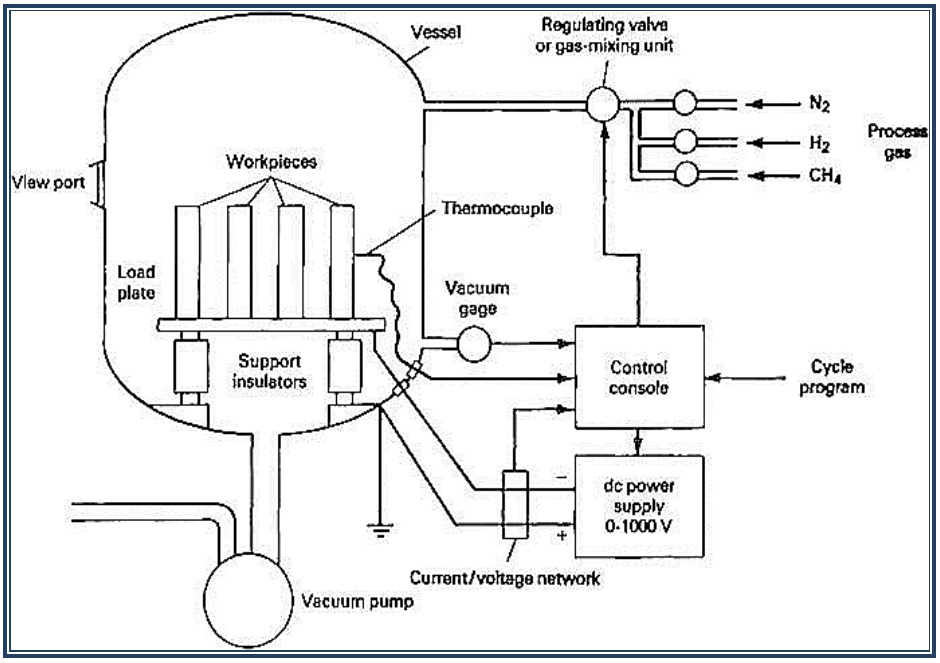

Figure 2.7 Parts of a typical plasma nitriding system [77].

2.4.3.5 Advantages and Disadvantages of Plasma Nitriding

Plasma nitriding has some advantages compared to other methods. Some of them are [82]:

1. Lowering the process time,
2. Lowering distortion and dimensional changes,
3. No need for final finishing processes,
4. Lowering the finished cost of process.
5. The surface homogeneity and uniformity of samples with complex geometry,
6. Harmlessness of plasma nitriding,
7. Fast kinetics of reaction at the surface and
8. Possibility to remove the oxide films before nitriding to accelerate nitrogen mass transfer from the plasma to the component.

There are also some problems for plasma nitriding method, as follows:

1. Need for handling of the process by skilled person,
2. The difficulty of processing big workloads with reproducible results,
3. Non uniformity of the temperature distribution within the workload,
4. The overheating of small parts and
5. Surface damage by arcing.

2.4.4 Surface Coatings with Tantalum based compounds (Pentoxide and Nitride)

The new implant and stent types coated by oxide and oxynitride coatings have excellent biocompatibility. Tantalum and tantalum-based compounds are promising for biomedical applications due to their good dielectric properties. The results of tests on implanting Ta in both soft and hard tissue of rats showed the good biocompatibility and osteogenesis of this metal. TaC and TaN materials possess relatively high hardness and demonstrate high corrosion resistance [83,84].

Bulk Ta suffers from high density and costs that restrict its applications. Therefore, tantalum oxide could be an appropriate substitute for tantalum owing to its lower ion release and toxicity, higher corrosion resistance, and better biocompatibility. Novel anticorrosion and antibacterial Ta_2O_5 coatings were successfully prepared and have minimal antibacterial activity. Ta_2O_5 coatings considered have the potential for extensive applications for orthopedic implants [85].

Tantalum possess mechanical properties similar to bones high hardness and flexibility. It is a highly ductile metal and forms a stable oxide component (TaO_2, Ta_2O_5) on its surface. Tantalum and oxygen is sputtered at the same time to attain tantalum oxide during deposition, the pure tantalum is chosen because its reaction with oxygen occurs faster. The corrosion resistance of Ta alloy was showing an improvement due to the more stable Ta_2O_5 passive films [86].

The bioactivity and biocompatibility of Ta stems from its ability to form a self-passivation surface oxide layer. From the perspective of orthopedic implants, this (Ta_2O_5) layer can facilitate the formation of a bone-like apatite coating thus allowing bone and fibrous in-growth and rapid attachment of bone and soft tissues. Moreover, Ta is one of the best anticorrosion metals due to the quick formation of an insulating Ta_2O_5 film. The Ta_2O_5 coating possessed excellent barrier in (SBF) [87].

Nitride coatings have also been tested as candidates to improve dental implants properties, including TiN, AlN, TaN and Cu- or Ag-doped TiN and TaN grown by magnetron sputtering, possibly combined with plasma nitriding. These coatings have been intended mainly to improve the osseointegration the protection against corrosion, and to reduce bacterial adhesion [88].

Ta is an excellent candidate for usage as a coating to improve its anticorrosion property and radiopacity. It was coated with excellent outcomes of good mechanical properties (high elastic modulus, high hardness value, low friction coefficient, high wear resistance) and chemical properties (high wettability, good corrosion resistance), so that it is of interest for joints presenting good biocompatibility and great longevity. Porous Ta is currently available for use in several orthopedic applications [89].

2.5 Surface Modification Technologies for Lean Duplex Stainless Steel

Surface modification of SS includes laser treatment, plasma modification, chemical and electrochemical treatment to obtain SS with certain properties such as roughness, hydrophilicity and corrosion resistance. Other surface modification techniques employ different physico-chemical methods. Hence, creating a micro- and nanostructured surface is another important method in surface modification of SS. Another way to increase the concentration of surface oxides consists in depositing metal oxides such as depositing TaO on SS implants [90].

Plasma nitriding of LDX at temperatures below 450◦C in a gas mixture of 25%N_2 and 75% H_2 forms a hardened surface layer with the thickness depending on the treatment temperatures. When low temperature plasma nitrided (T< 450 ◦C), the original austenite grains in the surface of the LDX forms the S-phase whilst "Fe_3N" were precipitated from nitrogen saturated ferrite grains [91].

Duplex stainless steel is usually employed in aggressive environments, the use of processing temperatures of 350 or 400 ◦C promoted the formation of only expanded austenite (γ_N), thereby

considerably increasing the corrosion potential and open circuit potential (OCP). Nitriding could be used to impart resistance to hydrogen embrittlement in DSS. The greater original hardness of DSS allowed it to better support the thin nitrided layer [92].

LDSS have been affected only by nitrides formation. Grade 2101 DSS only affected by Cr_2N nitrides precipitation, whereas a significant amount of the intermetallic σ-phase observed only in the high alloyed DSS. R-phase is not a structural anomaly but belongs to the equilibrium microstructure of all DSS (Figure 2.8). Nitrides formation is related to the variation of temperature of the ferrite solubility against nitrogen, which increases at high temperature, thus bringing ferrite in supersaturated solid-solution conditions [93].

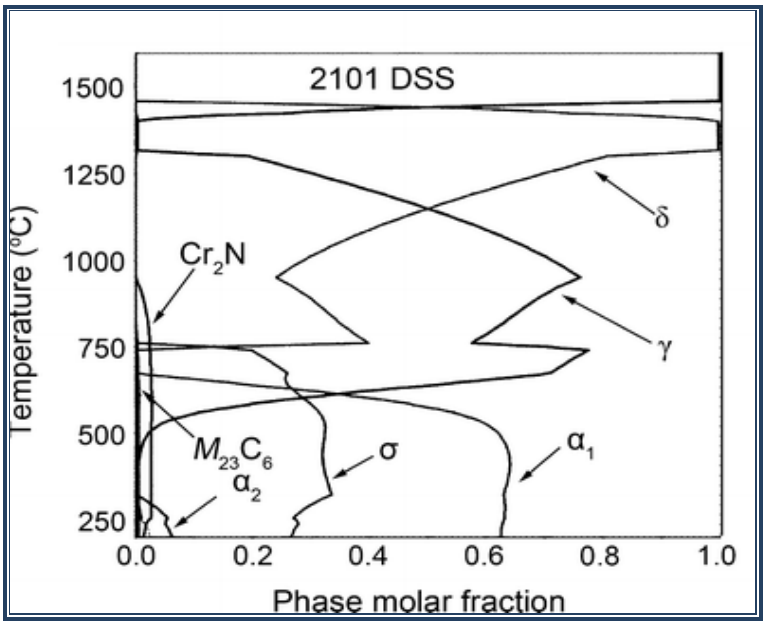

Figure 2.8 Equilibrium phase diagrams of LDX 2101 [93].

The passive film formed on SS in simulated physiological solutions is composed mainly of Cr and Fe oxides, with minor amounts of Ni and Mo oxides. The amount of Cr reaches a maximum in the outermost layer of the surface and decreases to a minimum, whereas the Fe concentration steadily increases until becoming constant. Both the thickness and nature of the

oxide on SS implants may change with time, depending on the location of the implant in the body [94].

The reasons for the different mechanical properties of the two phases of DSS are, first, the restoration mechanisms of ferrite and austenite during hot deformation differ. Ferrite has high stacking fault energy but, austenite has low stacking fault energy. Secondly, compared with BCC ferrite, FCC austenite has larger octahedral interstices; this leads to distribution of more interstitial solid-solution atoms in austenite than in ferrite [95].

A single S-phase layer on DSS is formed during low temperature nitriding. This requires the transformation from 'BCC" to "FCC" structure in the ferrite grains enriched with nitrogen. S-phase in the original austenite grains and αN and nitrides in the original ferrite grains are formed. At relatively low temperatures (<400 ◦C), a mixed phase (S-phase and αN) layer is more likely to form [96].

The increase of alloy contents not only improves the performances, but also promotes the precipitation of various secondary phases. These deleterious phases significantly deteriorate both the corrosion resistance and mechanical properties of the steel. The addition of N to SS not only facilitated the formation of finer precipitates but also promoted their uniform distribution in the steel. Increasing Cr and Mo content of SS could accelerate the precipitation of intermetallic phases [97].

Alloying N and C enhances the resistance to localized corrosion by strengthening the protectiveness of the passive film. Therefore, various SSs have been modified and newly developed by alloying N. The advantages of the alloying N can be manifested as long as they remain in solid solution state in the matrix. Because the alloyed N exceeding solubility limits is

prone to form Cr-consuming precipitates, such as Cr_2N and $Cr_{23}C_6$, which degrade both mechanical and corrosion properties [98].

The austenite stability adjusted by Mn, C, N and other alloying elements, such that the austenite transforms during deformation, with consequent increase in strength and elongation. As regards, resource-saving duplex stainless steel, which has higher N content and lower Mo content, high temperature austenite shows increased hardness because of increase of interstitial content, while ferrite at high temperature has low hardness. The increased difference in hardness significantly reduces the deformation compatibility of the two phases during hot deformation [99,100].

2.6 Corrosion of Duplex Stainless Steel

Typically, the excellent corrosion resistance of stainless steel mainly comes from its passivation. The passive film formed at high potential contains a much lower concentration of defects and provides better protection performance [101].

In the bio corrosion process, proteins are denatured and transform into a film on the metal surface, inhibiting corrosion. Fast or uncontrolled corrosion is accompanied by hydrogen and ion release and severe pH changes, which can lead to adverse biological reactions. Mechanical failure of orthopedic implants most frequently occurs due to fatigue. Structural changes in the film or variation in the ionic or electrical conductivity of the film alter the passive film resistance against corrosion. Presences of chloride ions essentially affects the corrosion of metallic implants where can easily penetrate the passive film due to their high diffusivity. Fluoride ions are also very corrosive. Protein adsorption inhibits the corrosion of metals, chiefly in two ways. First, the adsorbed protein layer forms a barrier between the electrolyte and the surface oxide layer, and resulting in

growth of the surface oxide. it is clear that proteins act as cathodic corrosion inhibitor. Second, the surface oxide contains negative charged oxide ions [36,37].

2.6.1 Corrosion Types of Duplex Stainless Steel

DSS showed the lowest corrosion rate. On the other hand, ferrite and austenite phases did not corrode uniformly. In DSSs, Cr, Ni, Mo, and N were not uniformly distributed between ferrite and austenite phases. This heterogeneity may lead to galvanic interactions, which result in a difference in corrosion behavior between these phases and can cause a preferential corrosion attack on the weakest phase. Ferrite was more active than austenite. Higher corrosion resistance of austenite in relation to ferrite phase attributed to a higher content of Ni in this phase. The release of metal ions was mainly from ferrite regions in a selective attack [102,103].

Galvanic corrosion takes place in direct physical contact with a dissimilar metal within an electrolyte such as serum or body fluid, especially in acidic pH environment. Amorphous oxide film has higher corrosion resistance compared to the polycrystalline oxide layer. The surface film crystalline defects act as active sites for corrosion. The absence of grain boundary, defects, and dislocations on amorphous oxide film provide the lowest current density and absence of breakdown potential. Addition of nitrogen increases resistance to pitting corrosion of stainless steels [104,105].

- **Pitting and Crevice Corrosion Resistance**

DSS can be characterized by a temperature above which pitting corrosion will initiate and propagate. This temperature is known as Critical Pitting Temperature (CPT). Pitting initiation below this temperature will not occur for long periods of time. Pit initiation is random, and the CPT is

sensitive to minor variations. The critical temperature for initiation of crevice corrosion is called the Critical Crevice Temperature (CCT). Generally; higher critical pitting or crevice corrosion temperatures indicate greater resistance to the initiation of these forms of corrosion. CPT and CCT of all grades of DSS are well above those of Type 316. This makes DSS a versatile preferred material. CPT = Constant + % Cr + 3.3 x % Mo + 16 x % N (Per IMOA guidelines) [104].

The pitting resistance of DSSs depends mainly on their Cr, Mo and N contents. Thus, the pitting corrosion resistance can be expressed in term of an empirical pitting resistance equivalent number (PREN) given by:

PREN = wt % Cr + 3.3 wt % Mo + *x* wt % N…… (9)

where the *x* value ranges from 16 to 30. Larger PREN value gives rise to higher pitting resistance. Partitioning of Cr and Mo in ferritic phase and of Ni and N in austenitic phase can affect the PREN values of both phases. Furthermore, the precipitation of secondary phase particles can cause compositional changes in the α- and γ-phases, resulting in selective pitting corrosion of a weak phase. Critical pitting temperature (CPT) is more appropriate to describe the susceptibility of stainless alloys to pitting corrosion. The ferrite volume fraction increases while the austenite fraction decreases with increasing temperature. Cr and Mo content in the α-phase decrease, while N content in the γ-phase increases, with increasing temperature. Accordingly, PREN value determined with $x = 20$ for the α-phase decreases, while that for the γ-phase rises by increasing the temperature. For lean UNS S32101 DSS contains very low Mo content, its pitting potential decreases with time that attributed to the formation of Cr_2N precipitates. Pits nucleate mainly at the Cr-depletion region around the Cr_2N precipitates, and then grow into ferritic grains. The reduction in

the passivation range, caused by the formation of α' phase, leads to serious pitting attack in the ferrite phase [104].

The resistance to the pitting corrosion gradually decreased as increase in α fraction. The phase fraction (α:γ) which exhibited the highest resistance to pitting corrosion was approximately 50:50 in all the DSSs. The pitting resistance equivalent numbers (PRENs) of α and γ phases in the DSSs (PRENα and PRENγ, respectively) is focused to explain the relation between the resistance to pitting corrosion and the phase fraction. The PREN values of the two phases become different. The overall resistance to the pitting corrosion of DSS determined by the pitting susceptibility level of less resistant phase than the other, which predicted by the PREN values of the two phases. Pitting corrosion occurred mostly at α phase adjacent to the γ phase and propagated into α phase. The more dissolved phase (the less noble phase) was α phase in all DSS. As α fraction increased, the average corrosion depth decreased. The pitting corrosion of DSS showed a stronger correlation with the galvanic corrosion rate between α and γ phases [106].

In practice, the pitting resistance equivalent (PRE) number is often used for comparing the pitting corrosion resistance of SS. The PRE number is between 34 and 35 for the austenite phase and around 41 for the ferrite matrix (without the nitride particles). This suggests a higher susceptibility of austenite, having lower PRE number, to initiate pitting corrosion than the ferrite phase at temperature above the CPT. The lower amount of Cr and Mo in the austenite phase could be a reason of its higher susceptibility to pitting corrosion compared to the ferrite phase [107].

- **Stress Corrosion Cracking**

DSS are replacements for austenitic grades in applications with a significantly lower risk of SCC. The presence of ferrite in DSS imparts the

superior chloride SCC resistance and high strength. Austenite in DSS provides higher resistance to aqueous corrosion and low temperature impact toughness.

The resistance of DSS to SCC is reduced by high temperature, low pH and high applied stress. The α-phase is more susceptible to SCC attack in hot chloride solutions, while the γ-phase is selectively attacked in hot alkaline sulfide solutions. Corrosion pits assist fine crack nucleation, causing selective dissolution of the α-phase. Preferential attack occurred at α-α and α-γ boundaries due to the formation of σ-phase in these regions. However, intermetallic phase and Cr-rich α'-precipitates are detrimental to the corrosion resistance of DSSs, especially for highly alloyed steels. The formation of these phases depletes Cr or Cr/Mo content in the matrix adjacent to the precipitates, leading to IGC, pitting corrosion and SCC [104].

- **Intergranular Corrosion**

The formation of intermetallic compounds, chromium nitrides and chromium carbides depletes Cr or both the Cr and Mo in DSS, leading to intergranular corrosion upon exposure to corrosive environments. Detrimental intermetallic phases in duplex stainless steel lead to low toughness and poor corrosion resistance [104].

2.6.2 Role of Alloying Elements in Duplex

• Chromium (Cr) – Ferrite Stabilizer – A minimum of 10.5% chromium is necessary to form a stable passive film to protect steel from mild atmospheric corrosion. The corrosion resistance is higher with increasing chromium content

• Molybdenum (Mo) – Ferrite Stabilizer – Molybdenum acts to support chromium to provide chloride corrosion resistance and resistance to pitting

corrosion; molybdenum also resists tendency to form detrimental intermetallic phases (e.g.: sigma, chi)

• Nickel (Ni) – Changes lattice structure from BCC to FCC; FCC gives excellent toughness; Ni additions help delay the formation of detrimental intermetallic phases. DSS do not have sufficient nickel to resist the strong reducing conditions

• Nitrogen (N_2) – Austenite Stabilizer – It delays formation of sigma phase; increases resistance to pitting and crevice corrosion; increases toughness; nitrogen is adjusted based on nickel content to achieve desired phase balance

• Manganese (Mn) – Somewhat controversial; stabilizes austenite, but may reduce pitting corrosion resistance [104,108].

2.7 Corrosion Resistance of Lean Duplex Stainless Steels

Lean Duplex stainless steel UNS S32101 and ASS 304L are showed similar breakdown potentials and pitting damage. There does not seem to be a universal relationship between PRE number and breakdown potential for the LDX and ASS. Lean DSS are also structurally stable and phases reform easily as result of nitrogen addition [108].

Corrosion resistance of LDX is similar to AISI 316L steel, but with the advantage of a yield limit two times superior to conventional austenitic grades. Lean duplex is much more susceptible to martensitic transformation, which can be explained by its lower Mo and Ni contents. Steels with PRE > 40 are super duplex, and those with PRE < 40 are duplex or “lean” duplex. LDSS have lower PRE than DSS because their Mo content is very low (less than 1.0%). A non-official boundary between LDSS and DSS is the PRE number of 30. The austenite of lean duplex

stainless steel was found to be as metastable as austenitic AISI 301LN grade, and more metastable than AISI 304L [34].

The dissolution of the microstructure of lean DSS during atmospheric corrosion seemed to spread preferentially along the outer surface rather than in depth. Pitting corrosion seemed to have been less favored apparent from minor localized forms of cavities, indicating corrosion attack occurred primarily by selective dissolution [109].

Localized corrosion occurs at the weakest parts of the LDX 2101 matrix. In general, equal volume fractions of phases, a defect-free microstructure, and no deleterious phases are required for LDX 2101 to have good corrosion resistance. LDX 2101 contains lower Mo, thus the precipitation of σ is more difficult. The resistance to pitting corrosion decreased gradually as the temperature increased from 950 C to 1100 C. [110-112].

With the temperature increasing, the change of chemical composition of each phase results in the PREN of ferrite phase decreasing while that of austenite phase increasing. But no equal PREN values in both phases were found in the alloy UNS S32101. Therefore, the pits are preferentially nucleated at austenite phase and restrained by ferrite phase. The pitting corrosion resistance is determined by the PREN value of the weaker phase [113].

The pitting corrosion resistance and the critical pitting temperature of LDSS have been found to be better than the standard austenitic types. LDSS, UNS S32101 has been very good resistance to stress corrosion cracking. Erosion can also be harmful to the pitting resistance of alloys especially if the re passivation rate is low. An increase in chromium content and an addition of N and Mo raises the re passivation rate. Mo containing alloy re passivates faster than without Mo. The LDSS UNS S32101 with

5wt% Mn is an alloy of interest due to the negative effect of Mn, in form of MnS inclusions; MnS (affect the pitting behavior). Mn is presented in the passive film of UNS S32101, likely to be preferentially oxidized and absorbed into the passive film formed on the austenite phase more than the dual phase of the lean duplex UNS S32101 [114].

2.8 The Body Environment

The human body consists of a significant number of natural elements with water. Where, about 96% of the available elements are oxygen, hydrogen, carbon and nitrogen. Additional ~ 4% of body mass comes in the form of bone minerals and blood composed of Ca, P, Mg and extracellular fluids comprising Na, Cl and K. As such, any implant developed on the basis of these elements would be compatible with the human body. However, there are few trace elements (trace elements) that are toxic at high levels [115].

Dissolved salts are probably the most influential components for implant corrosion in vivo. The most important characteristics of body fluids that influence the corrosion of metal implants are the chloride, dissolved oxygen and pH levels. Body fluids may seem to be slightly less aggressive than seawater, based on the lower (PREN) of 26 in comparison to the value of 40 for seawater. Indeed, deaerating of the solution with high-purity nitrogen gas to maintain low O_2 concentration was found to better predict the in vivo performance of metal implants. Another gas, carbon dioxide (CO_2), influences the corrosion in vivo by affecting the pH. The hydrogen evolution reaction (HER) and oxygen evolution reaction (OER) are two important reduction reactions in corrosion in vivo [116].

Artificial materials intended for clinical use are studied by in vivo and in vitro methods in simulated body fluids (SBF) to evaluate their

biocompatibility. In these model fluids, the ability of apatite formation on the surfaces can be tested. Most SBFs do not contain proteins, amino acids, or vitamins; only the inorganic ions of blood plasma are present in the same concentration as in the natural fluids as shown in Table (2.3). The tests may be either dynamic or static. Taking the constant flow of the body fluids into consideration, the dynamic method might be considered a better way to evaluate biocompatibility [117].

Table 2.2 Ionic concentrations of test solutions (in mM) [118-121].

Ions	Na^+	K^+	Mg^{2+}	Ca^{2+}	Cl^-	HCO^{3-}	HPO_4^{2-}	SO_4^{2-}
SBF	142.0	5.0	1.5	2.5	147.8	4.2	1.0	0.5
Ringers	156.4	5.6	-	2.2	161.8	2.4	-	-
PBS	138.7	3.1	-	-	139.7	-	2.03	-

2.9 Literature Review and Previous Study

2.9.1 Surface Modifications for Biomedical Applications

2.9.1.1 Different Surface Modifications on Stainless Steel

In 2015 He-Kyong Kang et.al [122]. This study investigated the biomechanical properties and bone-implant inter surface response of machined and laser surface-treated stainless steel (SS) mini-screw implants (MSIs). The mean values of Sa and Sq were significantly higher in the laser-treated group compared with the machined group (P <0.05). There were no significant differences in fracture resistance and BIC between the two groups. Laser treatment increased surface roughness without compromising fracture resistance. Despite increasing surface roughness, laser treatment did not improve BIC (the bone-implant contact).

In 2017 E.D.Gonzalez et.al [123]. Authors have proposed the use of Ti-Nb alloy thin films as surface coating for SS. Thin films were deposited on 316L SS substrate by magnetron sputtering, and four compositions were

produced: $Ti_{85}Nb_{15}$, $Ti_{80}Nb_{20}$, $Ti_{70}Nb_{30}$, and $Ti_{60}Nb_{40}$. The structure, morphology, and nanostructure of the coatings were analyzed by means of (XRD), (SEM), (TEM). The results showed lower elastic modulus values and higher hardness values as compared to commercially used alloys, as well as high values for joint plastic deformation between the coating and substrate.

In 2019 Viktoria Meyer-Kobbe et.al [124]. The objective of this study was to quantify the intraoral biofilm reduction on bracket material as a result of different surface modifications using silver ions. In addition to galvanic silver coating and (PVD), the plasma immersion ion implantation and deposition (PIIID) procedure was investigated for the first time within an orthodontic application. Orthodontic SS with a silver-modified surface by PIIID procedure showed an effective reduction in the intraoral biofilm formation compared to untreated bracket material. Additionally, the PIIID silver-modified surface has an increased bactericidal effect.

In 2020 A.M. Oje et.al [125]. Chromium oxide coatings deposited on stainless steel substrates by RF reactive magnetron sputtering were tested for their corrosion and ion release behavior in three physiological solutions. The coatings tested in Ringer's and Hank's solutions possess lower defect densities, better corrosion resistance, and lower ion release when compared to those tested in saline solutions. The metal ion release test suggests that the coatings have the potential to be used as an implantable coating for orthopedic implant applications.

2.9.1.2 Coatings with Tantalum based compounds (Pentoxide and Nitride)

In 2016 B. Rahmati et.al [86]. In this research, an attempt is made to study the corrosion and wear behavior of TaO_2 thin film coating deposited onto Ti-6Al-4V alloy by using physical vapor deposition magnetron

sputtering (PVDMS) with the highest adhesion which leads to increase corrosion resistance, decrease debris generation and improve durability. Corrosion testing was carried out in fetal bovine serum (FBS). The corrosion test in FBS medium confirmed that the corrosion resistance of the TaO_2 coated Ti-6Al-4V alloys was significantly higher than the uncoated Ti-6Al-4V substrate with high thin-film adhesion. The tests revealed that the specific wear ratio of TaO_2 coating was significantly lower than the uncoated substrate wear ratio. So, due to the noticeable corrosion and wear resistance characteristics of the TaO_2 coating, it is suggested for hip joint implant.

In 2016 Jian Cheng et.al [126]. In order to improve the corrosion and wear resistance of biomedical implants, a Ta_2N coating was synthesized on a Ti-6Al-4V alloy by the double glow discharge plasma process. The Ta_2N coating, improved the surface hardness and showed good contact damage tolerance and good adhesion strength to the substrate. The corrosion resistance of the Ta_2N coating in Ringer's physiological solution was evaluated by potentiodynamic polarization, electrochemical impedance spectroscopy (EIS), potentiostatic polarization and capacitance measurements (Mott-Schottky approach). The evolution of the surface composition of the passive films at different applied potentials was determined by X-ray photoelectron spectroscopy (XPS). The Ta_2N coating showed higher corrosion resistance than both commercially pure Ta and uncoated Ti-6Al-4V in this solution.

In 2018 Ay Ching Hee et.al [127]. Tantalum films were deposited on negatively biased Ti6Al4V substrates using filtered cathodic vacuum arc deposition. The effect of substrate voltage bias on the microstructure, mechanical and corrosion properties was examined and the cyto-compatibility of the deposited films was verified with mammalian cell

culturing. Ta/−100 V showed a significant improvement in corrosion resistance, which is attributed to the stable oxide layer. The results show that the Ta films have no adverse effect on mammalian cell adhesion and spreading proliferation.

In 2019 G. B. Melnikova et.al [128]. The research of structure, roughness and friction coefficients of tantalum and tantalum oxide coatings on steel and glass substrates by the AFM method is presented. The samples are characterized by low friction coefficients. These materials are proposed for fabrication of stents in medical applications.

In 2020 Hassan Jawad Farhan et.al [129]. Aim of study**:** to find materials which accelerate bone formation at bone implant interface and improve Osseo integration. Modified reactive plasma sputtering was used to coat CpTi with TaN at 4, 6 &8 hrs. Surface characterization by (XRD), (SEM), (EDS), contact angle measurement, were carried out for coated and uncoated disks. The results showed that 8 hrs coating time was the best time according to the results of XRD analysis. The results of wettability test for CpTi disk coated with TaN disk was more than wettability of non-coated CpTi disk. Surface roughness was more and better distributed in CpTi coated with TaN disk than non- coated one.

2.9.2 Plasma Nitriding

In 2015 J. Alphonsa et.al [130]. With a view to improve hardness and corrosion resistance of 2205 duplex stainless steel, plasma nitriding and nitro carburizing processes were performed at 350, 400, 450 and 500 ºC for 4 hrs. Samples treated at 400 ºC by plasma nitro carburizing exhibits the highest corrosion resistant with a significant raise in surface hardness. At higher temperatures, samples treated by these processes show poor

corrosion resistance. This study high lights the difference in plasma nitriding behavior of the ferrite and austenite phases.

In 2017 M A Maleque et.al [81]. The main aim of this work is to nitride alloy layer on the surface of duplex stainless steel by the nitriding process temperature of 400°C and 450°C at different time and ammonia composition using a horizontal tube furnace. After nitriding, it was observed that the hardness performance increased until 1100 Hv compared to substrate material of 250 Hv. The thickness layer of nitrided alloy also increased due to diffusion of nitrogen on the surface of DSS. XRD results showed that the nitride layer consists of iron nitride, expanded austenite and chromium nitride. It can be concluded that nitride alloy layer can be produced via nitriding process with significant improvement of microstructural and hardness properties.

In 2019 Giuseppe Pintaude et.al [92]. Two grades of DSS, SAF 2205 and SAF 2507, were nitrided using an active screen plasma process carried out at 380 ◦C for 10 hrs. X-ray diffractometer showed expanded austenite formation in all nitrided samples. The super duplex steel SAF 2507 showed much better scratch resistance, with low friction coefficient and greater toughness. The corrosion behavior of duplex steels was also different, and nitriding had a more beneficial effect upon SAF 2507.

In 2019 Ali Sabea Hammood et.al [131]. In this thesis the plasma nitriding process was done for a titanium alloy (Ti–6Al–4V) rod and performed at different nitriding times (5, 10, and 15 hrs), and the effect of plasma nitriding was examined on the chemical compassion of the alloy and phases were studied by (OM), (SEM) and (FESEM), (XRD), Tafel potential polarization, and cyclic polarization. The results indicate that the formation of layers and phases Ti_2N and Ti_2N_{3-x} on a surface of the alloy

were achieved, which would improve the chemical corrosion in simulated body fluid.

In 2020 Alisiya Biserova-Tahchieva et.al [132]. In this study, the effect of a plasma ion carburizing process to (DSS and SDSS), at 925 ◦C for a long time is presented. The objective is to analyze the diffusion elements' influence on the precipitation of secondary phases after additional short thermal treatment. Precipitation of secondary phases—sigma, chi, nitrides and carbides—seemed to occur during the treatments in a similar way for both (DSS and SDSS). It was found that an improvement of the surface protection after the plasma carburizing process occurred.

In 2020 XIAO TAO et.al [133]. In this article, Invar_36 (Fe-36Ni, in wt pct), is characterized after triode plasma nitriding (TPN) treatments at 400◦C to 450◦C and compared with a RA 330® (Fe-19Cr-35Ni, in wt pct) treated under equivalent nitriding conditions. Cr does indeed appear to play a pivotal role in colossal nitrogen super saturation of austenitic steel under low-temperature (≤ 450 ◦C) nitrogen diffusion. Nevertheless, this work reveals that nitrogen-induced lattice expansion occurs below the nitride-containing surface layer in Invar 36 alloy after TPN treatment, implying that Cr is not a necessity for the nitrogen-interstitial induced lattice expansion to occur.

2.9.3 Duplex Stainless Steel

In 2015 M.E. Sotomayor et.al [134]. Purpose of this paper is the evaluation of three different surface treatments on a duplex stainless steel, in order to improve its adhesive properties on a thermoplastic like polysulfide. Shot-peening, acid (aquaria) etching and atmospheric pressure plasma jet have been used. Additionally, aging studies have been performed to evaluate the effect of storage time of parts on atmospheric plasma torch surface treatment. Aquaria and plasma torch treatments have

reached the optimal surface modification condition under wettability criteria. Shear strength tests demonstrated that the improved surface adhesion provided on this substrate and the polysulfide is achieved by shot-peening and acid etching treatments.

In 2015 Margarita Bobadilla et.al [135]. In this work, DSS samples were plasma nitrided at temperatures between 350 °C and 500 °C for 240 min under an atmosphere of 75% N_2 + 25% H_2. Apparent diffusion coefficients, activation energy and pre-exponential constant were calculates using the first law of Fick for each material phase, austenite and ferrite. Nitrogen diffusion in both phases appears to be similar. Nevertheless, the difference on the layer thickness in both of the phases is small. From these results, it was proposed a model of nitrogen diffusion into a two-phase stainless steel to explain the morphology of the interface between the layer and the substrate.

In 2016 R. W. Gregorutti et.al [136]. Mechanical, electrochemical and magnetic properties of DSS were analyzed to evaluate its use as biomaterial, comparing the results with those obtained for ASS. Yield and ultimate tensile strengths are almost twice in DSS. The electrochemical test revealed that this material has lower susceptibility to localized corrosion because of its greater passive range. Both steels behave as soft magnetic materials; however, DSS has higher magnetic saturation, while ASS is more prone to heating when exposed to a magnetic field.

In 2017 Ali Sabea Hammood et.al [137]. In the present study, the corrosion resistance of a DSS in artificial saliva was studied by potentiodynamic measurements. The microstructure was investigated by (SEM), (XRD) and (HV). The properties were tested in thermally treated conditions (800-900°C, 2-8 min). The research aims to evaluate the capability of DSS for orthodontic applications. The results indicate that the

corrosion resistance is mainly affected by the ferrite /austenite ratio. The best result was obtained with a treatment at 900°C for 2 min.

In 2017 P.H. Lailatula et.al [138]. Surface modification of duplex stainless steel is important to make this material suitable for tribological and high temperature applications. The surface modification using fine SiC (20 μm) powder preplacement by TIG torch technique has been performed on DSS. The TIG torch was employed with varying operating welding variables such as welding current of 80 A, 90 A and 100 A and energy input of 648, 768 and 1440 J/mm. The composite surface layer was characterized using Vickers micro-hardness tester and (SEM). Based on the results, it was found that re-solidified composite layer produced maximum hardness of 833.6 Hv from substrate hardness for TIG processed of 768 J/mm energy input. The microstructure revealed the formation of dendrite phase due to complete melting of SiC in the modified layer.

In 2019 Alisiya Biserova Tahchieva et.al [139]. The paper presents an overview of diffusion surface treatments, especially nitriding processes, applied to duplex and super duplex stainless steels in the last five years. Research has been done mainly to investigate different nitriding processes in order to optimize parameters for the most appropriate procedure. The scope has been to improve mechanical and wear resistance without prejudice to the corrosion properties of the duplex and super duplex stainless steels.

In 2020 G. Lakshmi Prasanna et.al [140]. This paper analyzes a study of the impact of carburizing on DSS. The main focus is on increasing the hardness and wear ability without sacrificing the resistance to corrosion will significantly extend its applications. With regard to various metallographic and mechanical tests, these heat treated materials were analyzed. Metallographic measures such as XRD, SEM, and mechanical

tests such as tensile and hardness tests are the most commonly used. The paper discusses structural and physical changes in duplex stainless steel.

In 2021 Ali Sabea Hammood et.al [141]. This paper reports on electrophoretic deposition (EPD) of hydroxyapatite / titania nanocomposite coatings on 2205 (DSS). The effects of using deposition voltages of 20 V, 30 V, and 40 V on the kinetics during EPD were identified. The corrosion behavior of coated and uncoated samples was studied in Ringer's solution using potentiodynamic and cyclic polarization tests. A homogeneous morphology and crack-free structure were obtained at the optimum condition of 30 V, with minimum porosity and the highest corrosion resistance. The results confirm that these materials suitable for use in medical applications.

In 2021 Ali Sabea Hammood et.al [142]. This thesis indicates that Hydroxyapatite-Silver (HAp/AgNPS) coating on 2507 (DSS) by electrophoretic deposition (EPD) process was done. The ideal EPD parameters for good 2507 DSS coating were 20 V and 3 min. The corrosion results showed that all 2507 DSS coated samples had a lesser corrosion current density in solution (Ringer) at 37 ◦C than the 2507 DSS uncoated sample, while antibacterial results indicate that AgNPS play an effective role in destroying and inhibiting bacteria.

2.9.4 2101 Lean Duplex Stainless Steel

In 2015 Zhi-hui Feng et.al [143]. The microstructure, micro hardness, phase ratio, and recrystallization dependence of the deformation compatibility of LDX 2101 and DSS 2205 were investigated using (OM), electron backscatter diffraction (EBSD), Thermo - Calc software, and (TEM). The results showed that the phase ratio transformations of LDX 2101 and DSS 2205 were almost equal under the condition of increasing solution temperature. Thus, the phase transformation was not the main

cause for the hot plasticity difference of these two steels. The grain size of LDX 2101 was substantially greater than that of DSS 2205, and the micro hardness difference of LDX 2101 was larger than that of DSS 2205.

In 2016 Alberto Ruiz et.al [144]. In this paper, welded joint of a 2101 lean duplex stainless steel (DSS) was studied using ultrasonic attenuation measurements. Two plates were welded using gas metal arc welding (GMAW) process. Experimental measurements show that the longitudinal ultrasonic wave amplitude is significantly affected by the recrystallization of the microstructure caused by multi-pass welding. Similarly, it was found from Vickers micro hardness maps, that finer microstructure shows higher micro hardness values while coarser grains present the lower values.

In 2016 Jean-Yves Maetz et.al [145]. The microstructural evolution of a 2101 lean duplex stainless steel (DSS) during isothermal aging from room temperature to 470 °C was investigated using thermoelectric power (TEP) measurements to follow the kinetics, atom probe tomography, and transmission electron microscopy. The time–temperature pairs characteristic of the early stages of ferrite decomposition were determined from the TEP kinetics.

In 2018 A. A. H. Ameri et.al [146]. The effect of strain rate on the mechanical response and microstructural evolution of Lean Duplex Stainless Steel 2101 (LDSS 2101) has been investigated. The compressive response of LDSS 2101 at different strain rates was measured by using a universal testing machine and Split Hopkinson Pressure Bar (SHPB). The microstructural changes were examined using OM, ESM and Electron Backscatter Diffraction (EBSD). The results showed that the mechanical response of LDSS 2101 depends on strain rate. Microstructural observations revealed that some of the austenite phase transforms to

martensite. The volume fraction of the martensitic phase, increases with increasing plastic strain but decreases with increasing strain rate.

In 2018 Franc Tehovnik et.al [147]. The purpose of the research was to qualitatively analyze the phases in 2101 lean duplex stainless steel after thermal aging. (OM), (SEM) and electron-backscatter diffraction (EBSD) were used to investigate the structural stability and the chemical compositions of the phases.

In 2019 Masoud Atapour et.al [148]. Changes in corrosion behavior, metal release, and surface composition of austenitic (AISI 316L), ferritic (AISI 430), and lean duplex (LDX 2101) stainless steels in simulated milk (SMS) and whey protein solution were investigated. The amount of released metals and the corrosion susceptibility increased according to 2101 < 316L < 430. All grades revealed low corrosion rates in the whey protein solution without any sign of active/metastable corrosion. The total amount of released metals (iron, chromium, and nickel) was significantly higher in whey protein solution compared with SMS. Nickel was preferentially released compared to its bulk composition fraction for both 316L and 2101 in the highly complexing SMS. Reduced metal release rates with time correlated with the enrichment of chromium in the surface oxide.

Chapter Three

Experimental Part

3.1 Introduction

This chapter comprises the materials that were used and preparation of these materials and the experimental procedures. The experimental part of this investigation will contain the following:

- Materials used in this study
- Sample preparation for surface modifications and tests
- Experiments and performance methods

3.2 Raw Material

The alloy used in this work was rod of LDX 2101 lean duplex stainless steel (Figure 3.1) which made in Sweden OutoKumpu factory for stainless steel and high performance alloys. The analysis of chemical compositions for this alloy is displayed in Table (3.1). This test was performed in Al Nabaa Co. Engineering Services Labs in Baghdad which is agreed with OutoKumpu data of chemical compositions for LDX "2101" [149].

Figure 3.1 A sample prepared experimentally.

Table 3.1 Chemical composition analysis for LDX "2101" alloy in wt%.

LDX 2101 stainless steel alloy	EN	ASTM	C	Cr	Ni	Si	Mo	N	Others	Fe
	1.4162	S32101	0.03	21.5	1.5	1	0.3	0.22	5Mn Cu	Bal

Figure 3.2 shows illustrates the "flow chart" of the present study of the presented investigation.

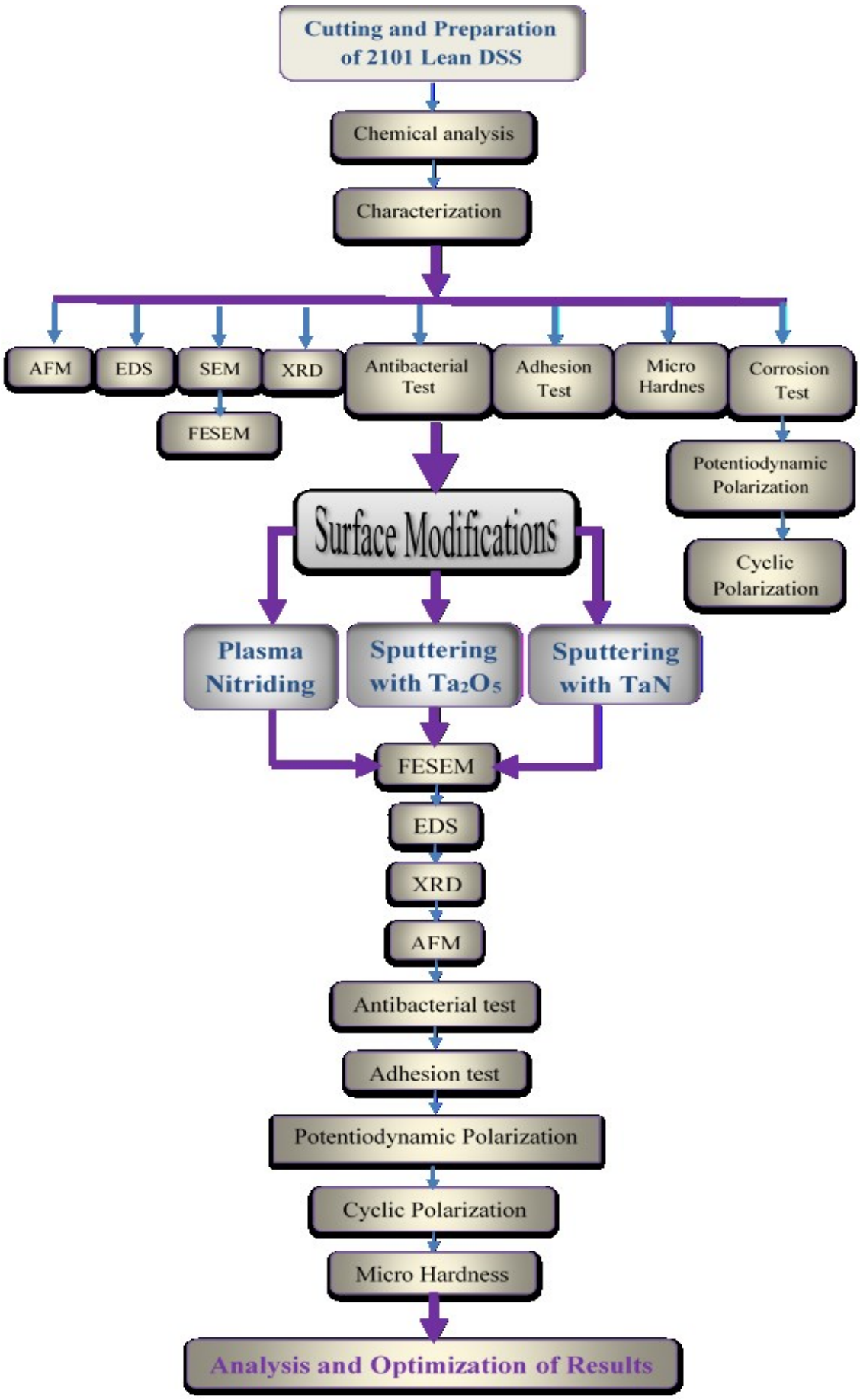

Figure 3.2 Flow chart of the study

3.3 Samples Preparation

The first step to prepare the samples for surface modifications was cut a rod of LDX 2101 alloy into samples with dimensions of (φ15x5) mm to three sets. Each set contained five samples, which were then ground with silicon carbide papers, and rinsed in refined water before polishing using the grinding and polishing machine (Meta Serv. 250). After polishing is completed, the samples were ultrasonically cleaned by ethanol medium for 10 min to remove any impurities from the surface.

3.4 Surface Modifications Techniques

From the material as received, the surface modification will consist of three parts:

3.4.1 First Part: Plasma Nitriding Technique

The plasma nitriding procedure was performed on mirror polished finished LDX 2101 DSS samples for different nitriding times (5, 10, 15, 20 and 25) hrs in plasma nitriding system. This was a low-pressure gas discharge unit consisting of a vacuum chamber with two parallel electrodes. The plasma chamber contains a target (cathode) and anode disk of stainless steel. The cathode faces the anode, which provides an electric field for the gas to be discharged. The bottom shaft of the cathode electrode is shielded by insulator disk (ceramic). The top of cathode is shielded by cathode space assembly which included by ceramics insulator and stainless steel holder. The diameter of the top electrode is 14.5 cm while the target electrode (effective area of cathode dark space) is 7.5 cm and the gap distance between them can be varied from 4 to 6 cm and in the current study a 4 cm distance is used. The feeding of N gas was done after evacuating the process chamber to high vacuum ($\approx 1 \times 10^{-5}$ mbar) using high vacuum system consisting of rotary and turbo molecular vacuum pumps to ensure the complete removal of the heavy gases like

hydrocarbons. A 4 kV DC voltage–power supply is used to ensure the necessary voltage for plasma nitriding and the discharge voltage was 400 V. The plasma nitriding process was performed in 3 mbar pressure of nitrogen. The clean samples are placed on the anode in the center of the dark shield as shown in Figure 3.3. The cathode was connected to the DC power supply, while the grounded chamber served as anode. After the process was finished, switch off voltage power supply and aeration the chamber in nitrogen gas to purpose reduce the pressure inter the vacuum chamber and exit the samples.

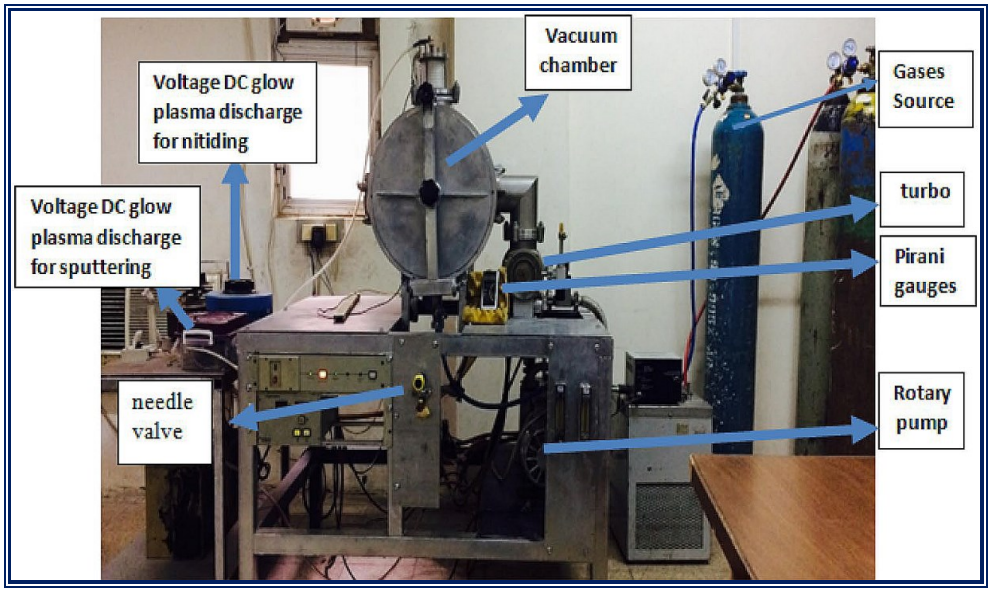

Figure 3.3 The plasma nitriding system (design and made locally).

Plasma nitriding for DSS (2101) at different times (5, 10, 15, 20, 25) hrs, voltage (400 V), current (30 mA) and pressure (3 mbar).

1- Preparation of samples from modern LDX (2101). 5 samples with (φ15 x5) mm dimensions.

2- Optimization of plasma nitriding process parameters: time, voltage, current and pressure, with several gases in order to use N_2.

3- Samples nitriding, by different nirtiding times and stay the other parameters invariant.

3.4.2 Second Part: Ta – Pentoxide Deposition by Reactive Sputtering Technique

Ta – Pentoxide deposition by sputtering at different sputtering times (2, 4. 6, 8, 10) hrs and voltage of (3500 V), current of (10 mA) and power of (35 W).

1- Preparation of samples from modern LDX (2101) (5 samples with (φ15x5) mm) dimensions.

2- Optimization of Ta_2O_5 reactive sputtering process parameters time, current and power.

3- Samples sputtering by different times and hold other parameters constant.

3.4.3 Third Part: Ta – Nitride Deposition by Reactive Sputtering Technique

Ta – Nitride deposition by sputtering at different sputtering times (2, 4. 6, 8, 10) hrs and voltage of (3500 V), current of (10 mA) and power of (35 W).

1- Prepare samples from modern LDX (2101) (5 samples with (φ15x5) mm) dimensions.

2- Apply the optimized process parameters of sputtering Ta – Nitride method.

3.5 Surface Characterization Processes

A brief description of the various techniques used for the characterization of the alloys is given in the following sections:

3.5.1 Vickers Micro Hardness Test

The hardness test can detect any changes in microstructures that are not related to varying chemical compositions. The test was accomplished at the University of Kufa – Faculty of Engineering– Materials Engineering Department. It was performed by using a "digital calibrated Vickers" micro

hardness testing machine, "TH715", "Beijing Time High Technology Ltd., China), equipped with microscopic lenses with amplification of 400 X and 100 X and according to ASTM E 384–99 (standard test technique for materials micro indentation hardness), to test samples at 9.8 N load and 15 sec before and after surface modifications. The hardness readings were taken five times in different regions and then the average of these readings were recorded for the sample before and after surface modifications.

3.5.2 Field Emission Scanning Electron Microscopy

Scanning electron microscopy (SEM) is used to identify microstructural features associated with the ferrite and austenite phases and also secondary phases. The test was performed for LDX 2101 in "Al-Razi Metallurgy Research Center" in Tehran by using FESEM kind (MIRA 3-XMU) (Figure 3.4) and "CAC Chemistry Analysis Center" in Baghdad.

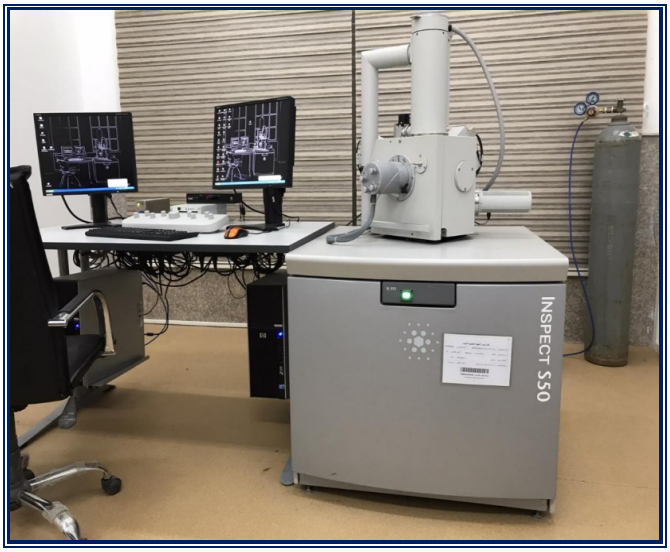

Figure 3.4 Field Emission Scanning Electron Microscopy.

3.5.3 Energy Dispersive Spectroscopy

Energy dispersive spectroscopy (EDS) analysis (attached to SEM) is one method to evaluate the chemical composition of each phase. Doing three spectrums by SEM for each phase (one sample), then calculating the mean value of weight percentage for each element and the minimum and maximum values for each element in the phases.

3.5.4 X-Ray Diffraction

X-ray diffraction (XRD) techniques is used method to define the presence phases in LDX 2101 alloy before and after the surface modifications. The "SHIMADZU Lab X XRD-6000", Japan X-Ray machine used in this thesis (Figure 3.5). The tests were accomplished at the Al-Razi Metallurgy Research Center in Tehran and the CAC Chemistry Analysis Center in Baghdad. X-ray with a nickel filter and generator copper Kα radiation (λ = 1.5406). The scanning speed of the diffract meter was adjusted to 60 per min with the diffraction angle range 2θº was (40º-100º). The resulting peaks are then compared to standard peaks for each phase that will appear in the Lean Duplex stainless steel alloy and phases that will appear as a result of surface modifications.

Figure 3.5 X-ray diffraction SHIMADZU Lab X XRD-6000.

3.5.5 Atomic Force Microscopy

The surface image feature, particle size in addition nano roughness of the deposition layer is observed with the atomic force microscope (AFM). AFM is a beneficial tool used to detect the arrangement of nanoparticles and providing high resolution topographies of coated films. This technique is very effective for characterizing the material in the nano scale. This test performed in the University of Babylon-Faculty of Materials Engineering

by using AFM (Figure 3.6) (SPM AA3000, Angstrom Advanced Inc., USA).

Figure 3.6 Atomic force microscopy (AFM).

3.5.6 Antibacterial Test

The risk of initial Microbial Colonization and bacterial attack exists on the surface of biomaterial. The activity of antibacterial of the surface layer of modified LDX was investigated to evaluate whether the coated layer is antibacterial or not. The activity of antibacterial is studied by using the inhibition zone method. An antibacterial kinetic test with bacterial strains of *"E.coli"* (Escherichia coli, American type culture, "ATCC 25922", gram negative bacteria, is prepared at the University of Kufa - Faculty of Medicine - Microbiology Department [150]. The *E.coli* grown on a (N. agar) "nutrient agar" and placed in the incubator for 24 hrs, then the bacteria spread on a petri dish and incubated at 37˚C for 24 hrs as seen in Figure 3.7, after that, the samples are placed in four different regions on the petri dish and the inhibition zones are observed.

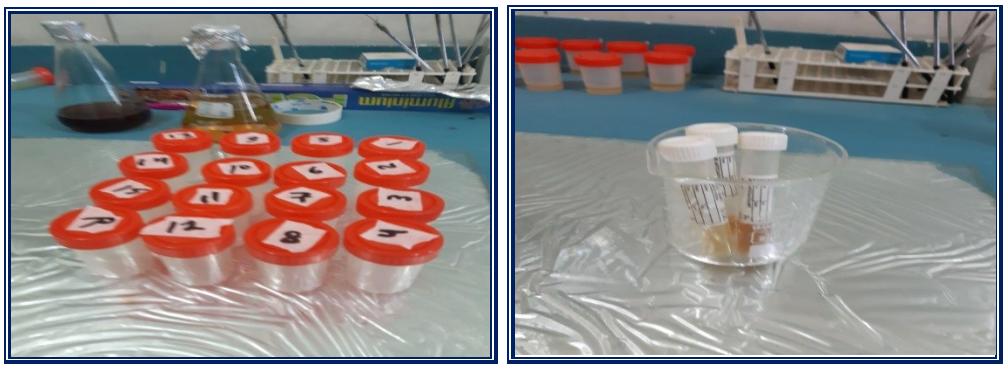

Figure 3.7 Anti-bacterial test samples

3.5.7 Adhesion Test

The adhesion test was performed using the Rockwell-C adhesion test, which uses a standard Rockwell hardness tester fitted with a Rockwell (type - C) diamond cone and a load of (150 kg) at 2 sec. Adhesion types as (HF1-HF6) ratio to the cracking level and plating delamination about the indented in Figure 3.8. Adequate adhesion is denoted by the indented classifications ("HF1" and "HF2") [151]. Rockwell hardness test was performed on LDX 2101 DSS substrate and nitrided samples at the Faculty of Engineering labs / Kufa University.

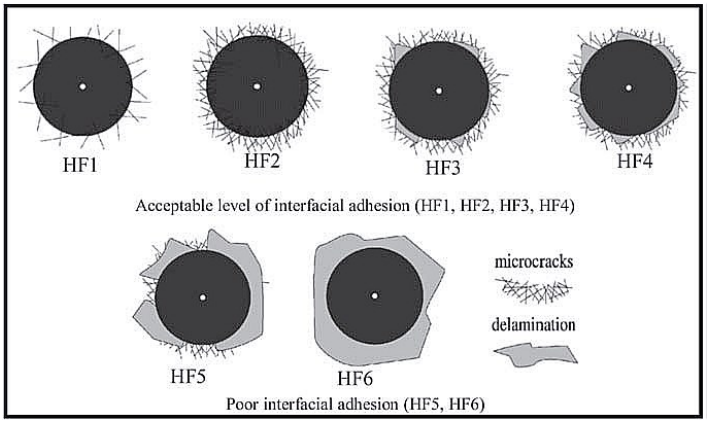

Figure 3.8 The adhesion test planner for Rockwell-C [151]

3.5.8 Electrochemical Corrosion Test

The electrochemical corrosion tests have been studied for the samples, before and after surface modifications, by polarization tests (potentiodynamic and cyclic). These tests are done in "Ringer's solution" (chemical composition detailed in Table 3.2). This test is performed by

utilizing potentiostats/galvanostats (MLab Bank Elektronik, Germany (Figure 3.9) at University of Technology–Production Engineering and Metallurgy Department. There are three electrodes in the corrosion cell.:

1. The electrode of working "LDX 2101 sample".
2. The counter electrode (platinum rod).
3. The saturated calomel electrode (SCE).

The exposed surface area was (1 cm^2) for the electrode of working where used for all samples.

Table 3.2 Chemical Composition of "Ringer's solution"

Component	Concentration (g/L)
NaCl	8.60
KCl	0.30
$CaCl_2.2H_2O$	0.33
pH	7.4
Na^+	147.5
K^+	4.0
Ca^-	4.5
Cl^-	156.0

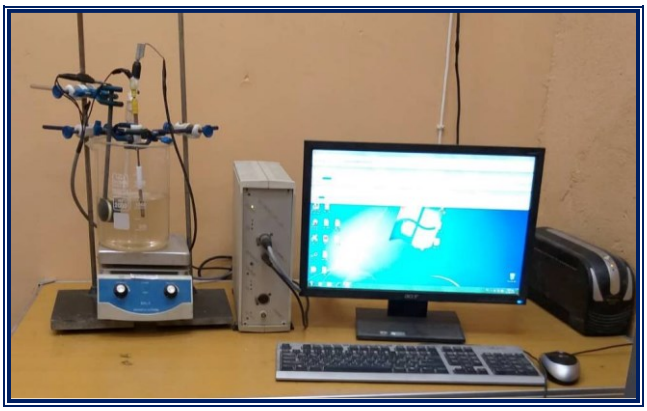

Figure 3.9 The electrochemical Corrosion Test System.

The corrosion rate (CR) was calculated by using Faraday's law in mpy unit according to the ASTM G102 − 89 [152]:

$$\mathbf{CR = K \frac{icorr\ W}{\rho * n}} \quad \text{..... Eq (3.1)}$$

Where:

K: Constant equal to 0.1288.

i_{corr}: Corrosion current density µA/cm^2.

W: Elements atomic weight.

ρ : Density of the alloy, which is calculated practically for LDX 2101 DSS and its value equal to 7.3 g/cm^3.

n: The required number of electrons to oxidize the element atom in the corrosion process or it is the valence of the element (n = 2 for DSS).

3.5.8.1 Potentiodynamic Polarization

In this work, the corrosion behavior was analyzed for LDX 2101 duplex stainless steel before and after surface modifications by using electrochemical cell (three-electrode). Polarization tests were done in potentiostat type "Winking M Lab 200". The curves of potentiodynamic polarization were plotted then Tafel plots were used to determine both the corrosion potential (Ecorr) and the corrosion current density (Icorr) using both anodic and cathodic polarization branches, the tests were done in "Ringer's solution" at 37 °C.

Polarization resistance was characterized as the resistance of the specimen to oxidation, during the application of an external potential. Based on the Sterne-Geary formula provided by Eq. (3.3) [152], Rp values were calculated: [153]

$$\boldsymbol{Rp = \frac{\beta a\, \beta c}{2.3\ Icorr\ (\beta a + \beta c)}} \quad \text{.....Eq. (3.3)}$$

Where:

β a: Anodic Tafel slope.

β c: Cathodic Tafel slope.

3.5.8.2 Cyclic Potentiodynamic Polarization

The cyclic potentiodynamic polarization method gives a reasonable, rapid technique for qualitatively predicting the propensity of an alloy or metal to suffer localized corrosion in the form of pitting. The test performed in the same system used in the potentiodynamic polarization shown in (Figure 3.8) and same conditions and test parameters. The test performed for LDX 2101 before and after surface modifications.

Chapter Four

Results & Discussion

4.1 Introduction

This chapter offers the results that have been inferred from the practical part, mechanical, physical and chemical tests followed by their discussion. The results are presented and discussed to demonstrate the effect of surface modifications type and its parameters (such as treatment time) on the mechanical and surface properties, antibacterial activity, adhesion strength in addition corrosion resistance of deposited layer was studied in vitro by "Ringer's solution" (simulated body fluid) at temperature 37 ±1 °C.

In this chapter also results of surface modifications processes with optimum conditions are extracted from statistical analyses.

4.2 Microstructure of LDX 2101 DSS Substrate

LDX 2101 duplex stainless steel before surface modifications has microstructure of biphasic, with darker ferritic and brighter austenitic phase grains in approximately area fraction of 50.6 % ferrite (α) and 49.4 % austenite (γ) without secondary phases (Figure 4.1), that calculated by using Image J-1.46r program [154].

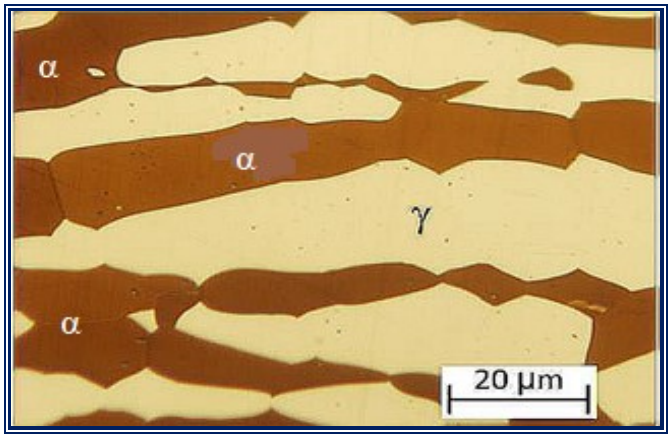

Figure 4.1 Initial microstructure of LDX 2101 duplex stainless steel, with ferrite (dark) and austenite (light) phases.

4.3 Surface Characterization Techniques after Surface Modifications

Part I: Plasma Nitriding Technique

4.3.1 Vickers Micro Hardness Test

The average micro-hardness for the un nitrided 2101 LDSS substrate at five different regions is 260 HV, which is equal to the hardness of LDSS 260 HV [155]. The surface hardness is increased due to the nitrogen diffusion into the crystal lattice by plasma nitriding [156].

The precipitates, that form nitrides, distort the lattice and pin crystal dislocations, significantly increasing the material's hardness. The super saturation of N in solid solution and precipitation of "nitride" result in very high micro hardness values. By employing active nitrogen diffusion for nitriding times less than "10 hrs", the ferrite in sample surface may be transformed to austenite, and the "expanded austenite" was the main phase in the nitriding layer "S phase". By the nitrogen atoms infusion, the region of pre-existing ferrite transformed into "S phase", most of atoms remain in interstitial positions. Little pre-existing ferrite was decomposed and Ɛ-nitride precipitated in "S phase" whenever time of nitriding was prolonged to 16 hrs. When time of nitriding was extended, a great amount of "Ɛ-nitride", also "CrN" precipitates were found in pre-existing ferritic zone (expanded austenite). In addition, from pre-austenite region, several nitrides precipitated [157]. At an initial stage of nitriding treatment, nitrogen atoms are dissolve into the α and γ, causing its lattice expansion, which improves the surface hardness of DSS. Besides, nitrogen atoms combine with alloy elements to form nitrides (CrN and $Fe_{2-3}N$), which significantly enhances its surface hardness. When the surface layer reaches a certain thickness, the diffusion resistance of nitrogen atoms increases, and the degree of lattice distortion and the amount of nitrides have un obvious increase, the surface hardness of the treated sample reaches the maximum.

With prolonged nitriding time, nitrides grow and coarsen, which causes the decrease of surface hardness instead in samples 4 (20 hrs) and 5 (25 hrs) as shown in Figure (4.2) which is match with references [158,159]. Increased nitriding time (up to 15 hrs) results in a decrease in nano-hardness, which may be attributed to increased particle size produced by longer nitriding [160].

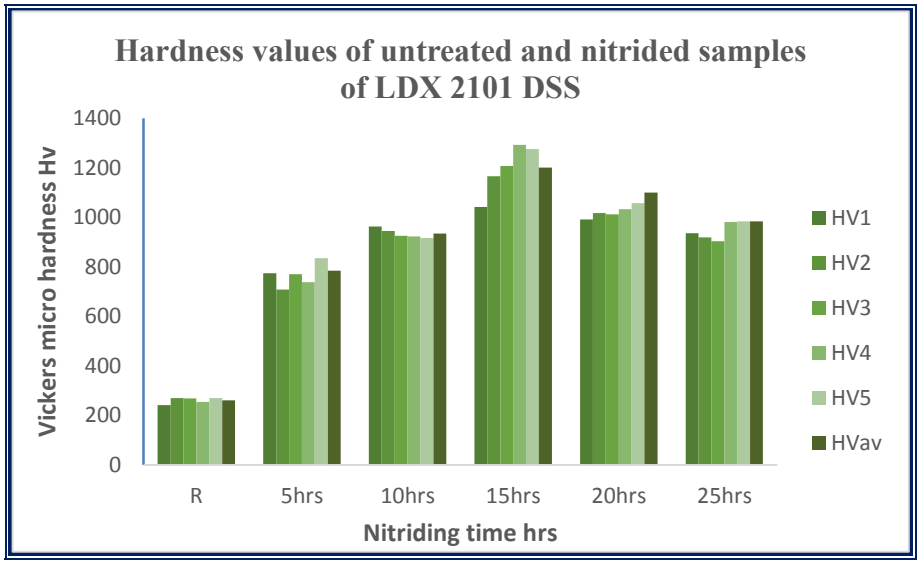

Figure 4.2 Histogram of hardness values for untreated and nitrided samples of LDX 2101 DSS.

4.3.2 Field Emission Scanning Electron Microscopy

Figure 4.3 (a,b,c,d,e) shows the SEM micrographs of nitrided layer at different times. It can be observed that the microstructure is densely packed The main phase of the nitrided layer is the expanded austenite. When the nitriding time extends up to 16 hrs, some pre-existing ferrite in expanded austenite is decomposed and ε-nitride precipitated subsequently. When the treatment time went up to more time, large amount of ε-nitride and CrN precipitates are observed in the pre-existing ferritic region in the expanded austenite. Furthermore, many nitrides precipitate from the pre-austenite region [157].

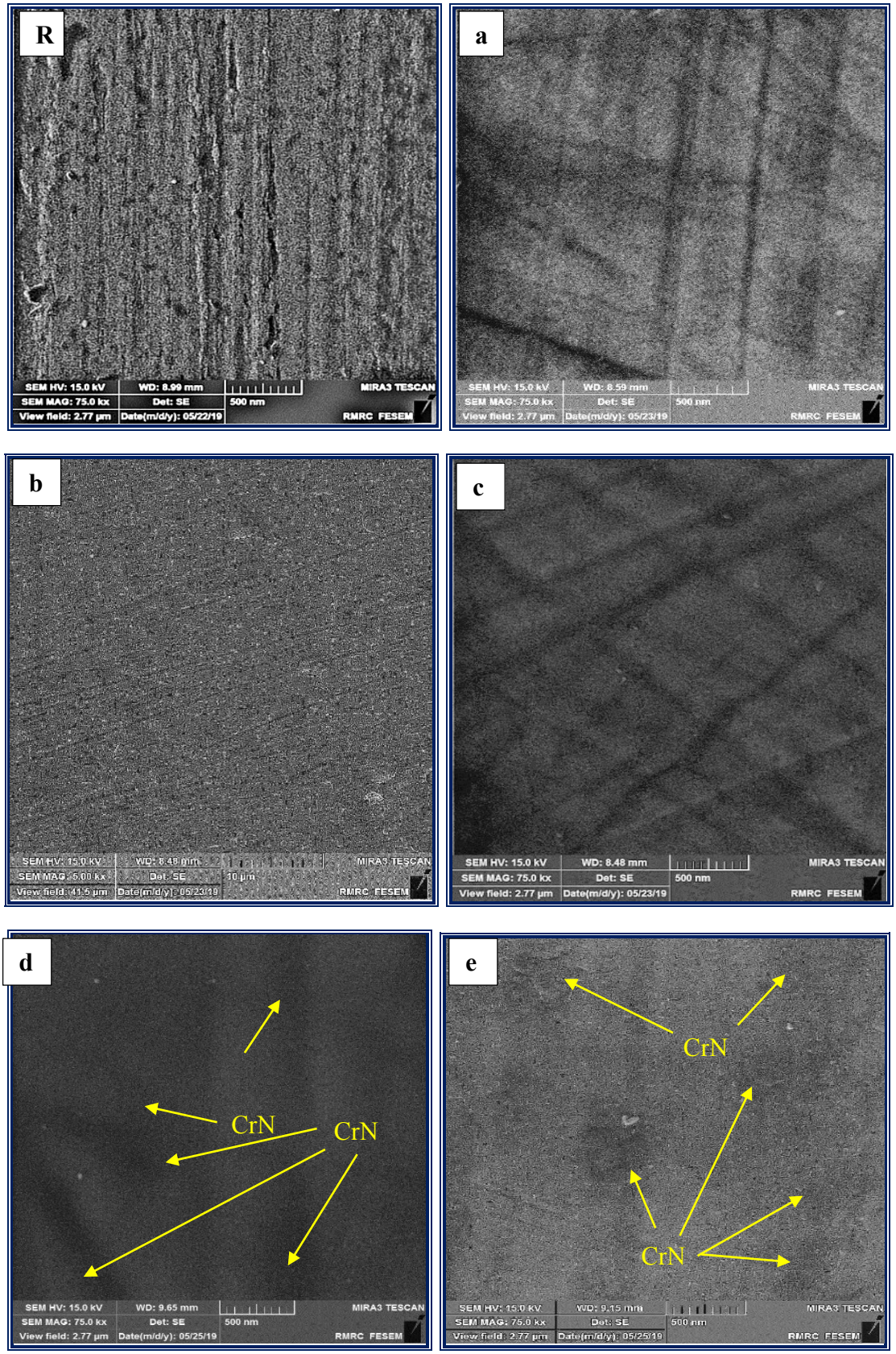

Figure 4.3 SEM micrographs of nitried samples of LDX 2101 DSS alloy at: (R) uncoated (a) 5 (b) 10 (c) 15 (d) 20 (e) 25 hrs.

At 5-hrs deposition time (Figure 4.3), it can be seen that the distribution of particles is better than uncoated morphology, while Figure

4.3 (b) that the nitriding time is 10 hrs shows more close packed microstructures, homogeneity surface, crack- free and uniform coating were achieved. On the other hand, after (15, 20, 25) hrs as shown in Figure 4.3 (c,d,e), it can be observed that there are coarse particles with non-uniform distribution. These observations are due to the coalescence of large amount of Ɛ-nitride and CrN precipitates [157].

Figure (4.4) (a,b,c,d,e) illustrates the cross-sectional topography of the nitriding coating at (5, 10, 15, 20, 25) hrs. It can be seen that the coated layer has a regular thin film structure of (97.32, 176.28, 248.70, 200.06, 113.67) nm in thickness, with higher compact, homogeneity, and complete adhesion between the coating and the substrate. Figure (4.4) shows the mapping of elements that are present in nitrided samples. With the increase in nitriding time, its thickness increases significantly. When the nitriding time is over 15 hrs, the thickness decreases slowly. Obviously, with the increase of nitriding time, the growth rate of the compound layer gradually slows down. The reason is that due to the extension of nitriding time, the nitrides formed on the surface of LDX 2101 increase, which results in the diffusion resistance of nitrogen increasing and the formation ability of nitrides reducing [159,194]. In Plasma nitriding, excessively long treatments lead to thinner coatings because of the plasma formation and continuous sputtering on the metal surface [160].

When nitriding time is 20 and 25 hrs, there is some micro cracks appears on the surface layer of the treated samples, and the longer nitriding time is, the more cracks are.

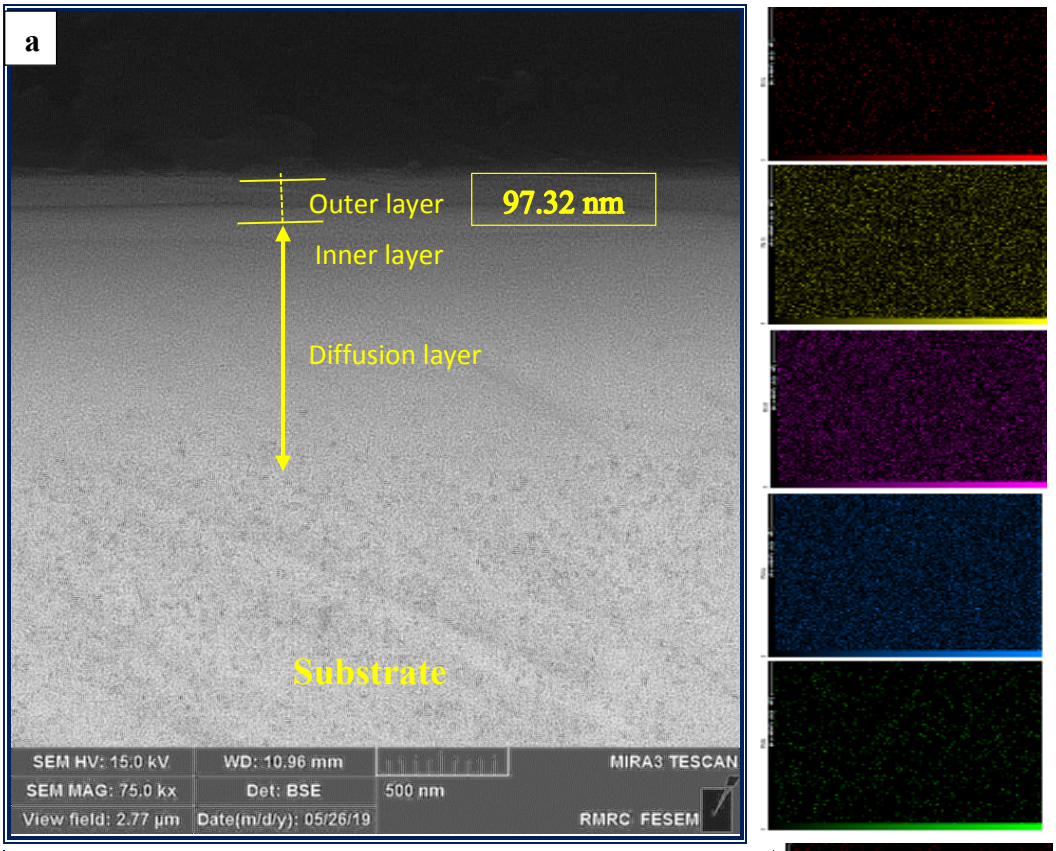
a
Outer layer
97.32 nm
Inner layer
Diffusion layer
Substrate
SEM HV: 15.0 kV
WD: 10.96 mm
MIRA3 TESCAN
SEM MAG: 75.0 kx
Det: BSE
500 nm
View field: 2.77 µm
Date(m/d/y): 05/26/19
RMRC FESEM

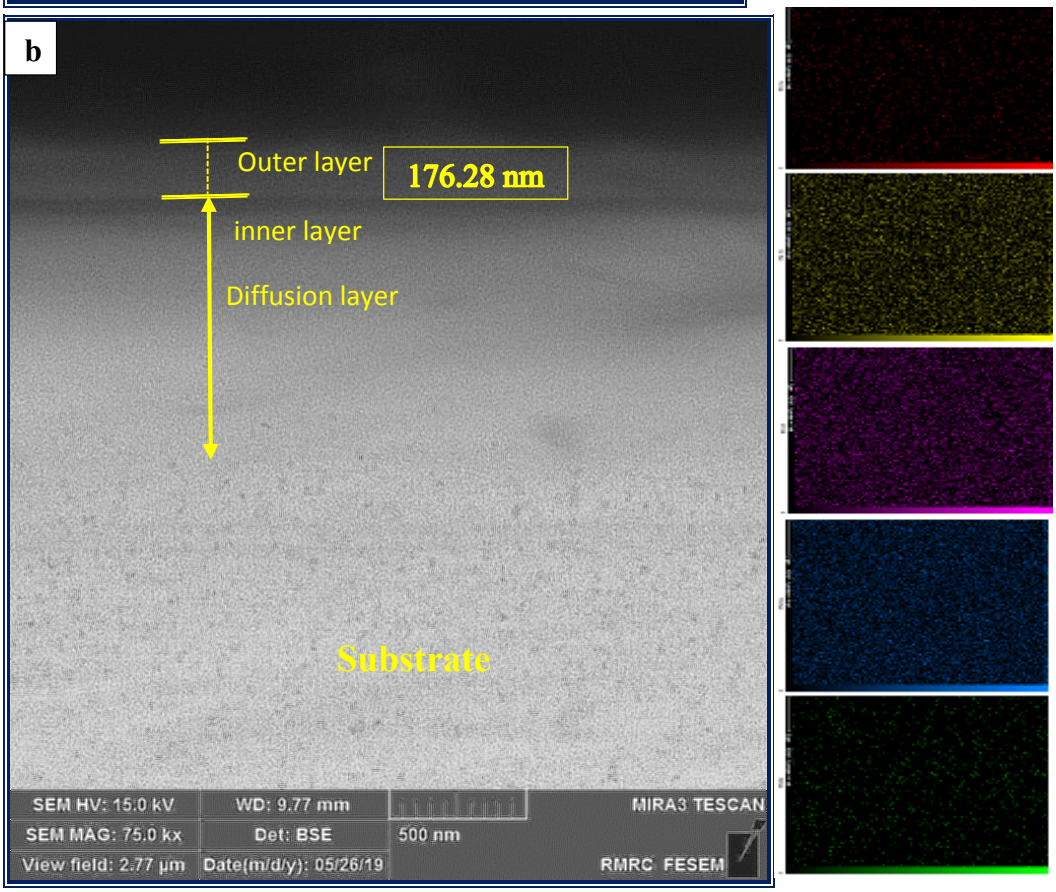
b
Outer layer
176.28 nm
inner layer
Diffusion layer
Substrate
SEM HV: 15.0 kV
WD: 9.77 mm
MIRA3 TESCAN
SEM MAG: 75.0 kx
Det: BSE
500 nm
View field: 2.77 µm
Date(m/d/y): 05/26/19
RMRC FESEM

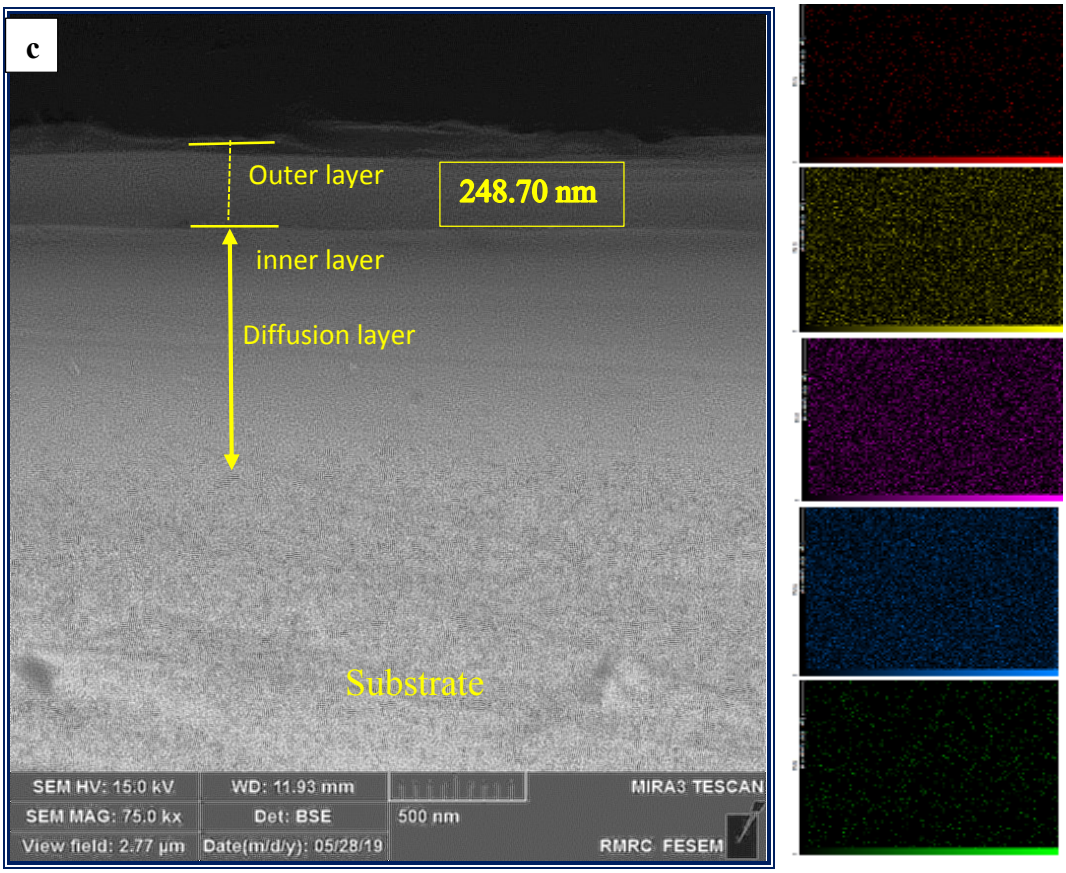
c
Outer layer
248.70 nm
inner layer
Diffusion layer
Substrate
SEM HV: 15.0 kV
WD: 11.93 mm
MIRA3 TESCAN
SEM MAG: 75.0 kx
Det: BSE
500 nm
View field: 2.77 µm
Date(m/d/y): 05/28/19
RMRC FESEM

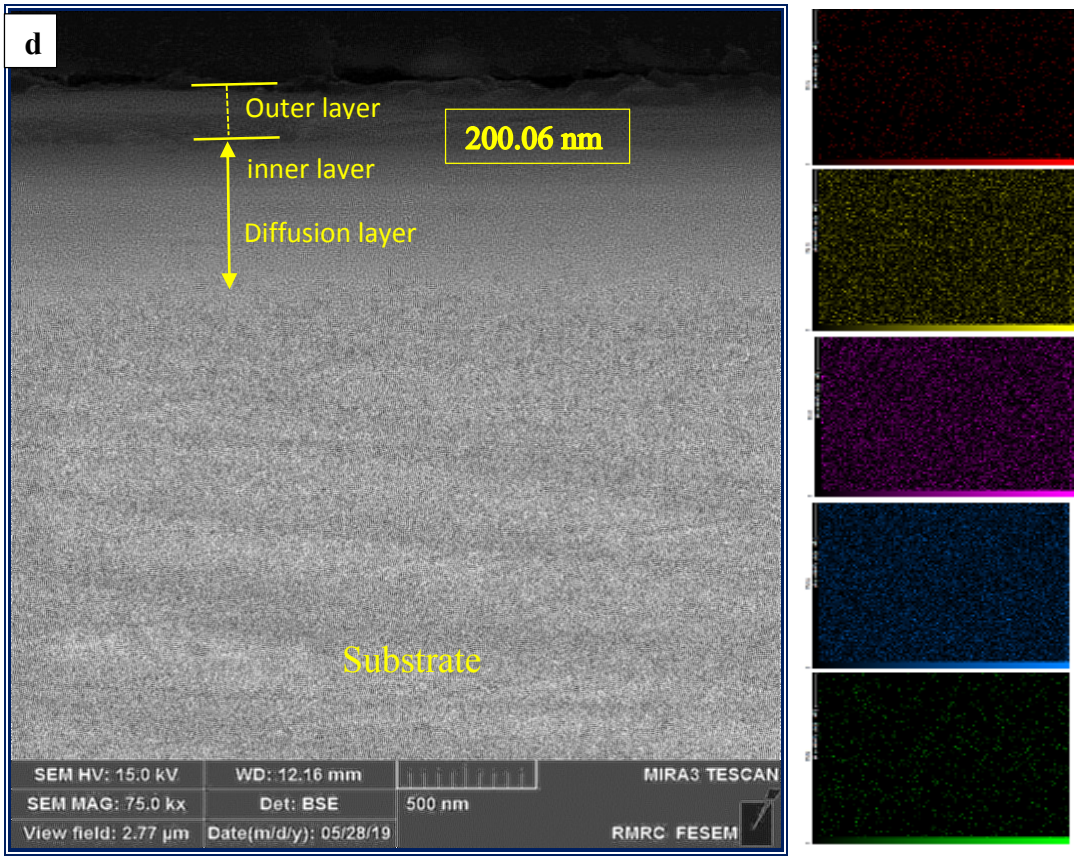
d
Outer layer
200.06 nm
inner layer
Diffusion layer
Substrate
SEM HV: 15.0 kV
WD: 12.16 mm
MIRA3 TESCAN
SEM MAG: 75.0 kx
Det: BSE
500 nm
View field: 2.77 µm
Date(m/d/y): 05/28/19
RMRC FESEM

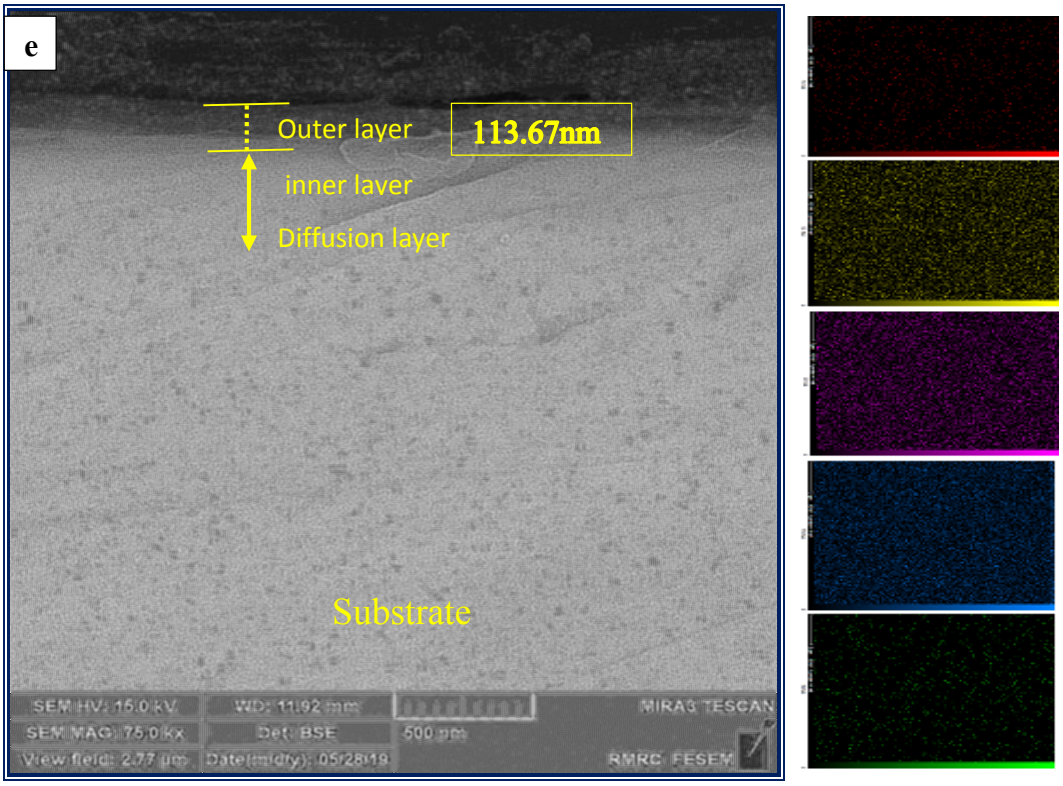

Figure 4.4 Cross-sectional SEM micrographs and EDS elemental mapping of N, O, Cr, Fe and Ni of nitrided samples at (a) 5 (b) 10 (c) 15 (d) 20 (e) 25 hrs.

4.3.3 Energy Dispersive Spectroscopy

The elemental composition of nitrided layer formed on the LDX 2101 DSS alloys for different times parameters are shown in Figure (4.5).

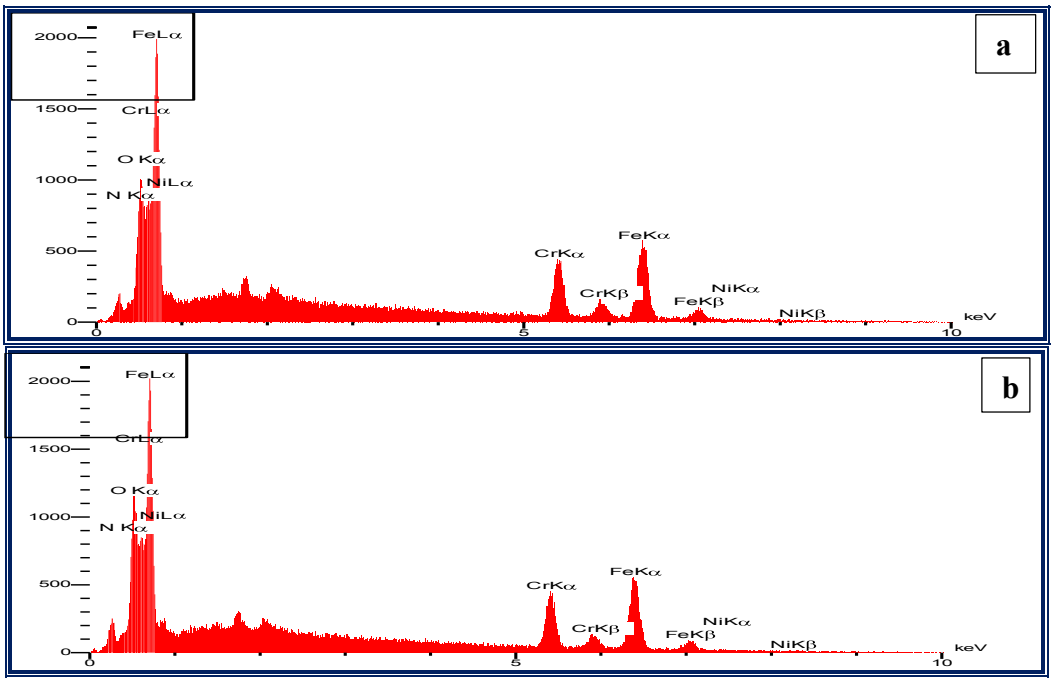

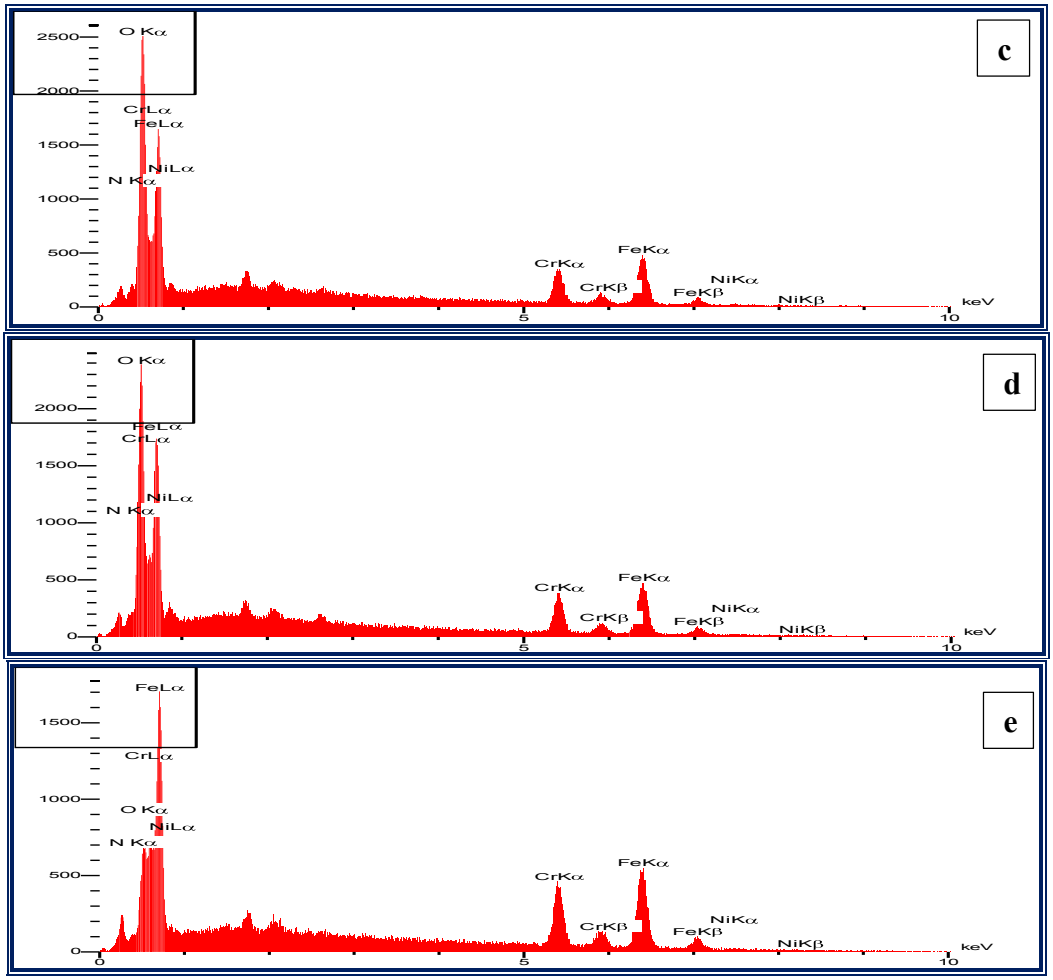

Figure 4.5 EDS analysis for nitrided samples at: (a) 5 (b) 10 (c) 15 (d) 20 (e) 25 hrs.

It can be observed that the main elements of Fe, Cr, O, N and Ni are presented in the coatings. The existence of these elements confirms the formation of nitrided coating on the LDX 2101 DSS alloy. Moreover, there is no other peaks different from nitride and this assure the coating purity.

4.3.4 X-Ray Diffraction Analysis

The XRD results, (Figure 4.6), reveals crystalline α and γ phases in the reference (untreated) LDX sample, these phases are identified according to the JCPDS card numbers where the diffraction pattern of the ferrite phase match with the (JCPDS Card No. 06-0694) peaks and the austenite phase match with the (JCPDS Card No. 33- 0397). After nitriding, the expanded austenite (γN - S-phase) and nitride (γ′-Fe_4N and Ɛ-$Fe_{2-3}N$) phases are identified in all the surfaces. Likewise, with increasing treatment time, the

α phase of nitrided DSS is converted into γN, Ɛ-$Fe_{2-3}N$, and Ɛ + CrN (Figure 4.6 – d and e), the γN being the main phase on the surfaces in accordance with literature [73,156,161].

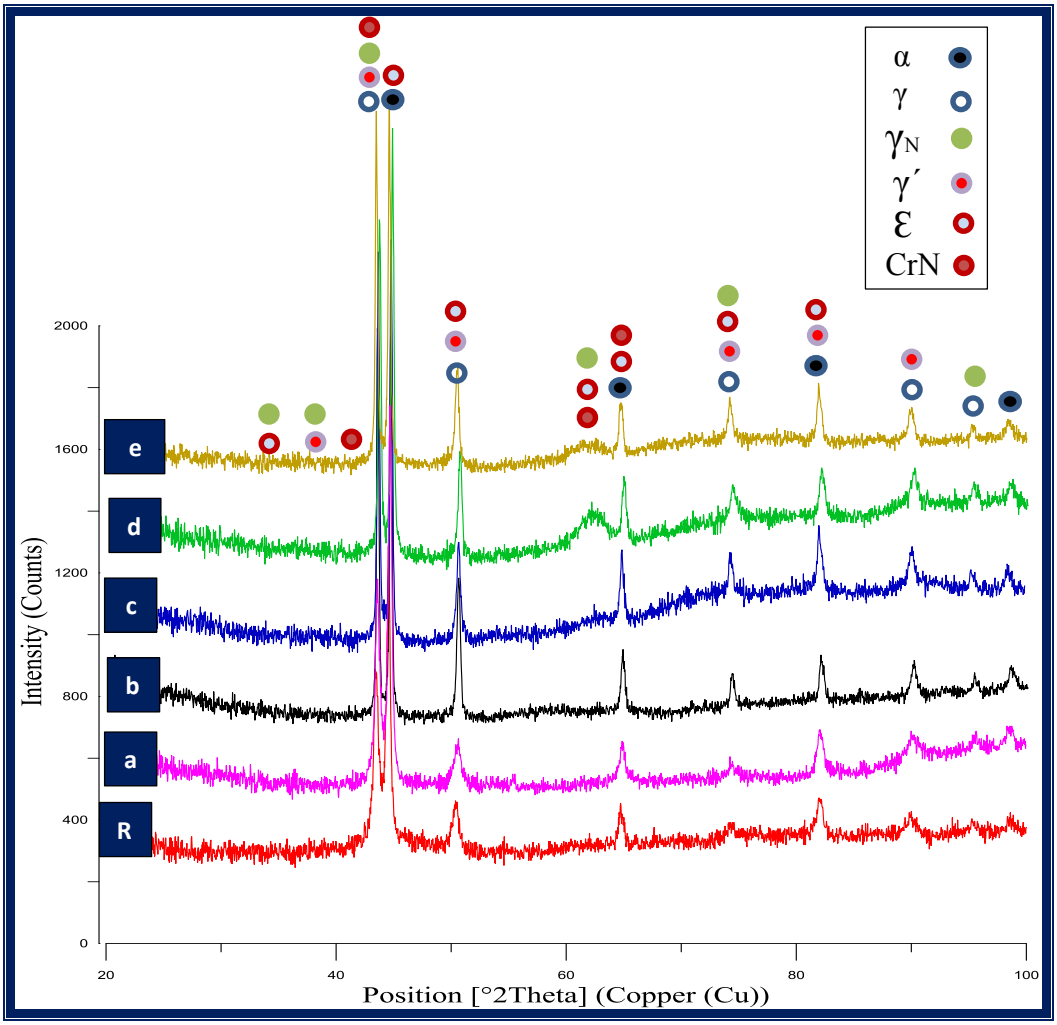

Figure 4.6 XRD patterns of plasma nitrided LDX 2101samples at: (R) un treated (a) 5 (b) 10 (c) 15 (d) 20 (e) 25 hrs.

4.3.5 Atomic Force Microscopy Analysis

The average surface roughness (Ra) of the uncoated LDX 2101 DSS sample was equal to (2.55) µm. The roughness was required to develop the necessary mechanical bonding to improve the adhesion between the coating and base alloy for biomedical applications. The AFM analysis is done for the nitrided alloys and the topography of the nitrided samples with 3D performance images were shown in Figure (4.7). The topography shows some spherical packed particles in a dense and homogeneous layer of the

coated samples, as well as the surface roughness were (2.66, 3.02, 4.38, 6.78 and 8.25) nm respectively. The illustrated topographies indicate that the surface of nitride samples is covered by semispherical nitride particles. The height and width of these nitride particles increased with the increase of the treatment time. This is an important role in the bone replacement field, where it is strongly related to the bonding between the implant surface and host bone, hence it accelerated the implant fixation to the human body [160,162]. The different particles distributions for the mentioned samples are shown in Figure (4.7). It appears that the granularity accumulations for the coating layers with average diameters of (455.28, 844.28, 1032.94, 1374.40, 1436.02) nm respectively in these conditions increase with increasing nitriding time. which is attributed to the growth of particles [163].

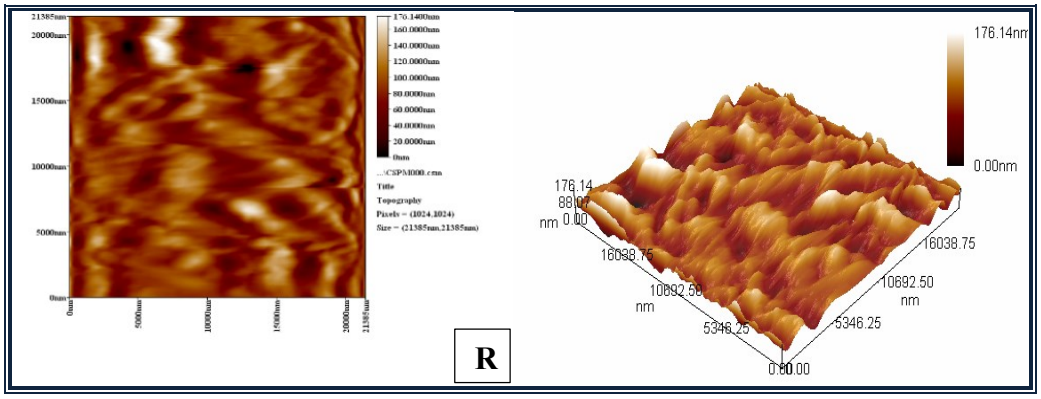

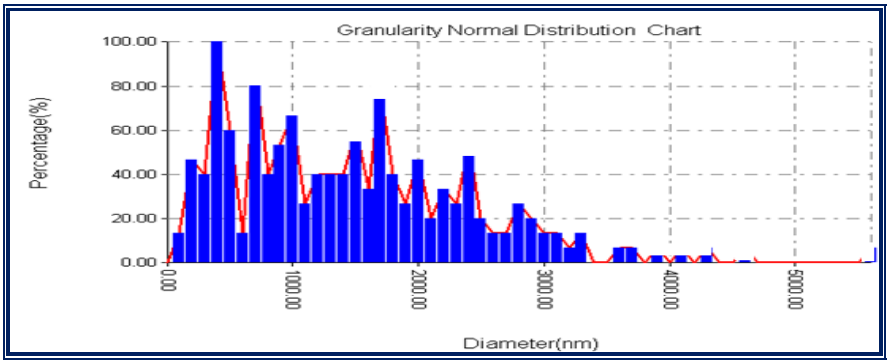

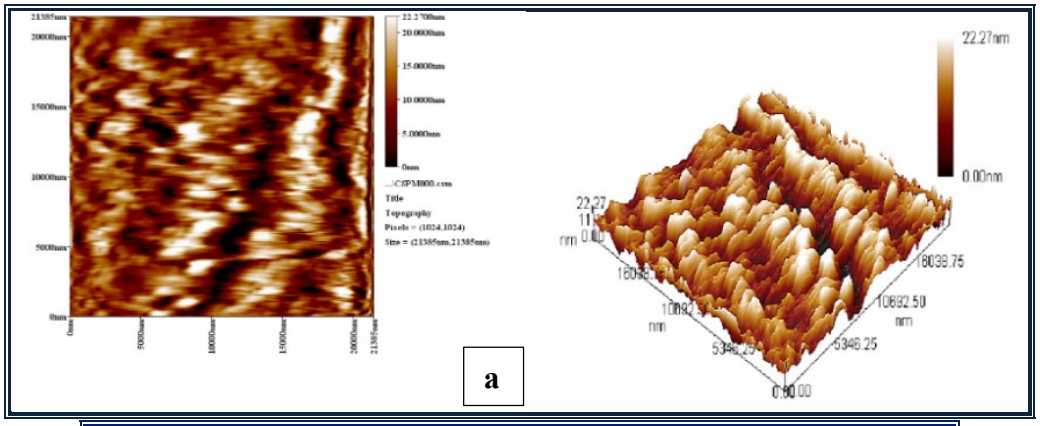
22.27nm
0.00nm
22.27
11
nm 0.00
18038.75
10692.50
nm
5346.25
0.00
a

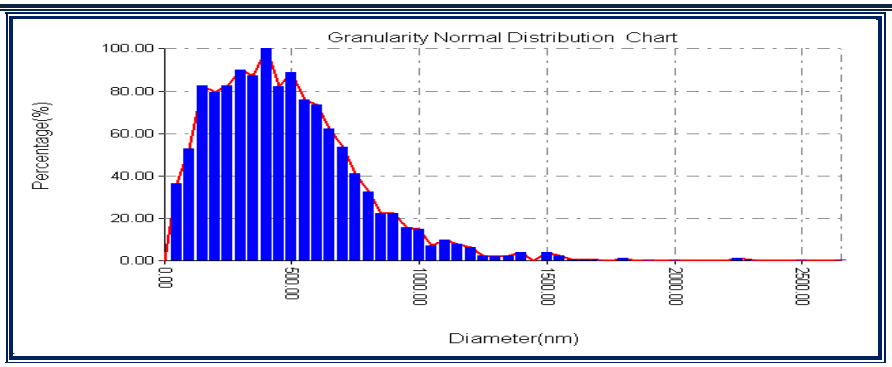
Granularity Normal Distribution Chart
Percentage(%)
100.00
80.00
60.00
40.00
20.00
0.00
0.00
500.00
1000.00
1500.00
2000.00
2500.00
Diameter(nm)

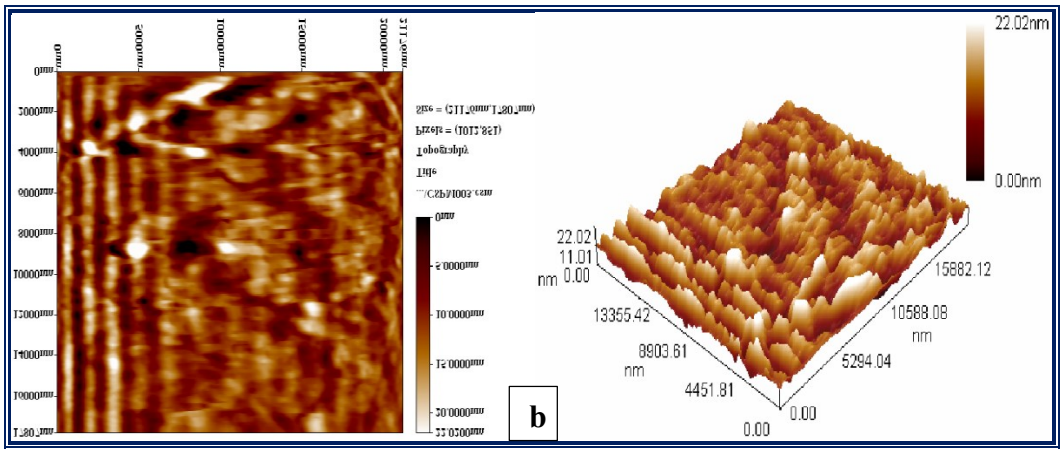
22.02nm
0.00nm
22.02
11.01
nm 0.00
15882.12
13355.42
10588.08
nm
8903.61
nm
5294.04
4451.81
0.00
0.00
b

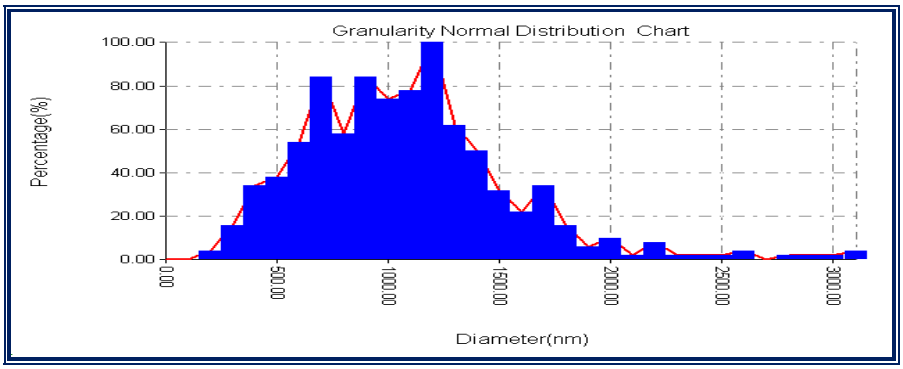
Granularity Normal Distribution Chart
Percentage(%)
100.00
80.00
60.00
40.00
20.00
0.00
0.00
500.00
1000.00
1500.00
2000.00
2500.00
3000.00
Diameter(nm)

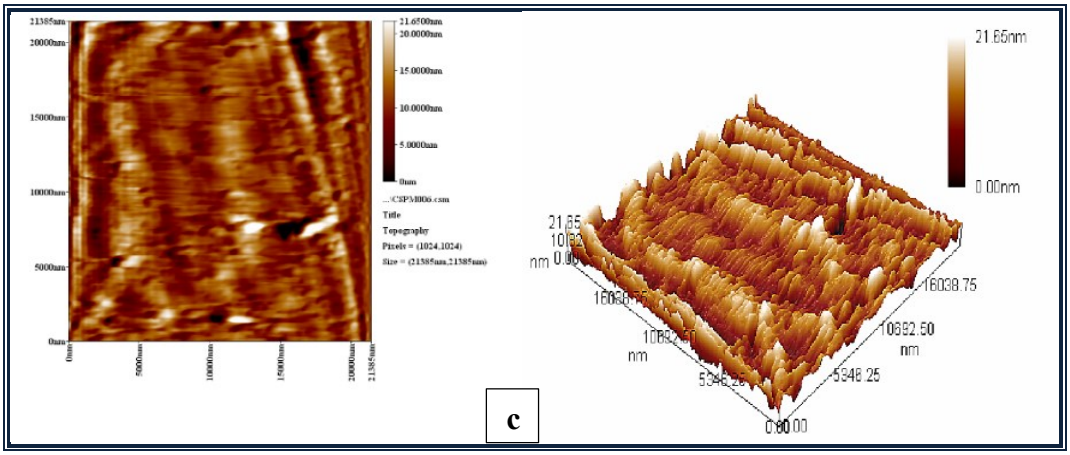
21.65nm
0.00nm
c

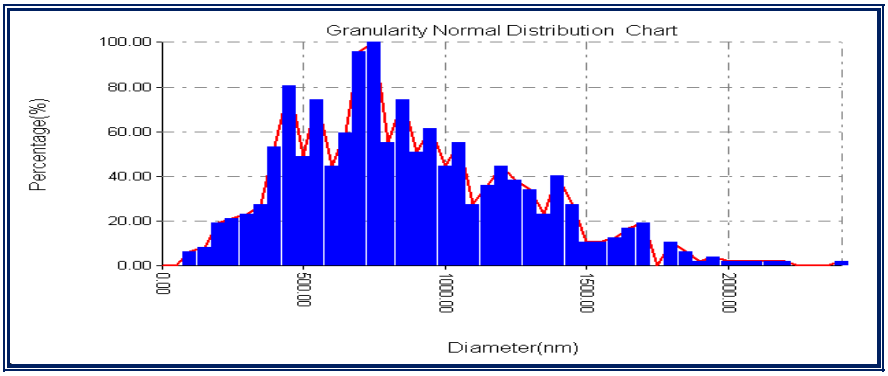
Granularity Normal Distribution Chart
Percentage(%)
Diameter(nm)

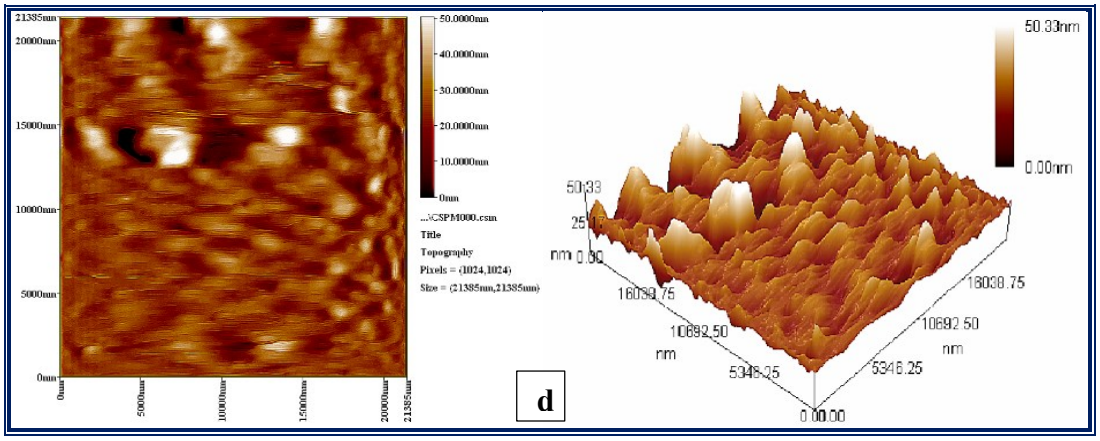
50.33nm
0.00nm
d

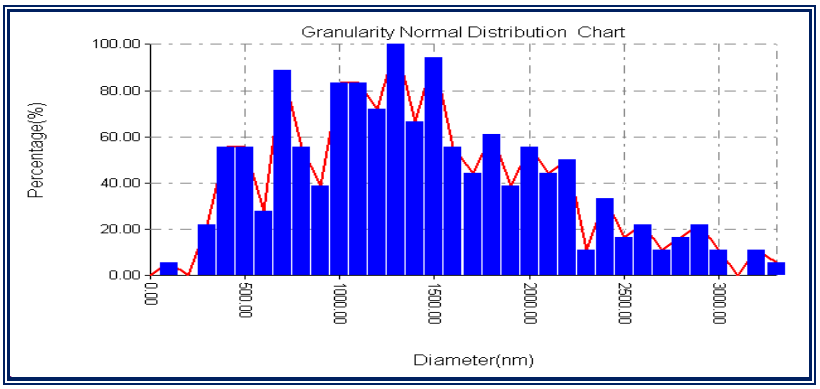
Granularity Normal Distribution Chart
Percentage(%)
Diameter(nm)

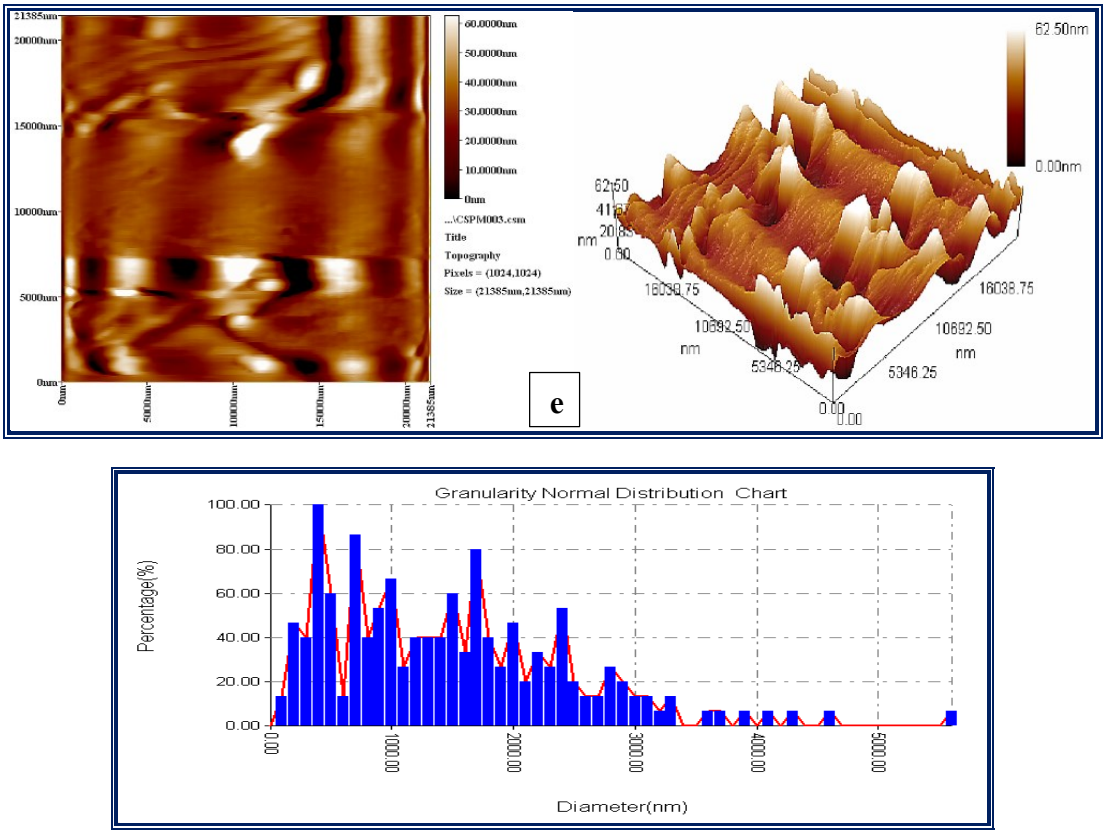

Figure 4.7 The topography of the nitrided samples with 3D performance images and granularity accumulation chart for particles at: (R) un treated (a) 5 (b) 10 (c) 15 (d) 20 (e) 25 hrs.

4.3.6 Antibacterial Test

The effect of the antibacterial nitrided LDX 2101 DSS alloys was examined against E. coli culture as shown in (Figure 4.8). The formation of a clear region around the disc is referred to as the bacterial inhibition zone. After 24 hours of incubation, both cases exhibited a good antibacterial effect against E. coli [164], and then the nitride particles exhibited a strong antibacterial effect. Therefore, the presence of N2 nano particles was effective in preventing bacterial adhesion on the surface and, in turn, preventing bacteria growth, which would improve the antibacterial activity, and this activity would increase with increased nitriding time. Bacterial tests demonstrated the nitrided layer had excellent anti-bacterial properties [67,150].

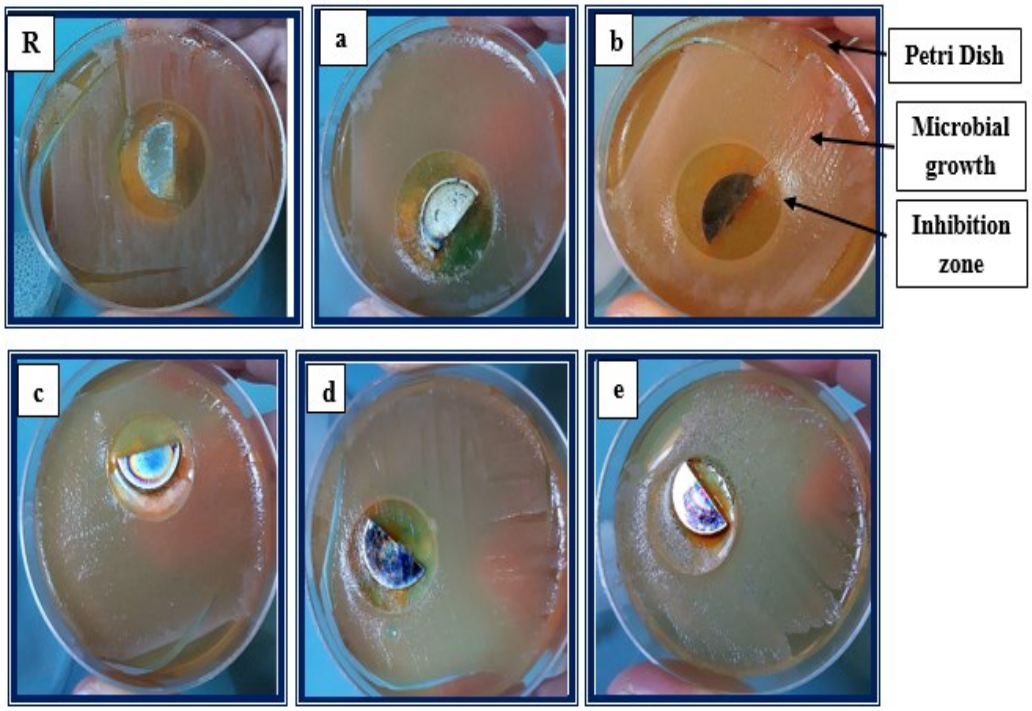

Figure 4.8 Optical photographs of antibacterial activity of E.coli performed for nitrided samples at: (R) un treatment (a) 5 (b) 10 (c) 15 (d) 20 (e) 25 hrs.

4.3.7 Adhesion Test

Figure (4.9) shows the optical microscope (OM) images of Rockwell C indentation on the nitrided samples. Deep and long cracks were observed around the indentation point in the nitrided samples. Furthermore, no delamination was observed around the Rockwell C indentation effect. These results show that the adhesion strength quality of these samples is related to HF1 and HF2 and these failures represent HF2-HF3 type of the adhesion strength quality. The adhesion of all treated sample is sufficient [165,166]. The adhesion strength of the surface layer substrate declines, and the longer the nitriding time is, the more obvious the decline is. This may be attributed to the fact that the brittle phase of CrN (as shown in XRD) increases and coarsens with nitriding time increasing (as observed in AFM, Figure 4.7), which causes a decrease in the toughness of the surface layer. Besides, the structural differences between the phases increase the residual stress in the surface layer [159].

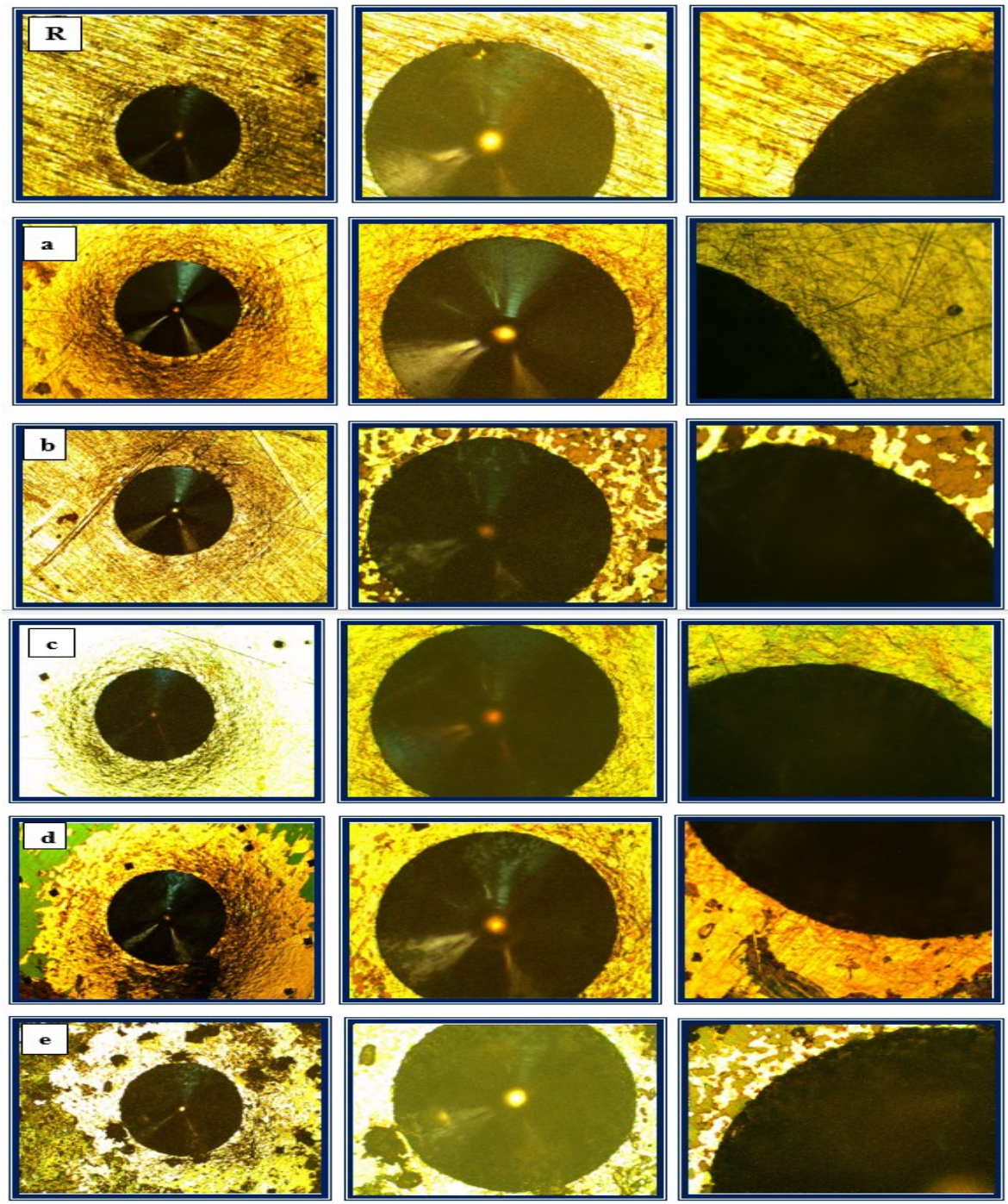

Figure 4.9 Optical photographs of Rockwell type - C effect an indentation for plasma nitrided samples at: (R)un treatment (a) 5 (b) 10 (c) 15 (d) 20 (e) 25 hrs.

4.3.8 Corrosion Behavior

Investigation of corrosion behavior of coating is obtained by potentiodynamic and cyclic polarization tests. At first, the sample is immersed in Ringer's physiological solution for 30 min and the open circuit potential (OCP) has been recorded after this period, where a steady

state potential is attained. The corrosion behavior has been studied for nitriding time.

4.3.8.1 Potentiodynamic Polarization

Figure (4.10) shows the potentiodynamic polarization curves for untreated LDX 2101 DSS alloy and nitrided samples in the Ringer's solution at 37 ±1 °C for different treatment time. The corrosion current densities (i_{corr}) and corrosion potentials (E_{corr}) are derived from the potentiodynamic curves by employing Tafel extrapolation (Table 4.1). In addition, the corrosion rates (CR) are also included in this Table and it is calculated according to the equation (3.2).

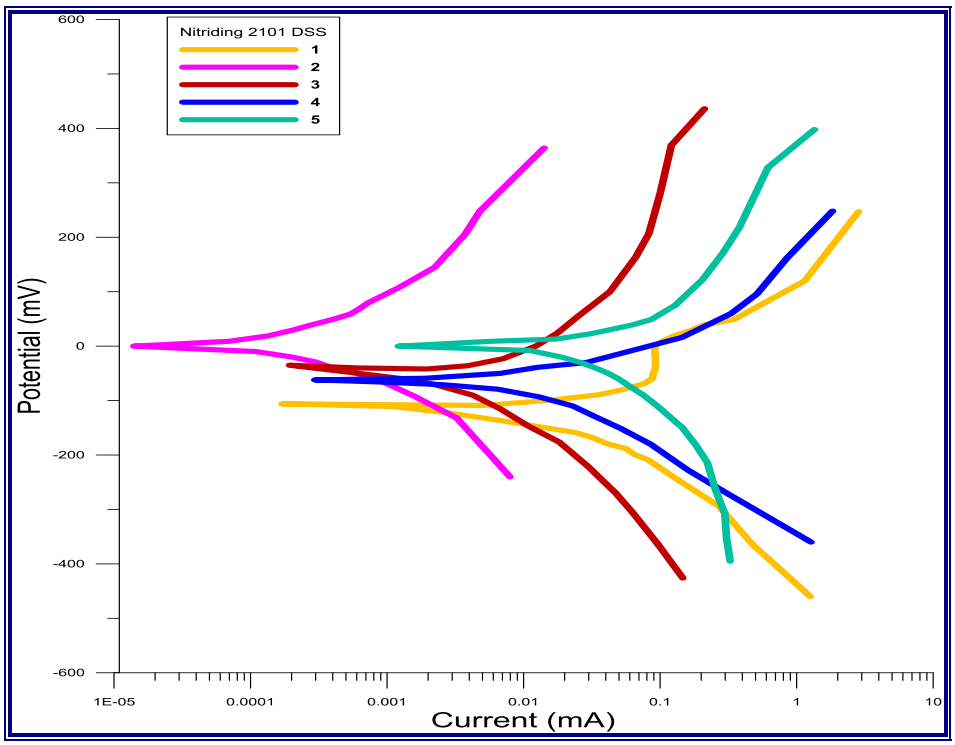

Figure 4.10 Potentiodynamic polarization curves of untreated LDX 2101 DSS and nitrided samples at different times in Ringer's solution at 37 ±1 °C.

It can be realized from the results obtained in Table 4.1, the untreated alloy has high corrosion current density (i_{corr} = 2.75 µA/cm^2) and thus corrosion resistance happens because of the occurrence of metal ions dissolution on the surface of the uncoated substrate. After nitriding, it can be observed that the corrosion current density of some samples decreases, this means that the nitriding provides a protective layer on the alloy surface that would

reduce the corrosion rate. The nitriding time (5 hrs) treated samples showed better corrosion resistance than the untreated samples. When nitriding at 10 hrs, a lowest corrosion current (i_{corr} = 0.118 μA/cm^2) is obtained. It is evident that the sample coated at 10 hrs shows a lowest corrosion rate and high E_{corr} and thus more corrosion resistance than the others. This mean a high nitride protection layer on the 2101 DSS substrate is obtained because of uniform, dense and compact layer structure of this sample, while the nitriding time at 15, 20 and 25 hrs, shows some micro cracks, and the presence of CrN in structure (see Figure 4.3 – c, d and e), this leads to decrease the corrosion resistance [78,156].

Table 4.1 Electrochemical parameters of the nitrided samples for LDX 2101 DSS at different times.

Sample no.	Condition	i_{corr} (μA/cm^2)	E_{corr} (mV)	CR(mpy)
R	untreated	2.75	-34.2	1.329
1	5 hrs	1.56	-37.1	0.754
2	10 hrs	0.118	13.2	0.057
3	15 hrs	1.87	-84.8	0.903
4	20 hrs	2.66	15.3	1.285
5	25 hrs	5.64	-145	2.725

In addition, coating at extension time leads to produce a coarse particles and inhomogeneity in the nitride layer that result in rough and poor deposit quality. On the other hand, nitriding at 25 hrs has the lowest corrosion resistance than the other as a result of the low layer thickness compared with the other samples.

Finally, the corrosion resistance of the diffusion layer increases with the improvement of nitriding time, but after nitriding 10 hrs its uptrend stabilized, It is also evident that the corrosion behavior of time 10 hrs is better than others of a high corrosion potential and lower passive corrosion density [167,147].

Polarization resistance (Rp) measurements were used to determine the protective ability of nitrided layer since the registered Rp values are

contrariwise proportional to the corrosion current (higher polarization resistance means lower corrosion current). The corrosion rate was directly related to the Rp. Rp was calculated by Eq. (3.3).

Table 4.2 Polarization resistance of untreated and nitrided LDX 2101 DSS samples.

Sample no.	Condition	i_{corr} (μA/cm^2)	βa (mV)	βc(mV)	Rp (kΩ.cm^2)
R	Un treated	2.75	80	-52.6	5.017
1	5 hrs	1.56	42.7	-124.9	8.86
2	10 hrs	0.118	69	-50.1	106.94
3	15 hrs	1.87	82.4	-86.9	9.83
4	20 hrs	2.66	92.7	-101.5	7.91
5	25 hrs	5.64	125	-78.3	3.71

According to Table 4.2, untreated LDX 2101 DSS has low polarization resistance (Rp = 5.017 $k\Omega.cm^2$). Nitriding process leads to increase in polarization resistance to (Rp = 106.94 $k\Omega.cm^2$) at 10 hrs which has lowest corrosion current density led to lowest corrosion rate.

4.3.8.2 Cyclic Polarization

In order to investigate the resistance of the samples to the localized corrosion, the cyclic polarization is carried out. Figure (4.11) illustrates the cyclic polarization curves for untreated and nitrided samples at different times. Typically, the reading starts at the open circuit potential and scans upwards until breakdown is attained. Then the direction of scan is inverted after specific amount of localized corrosion is established and the passive film is damaged. The potential at which stable pit formed is called breakdown potential (Eb) or pitting potential (Ep). Consequently, the Ep imply the potential over which the pits initiated and developed. If the Ep is high, the material has high resistance to the pitting corrosion [168]. During the reverse scan, a negative hysteresis can be observed on the curve as that shown schematically in Figure (4.11). The difference between Ep and

Eprot (Δ E) will give an indication to the corrosion resistance of the sample, where the smaller Δ E value means the highest corrosion resistance.

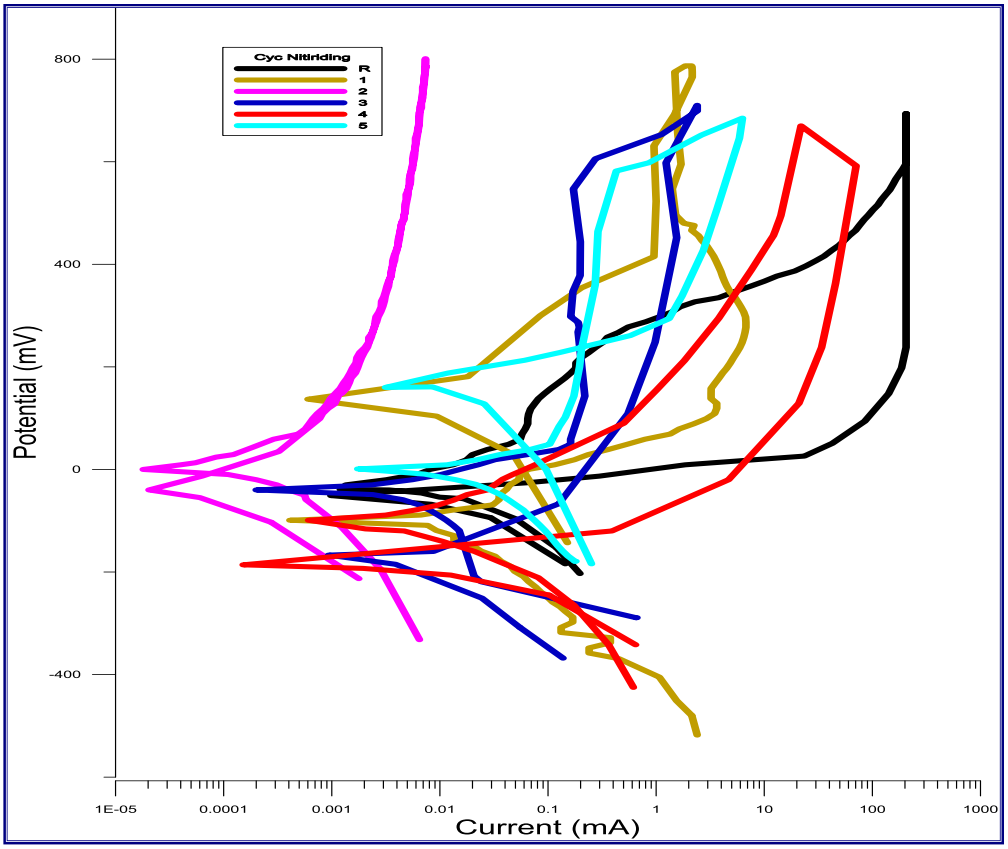

Figure 4.11 Cyclic polarization curves for untreated LDX 2101 DSS and nitrided samples at different times in Ringer's solution at 37 ±1 °C.

It is clear from Figure (4.11) and Table 4.3 that the nitrided sample at 25 hrs has the lowest pitting or break down potential and thus low resistance to the pitting corrosion, this is due to the increasing of coarse particles. However, the nitrided sample at 10 hrs has highest pitting and protection potential with a close hysteresis loop where this polarization behavior tends to be resistant to the localized corrosion. In addition, the lowest value of Δ E is obtained and consequently this sample would have the more resistance to pitting corrosion. Addition of nitrogen increases resistance to pitting corrosion of stainless steels by dissolution of nitrogen at the pit site and subsequent formation of ammonium ions NH_4^+ and NO_3^- in the metal

interface which increases pH and thus slows down pit growth kinetics [105]. This means that this sample has appropriately hindered the pit initiation and propagation. Therefore, based on the results from the potentiodynamic and cyclic polarization curves, it is supposing that the nitrided layer at 10 hrs has a strong ability to act as barrier to prevent the localized corrosion attack of many aggressive ions appeared in Ringer's solution during the corrosion test. Moreover, the nitrided layer has the ability to exhibit efficacious chemical barriers against metal ions release from the metallic implants.

Table 4.3 Values of pitting potential for untreated and nitrided samples at different times from cyclic polarization.

Sample no.	Condition	Ep (mV)
R	untreated	694
1	5 hrs	787
2	10 hrs	801
3	15 hrs	710
4	20 hrs	685
5	25 hrs	670

Part II: Tantalum Pentoxide Deposition by Plasma Sputtering Technique

4.3.9 Vickers Micro Hardness Test

The mechanical strength of LDX 2101 DSS alloy is promoted by a ferritic structure (interstitial solid solution, mainly N; substitutional solid solution, mainly Cr, Mo, Ni; grain refining, with mutual action between the phases), while the austenitic structure promises ductility and fracture toughness [169,170]. Figure 4.12 displays histogram of micro hardness values of samples coated with Ta_2O_5 at different times (2,4,6,8 and 10) hrs. It may be noticed from this Figure that when sputtering time increases, this leads to increase the micro hardness of sputtered samples with Ta_2O_5. It is observed that the hardness value of Ta_2O_5 thin film has significantly increased up to

1.7-fold when compared with un sputtered sample. The increase in hardness values are due to the crystallization state of Ta_2O_5 [171].

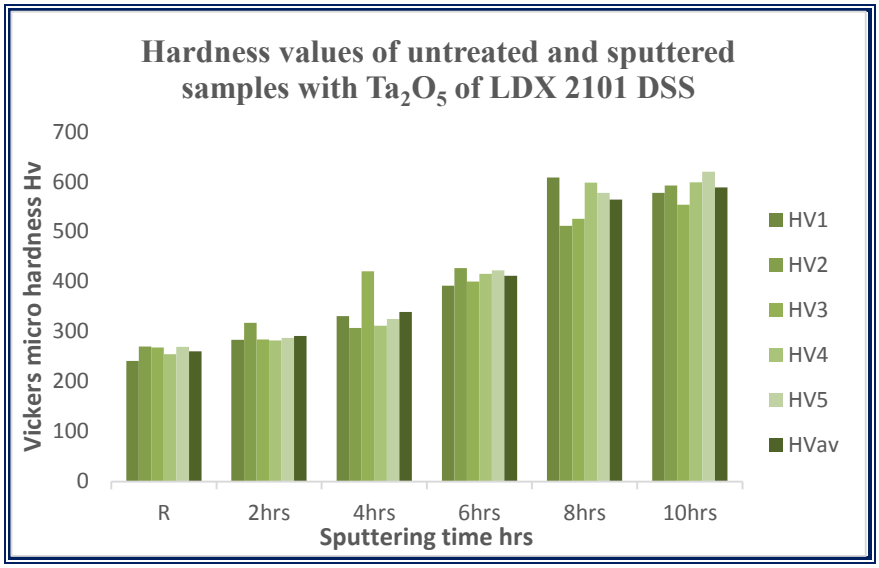

Figure 4.12 Histogram of hardness values for untreated and sputtered samples with Ta_2O_5 of LDX 2101 DSS.

4.3.10 Field Emission Scanning Electron Microscopy

The morphology and topography of un-sputtered and sputtered samples with Ta_2O_5 were observed by SEM in Figure (4.13) (a,b,c,d,e), shows the SEM micrographs of tantalum pentoxide layer coatings at different times. The SEM surface micrograph shows a smoother surface, typically observed in compact coatings grown with amorphous morphologies, suggesting that the addition of (O_2) promotes the densification of the coatings. It can be observed that the microstructure is densely packed and contain a homogeneous particles distribution and leads to the formation of homogeneous coatings. Figure 4.13 (a and b) shows a structure with homogeneous particles distribution within them at (2 and 4) hrs. On the other hand, after 10 hrs as shown in Figure (4.13) (e), it can be observed that there are micro cracks, coarse particles with uniform distribution with some uncovered areas. The use of high time during sputtering leads to a considerable increase in the porosity of deposition and the tendency for micro crack formation. Moreover, coarse particles will deposit and cause

an increase in the roughness and thickness of coating and that will promote the cracking to be more dominant for the thick layer as seen in Figure (4.13 – e). Therefore, it is clear that the coated sample at 8 hrs is the most appropriate one.

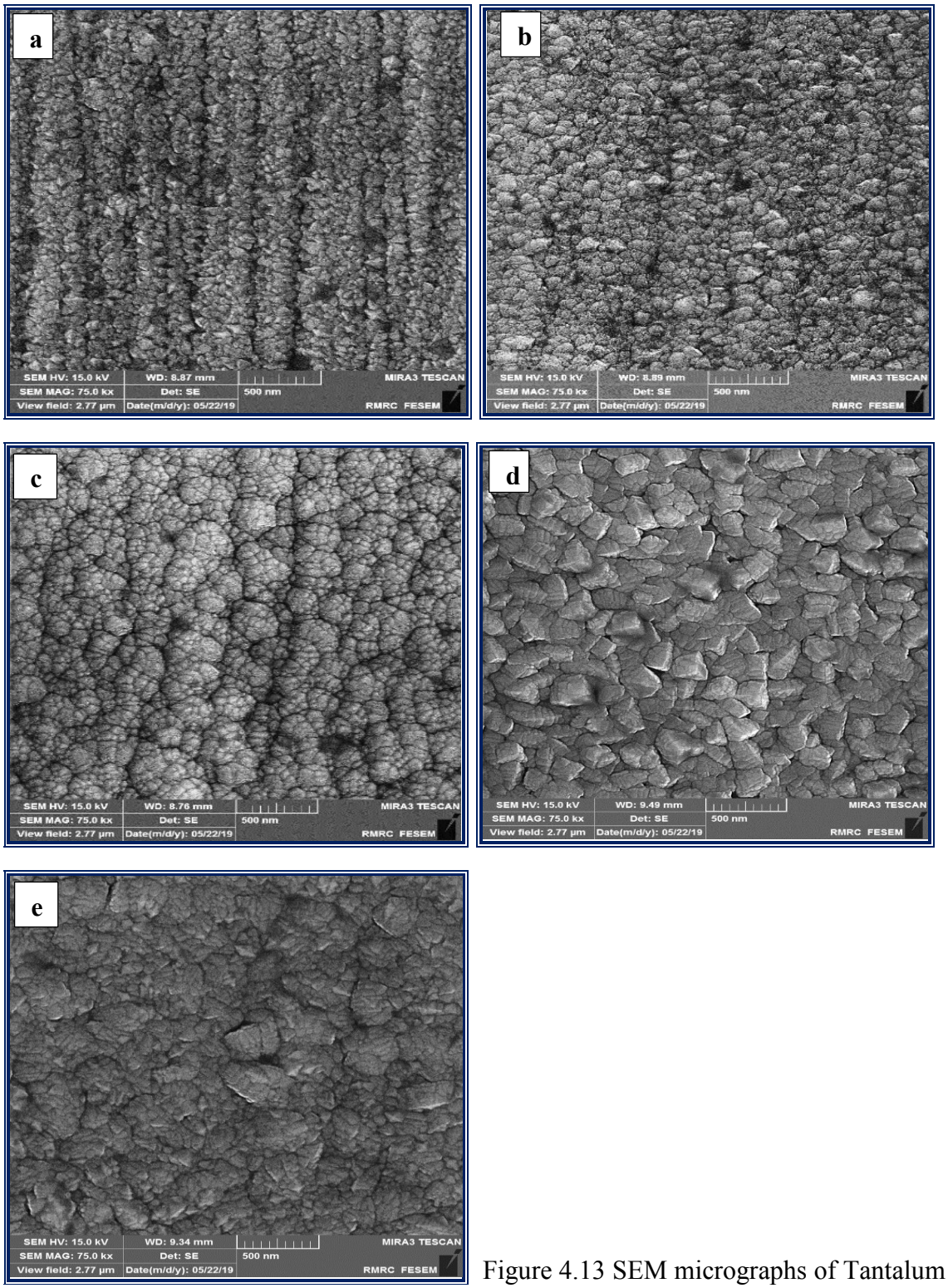

Figure 4.13 SEM micrographs of Tantalum oxide coating on LDX 2101 DSS alloy at: (R) uncoated (a) 2 (b) 4 (c) 6 (d) 8 (e) 10 hrs.

Figure (4.14) (a,b,c,d,e) illustrates the cross-sectional topography of sputtered samples with Ta_2O_5 at (2,4,6,8 and 10) hrs. It can be seen that the sputtered layer has a regular thin film structure of (454.19 nm, 784.92 nm, 867.54 nm, 1.03µm and 2.07µm) respectively in thickness with higher compact, homogeneity and complete adhesion between the coating and the substrate. It can be concluded that with the increase of sputtering time, thickness of coating layer increases significantly [172]. Interfaces can be seen clearly between sputtered layer and substrate. As well as Figure 4.14 shows mapping of elements that present in sputtered Ta_2O_5 samples which are O, Cr, Fe, Ni and Ta that match with EDS analysis (Figure 4.15) [84].

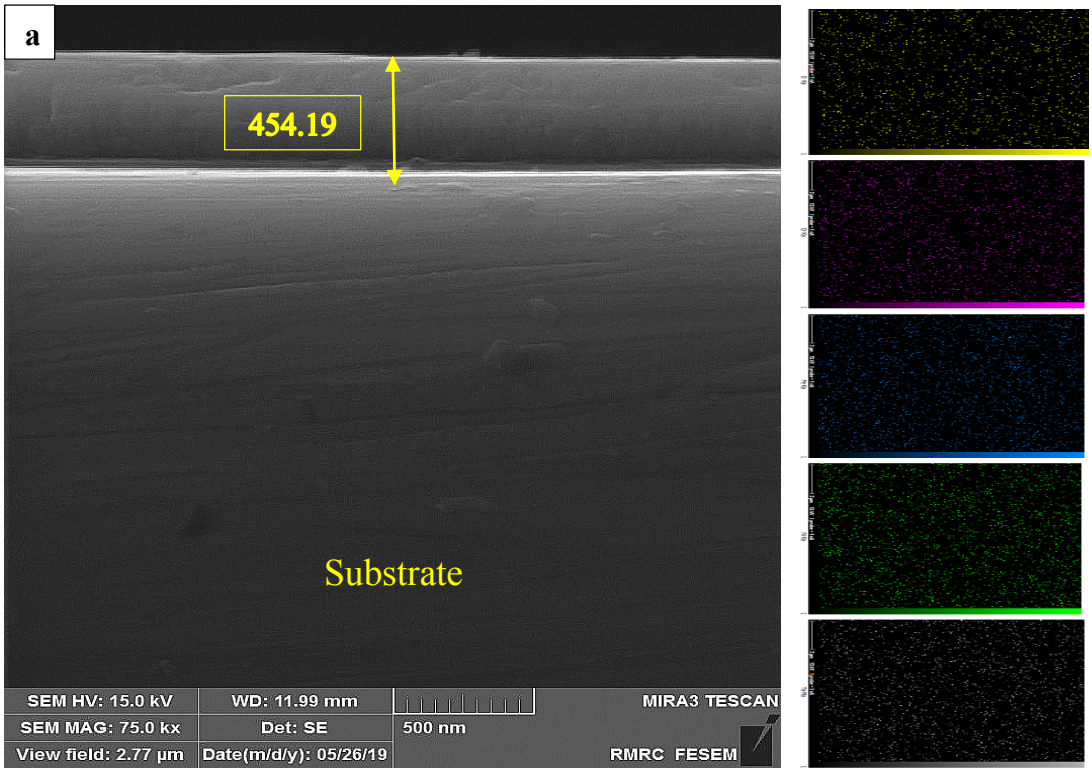

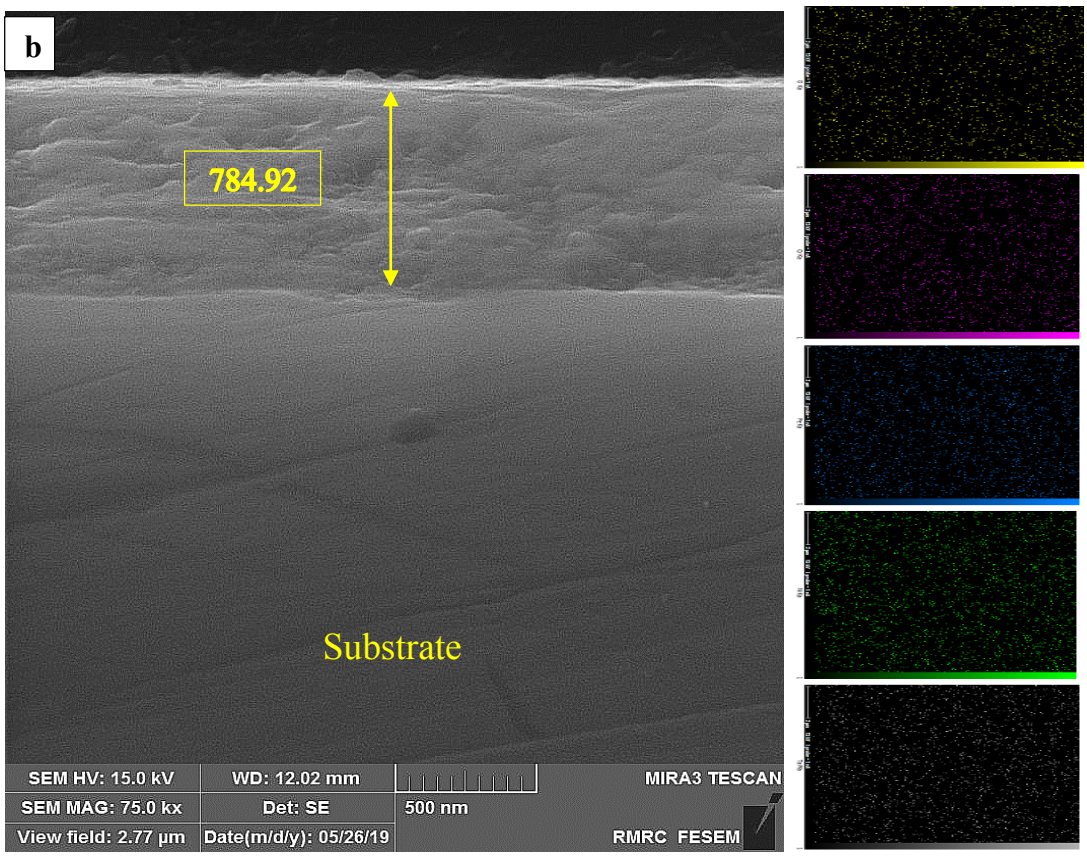
b
784.92
Substrate
SEM HV: 15.0 kV
WD: 12.02 mm
MIRA3 TESCAN
SEM MAG: 75.0 kx
Det: SE
500 nm
View field: 2.77 µm
Date(m/d/y): 05/26/19
RMRC FESEM

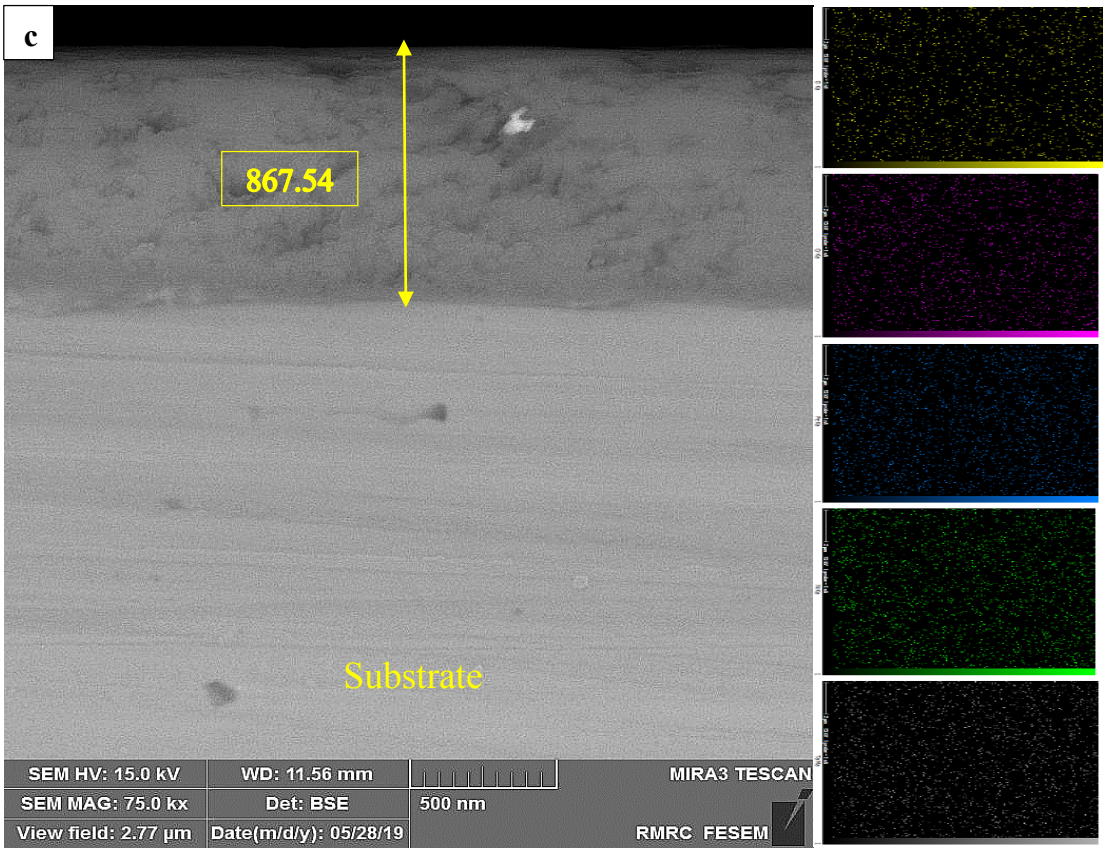
c
867.54
Substrate
SEM HV: 15.0 kV
WD: 11.56 mm
MIRA3 TESCAN
SEM MAG: 75.0 kx
Det: BSE
500 nm
View field: 2.77 µm
Date(m/d/y): 05/28/19
RMRC FESEM

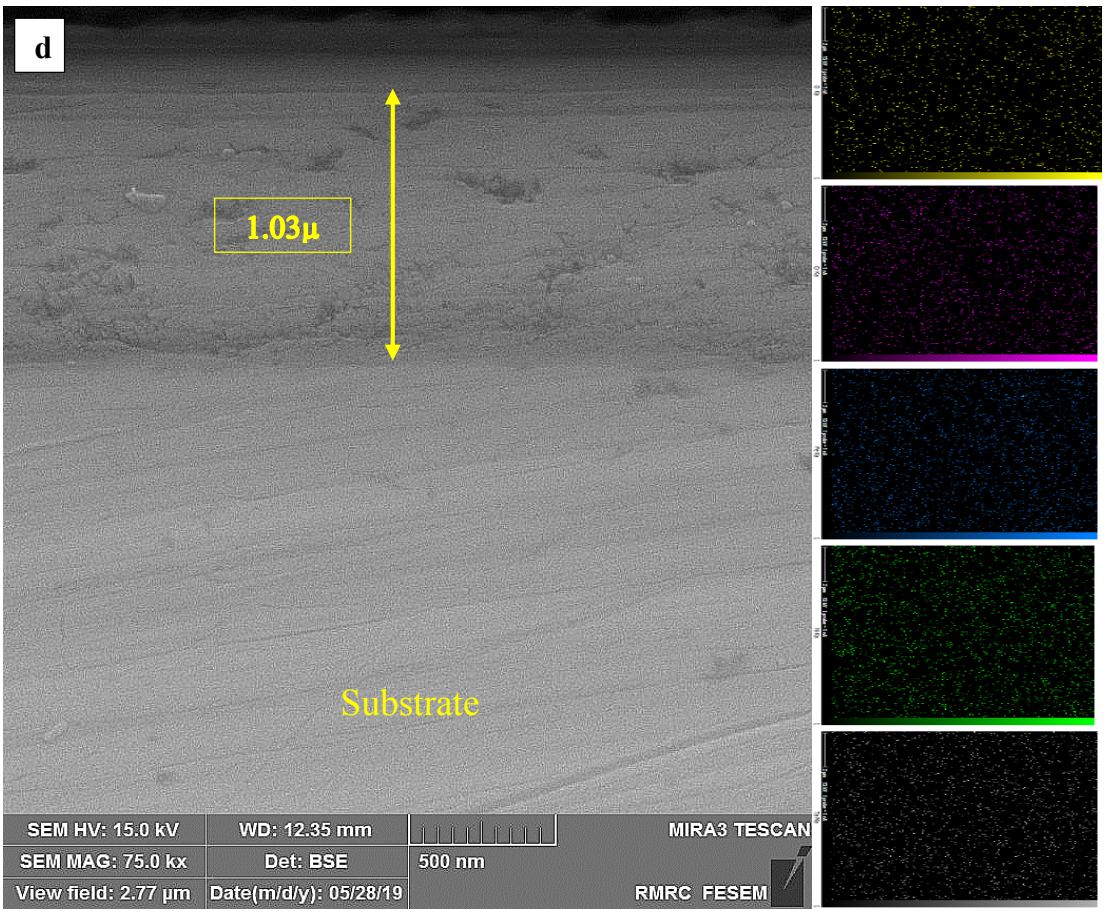

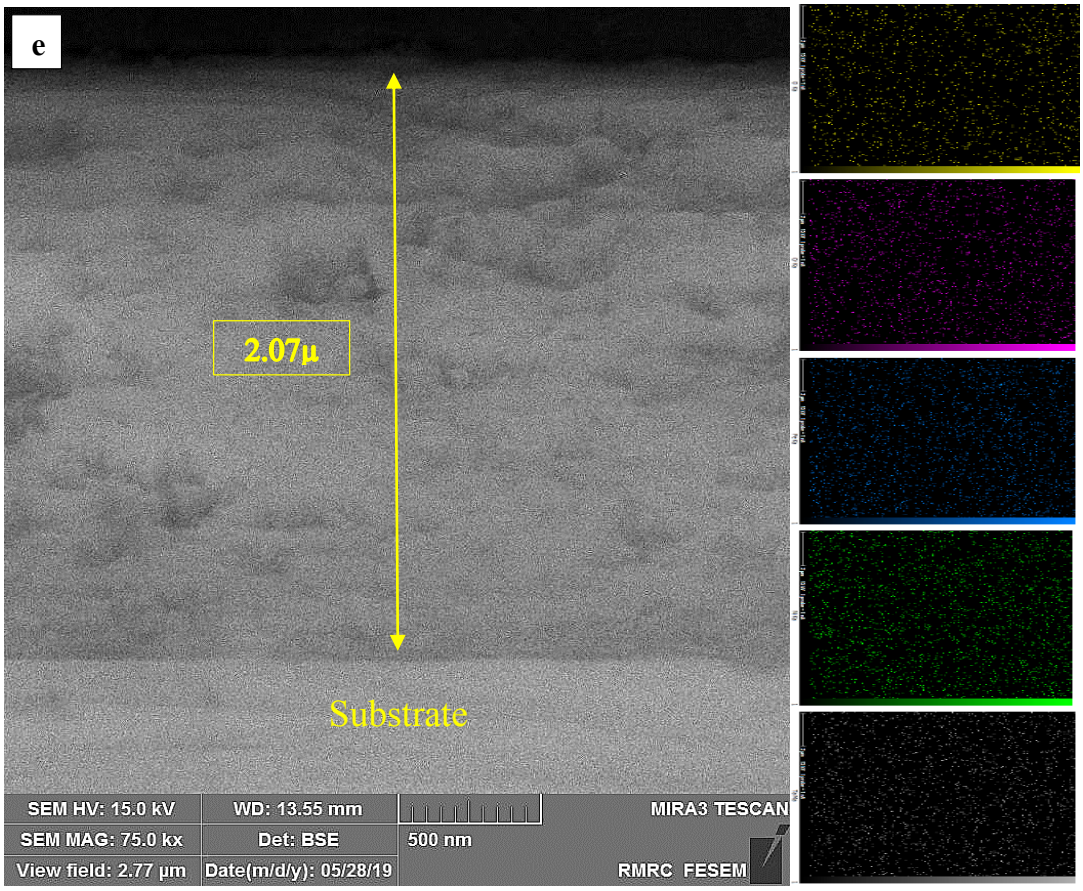

Figure 4.14 Cross-sectional SEM micrographs and EDS mapping of Tantalum oxide coating on LDX 2101 samples at: (a) 2 (b) 4 (c) 6 (d) 8 (e) 10 hrs.

4.3.11 Energy Dispersive Spectroscopy

Figure 4.15 shows EDS analysis results, it can be observed that Fe, Cr, O, Ta and Ni are the main elements existing in the sputtered layer for coated samples at condition (2,4,6,8 and 10) hrs sputtering time. The existence of these elements confirms the formation of successful Tantalum oxide coating on the LDX 2101 DSS alloy.

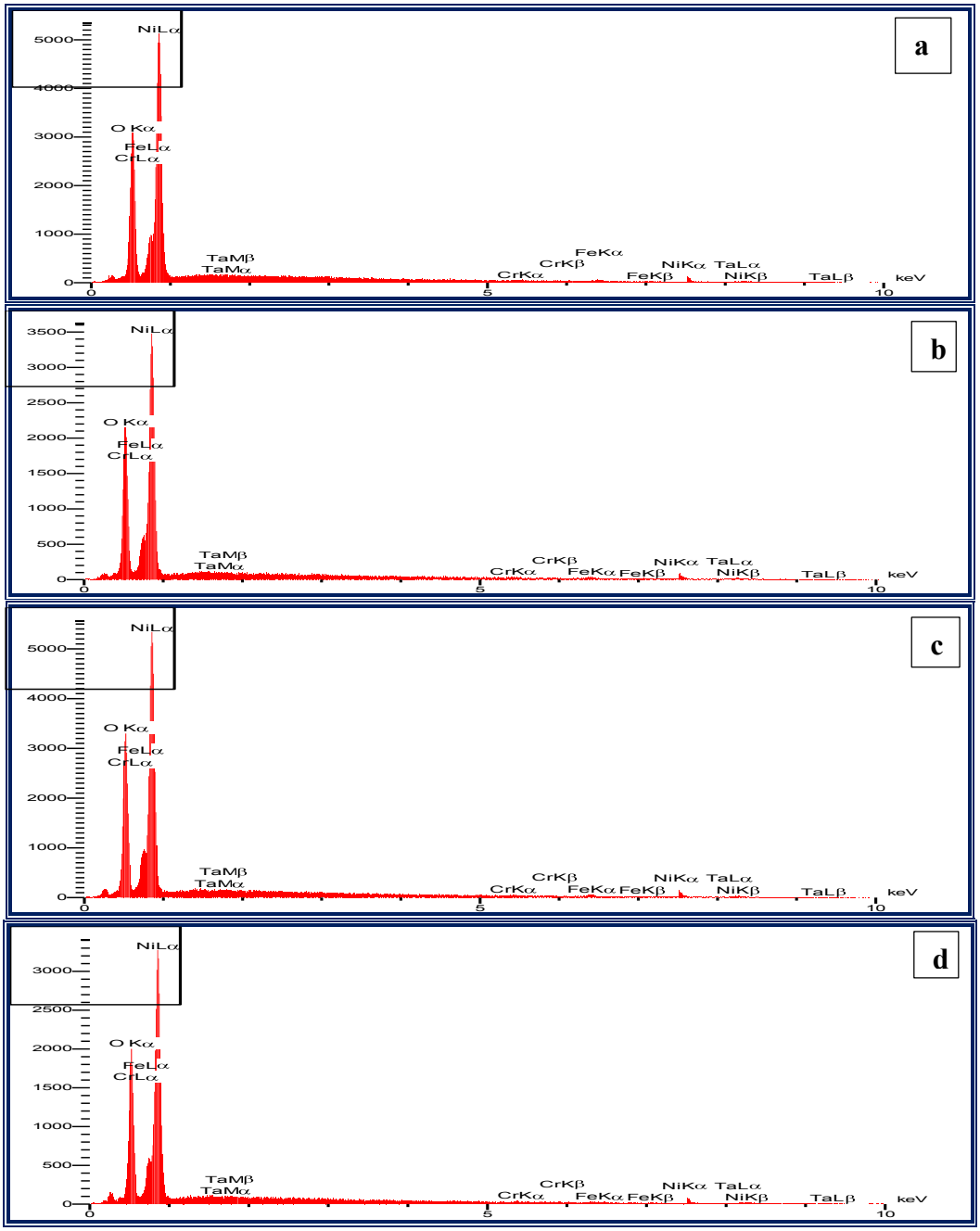

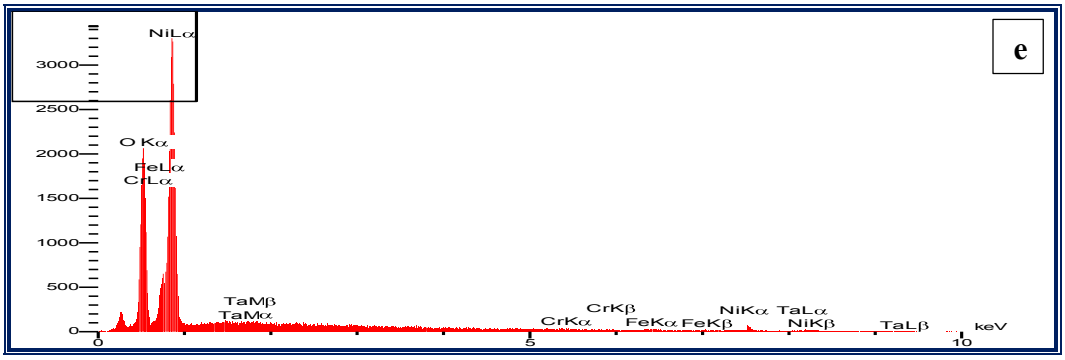

Figure 4.15 EDS analysis for sputtered samples with Ta_2O_5 at: 2 (b) 4 (c) 6 (d) 8 (e) 10 hrs.

4.3.12 X – Ray Diffraction Analysis

Identification of phases present in LDX 2101 DSS substrate before sputtering, and sputtered samples are characterized by using X-ray diffraction technique. The XRD results, (Figure 4.16), revealing crystalline α and γ phases in the reference (untreated) LDX sample, after sputtering Ta_2O_5 film crystallization possess a typical amorphous hump between 2θ angle of 20° - 40° [173]. Ta_2O_5 and TaO phases are identified in all the surfaces. Moreover, the broad peak of the pattern matches with the location of several peaks for oxide phases such as TaO_2 (ICDD card no 00–019-1297) and Ta_2O_5 (ICDD card no 00–025-0922), implying that either one or a mixture of these phases may be present [170]. Ta_2O_5 coatings are synthesized by using a reactive magnetron sputtering system, the deposited Ta_2O_5 exhibited amorphous structure [84,174].

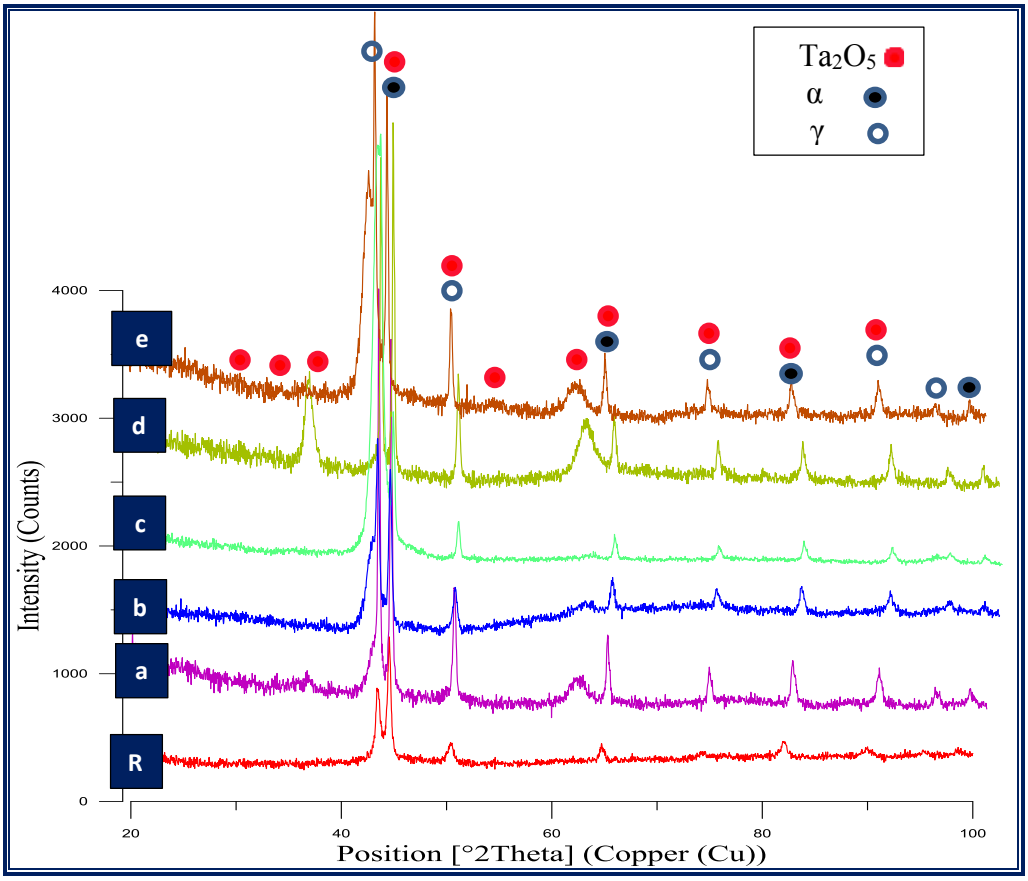

Figure 4.16 XRD patterns of sputtered LDX 2101samples with Tantalum oxide at: (R) un coated (a) 2 (b) 4 (c) 6 (d) 8 (e) 10 hrs.

4.3.13 Atomic Force Microscopy Analysis

The AFM analysis is performed for the substrate LDX 2101 DSS and sputtered samples with Ta_2O_5 at (2,4,6,8 and 10) hrs. The topography of the sputtered samples and different particles distribution in Ta_2O_5 coating layer with 3D performance image is shown in Figure (4.17). The surface roughness of sputtered coated samples was (2.65, 2.71, 3.22, 3.6 and 6.11) nm respectively, which indicates that when time of sputtering increases, roughness of sputtered coating layer increases [175]. This Figure also shows different particles distributions and the granularity accumulations for the coated layers for the mentioned samples with average diameters of (846.92, 934.69, 1032.25, 1109.00 and 1196.36) nm respectively in these conditions, the tantalum oxide surface is characterized by the irregular localization of particles that increase with increasing sputtering time [84,128,170].

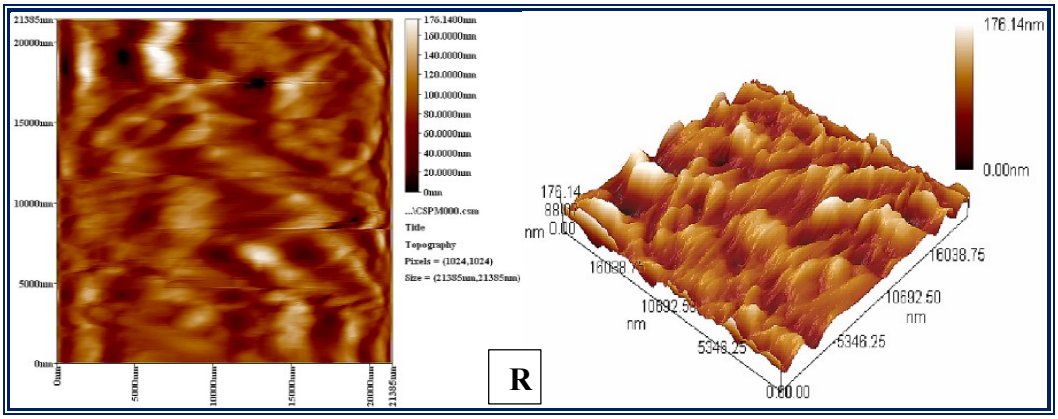
R
176.14nm
0.00nm
Title
Topography
Pixels = (1024,1024)
Size = (21385nm,21385nm)

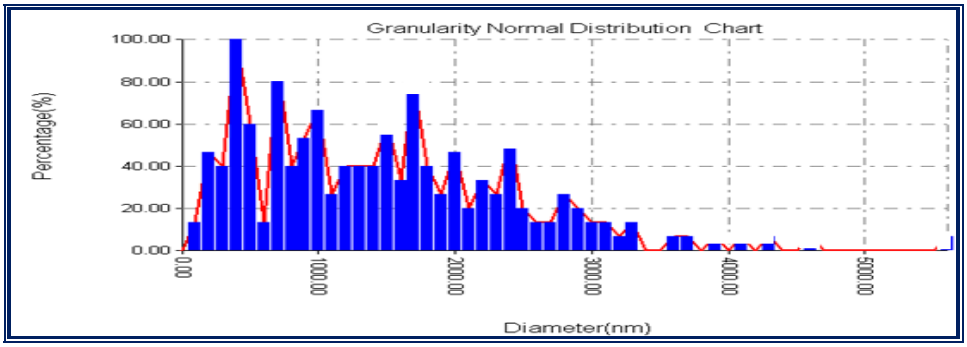
Granularity Normal Distribution Chart
Percentage(%)
Diameter(nm)

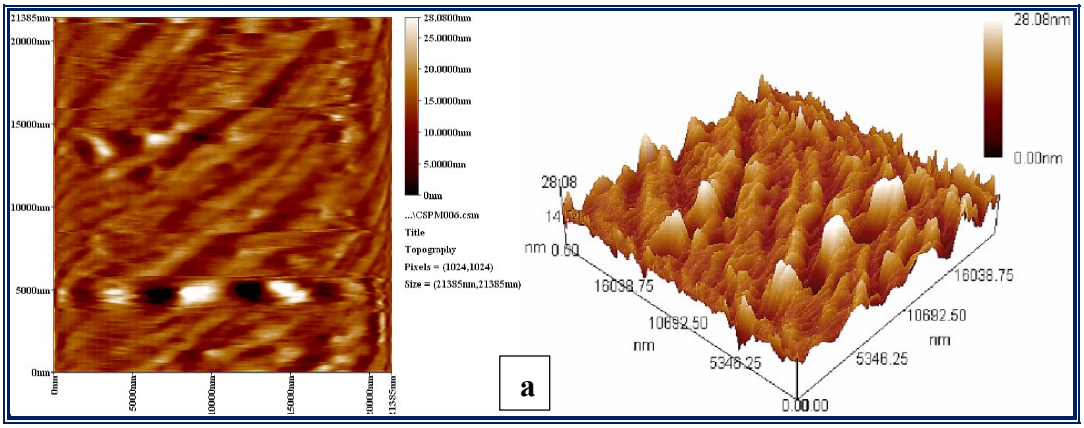
a
28.08nm
0.00nm
Title
Topography
Pixels = (1024,1024)
Size = (21385nm,21385nm)

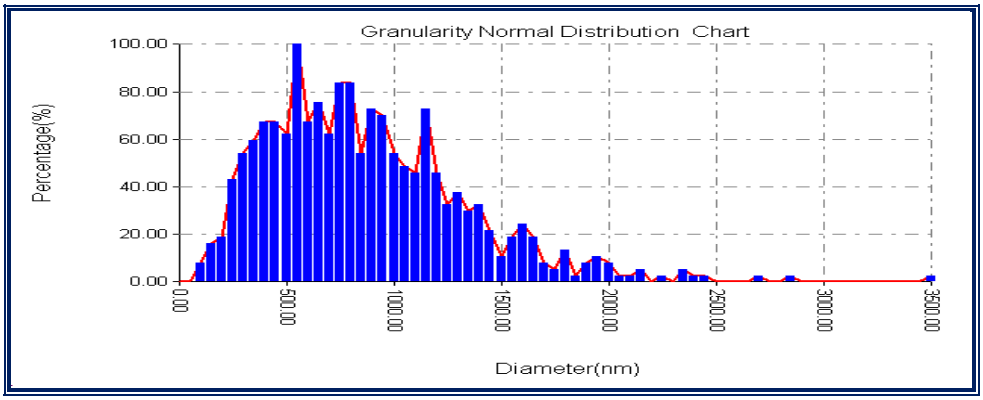
Granularity Normal Distribution Chart
Percentage(%)
Diameter(nm)

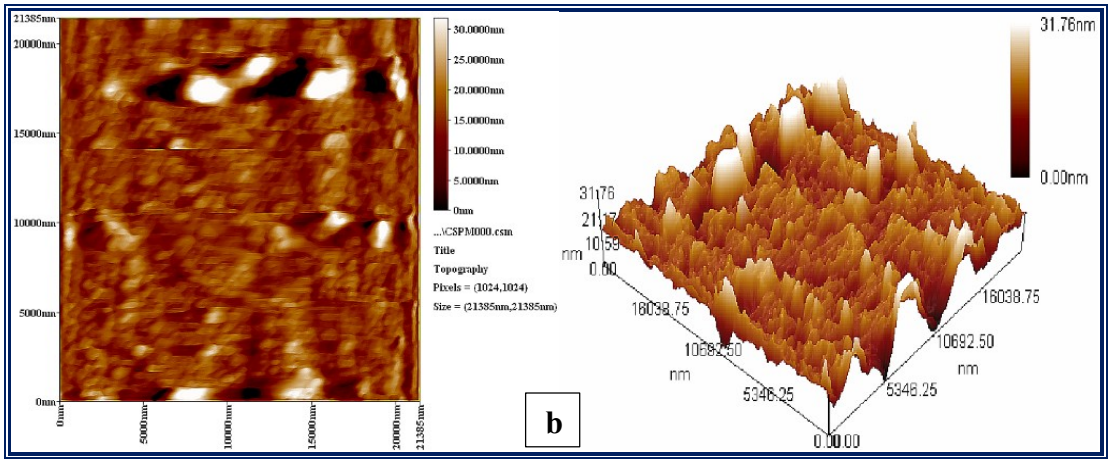
21385nm
20000nm
15000nm
10000nm
5000nm
0nm
50.0000nm
25.0000nm
20.0000nm
15.0000nm
10.0000nm
5.0000nm
0nm
...\CSPM000.csm
Title
Topography
Pixels = (1024,1024)
Size = (21385nm,21385nm)
31.76nm
0.00nm
31.76
21.17
10.59
0.00
nm
16038.75
10692.50
5346.25
0.00
b

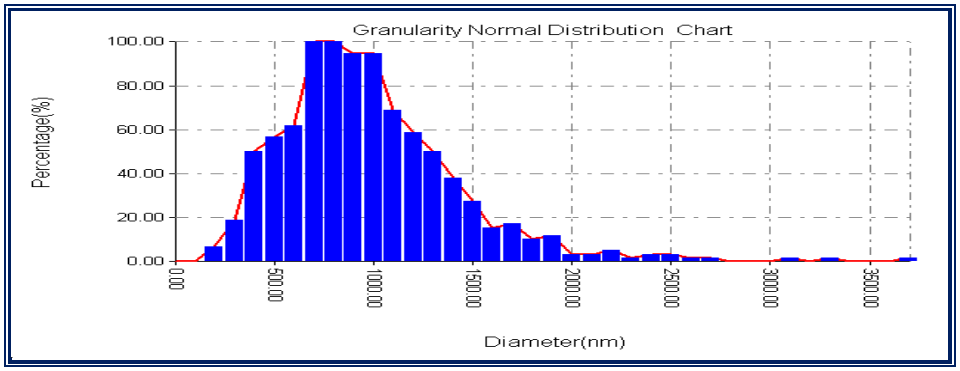
Granularity Normal Distribution Chart
Percentage(%)
100.00
80.00
60.00
40.00
20.00
0.00
Diameter(nm)

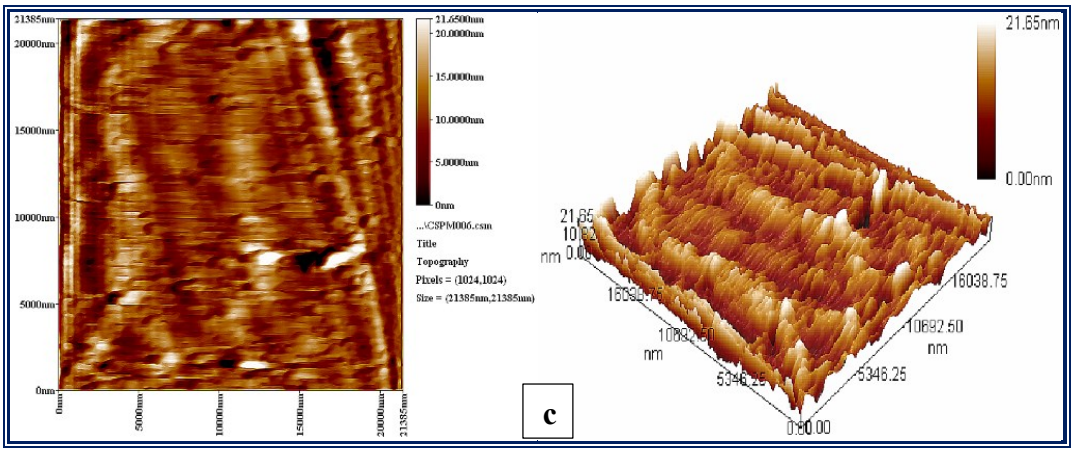
21385nm
20000nm
15000nm
10000nm
5000nm
0nm
21.6500nm
20.0000nm
15.0000nm
10.0000nm
5.0000nm
0nm
...\CSPM006.csm
Title
Topography
Pixels = (1024,1024)
Size = (21385nm,21385nm)
21.65nm
0.00nm
21.65
10.83
0.00
nm
16038.75
10692.50
5346.25
0.00
c

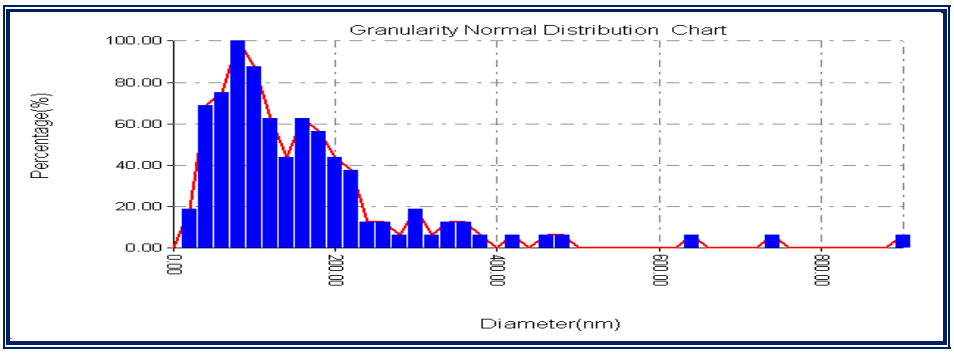
Granularity Normal Distribution Chart
Percentage(%)
100.00
80.00
60.00
40.00
20.00
0.00
Diameter(nm)

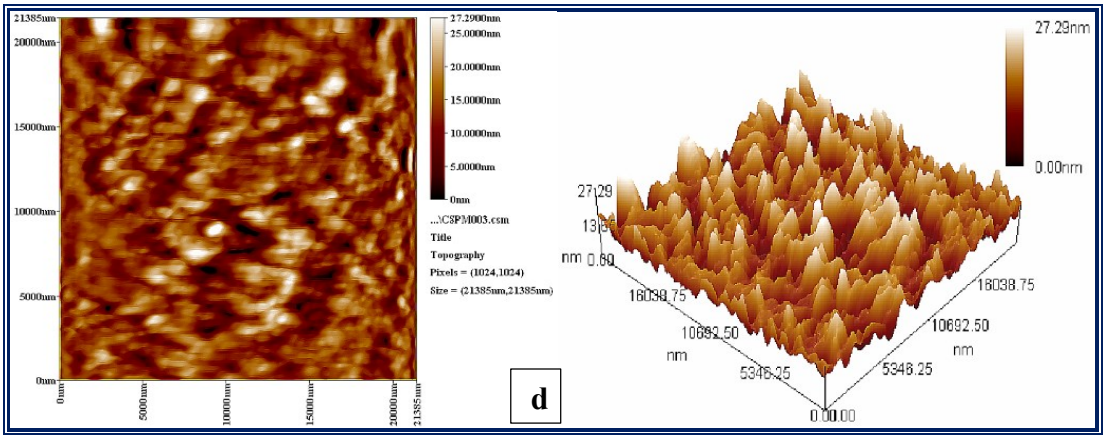

Figure 4.17 The topography of the Tantalum oxide coated samples with 3D performance images and granularity accumulation chart for particles at: (a) 2 (b) 4 (c) 6 (d) 8 (e) 10 hrs.

4.3.14 Antibacterial Teat

The antibacterial effect is more obvious for the deposited Ta_2O_5 coating samples than for the uncoated alloys as shown in Figure (4.18). Depending on the coating structures (amorphous and crystalline phases), the amorphous and crystalline Ta_2O_5 exhibits good antimicrobial performance against E. Coli, and has potential in medical applications. Ta_2O_5 coatings possess excellent cell viability and can be used as a surface modification for implant applications to increase the biocompatibility [85,174].

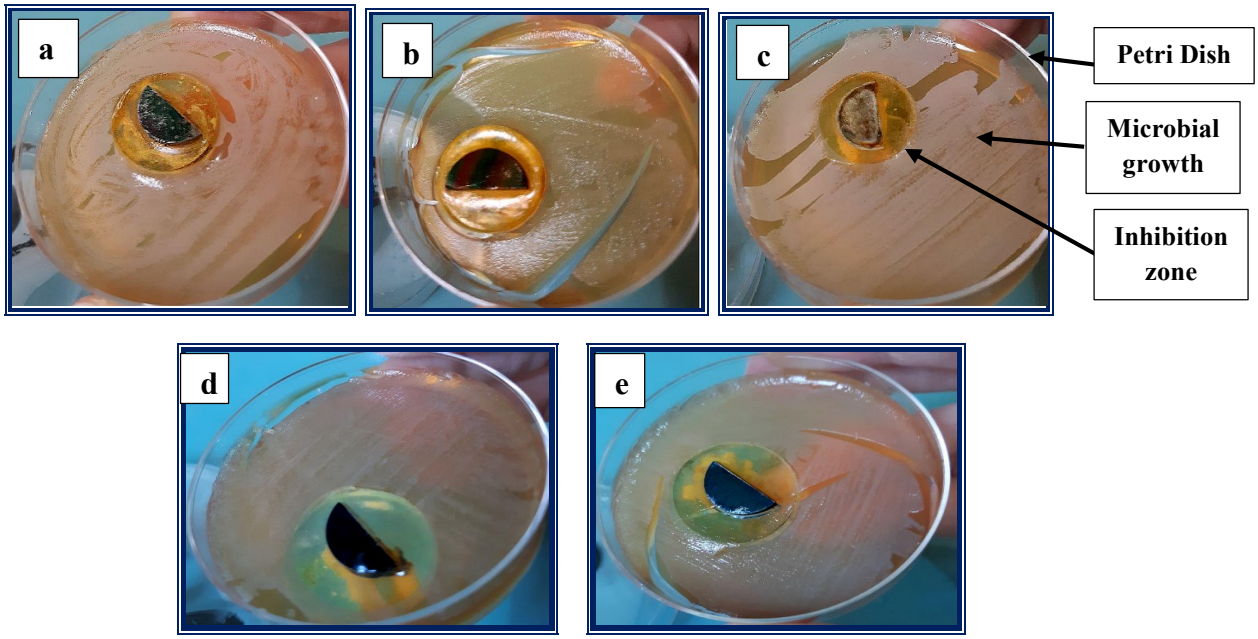

Figure 4.18 Optical photographs of antibacterial activity of E.coli performed for sputtered samples with Ta_2O_5 at: (a) 2 (b) 4 (c) 6 (d) 8 (e) 10 hrs.

4.3.15 Adhesion Test

Figure 4.19 shows the (OM) images of Rockwell C indentation with three different magnifications (5X, 10X, 20X) on the surface of sputtered samples with Ta_2O_5. Shallow and short cracks are observed around the indentation point in the sputtered samples with T_2O_5 at different times (2, 4, 6, 8 and 10) hrs. Furthermore, no delamination is observed around the Rockwell C indentation effect.

The only cracking on any of these films is located within the indentation and is minimal. All samples have an HF rating of 1, which implies that all tantalum films and coatings deposited by sputtering exhibit good adhesion regardless of thickness. When deposition time increases, adhesion will increase [176].

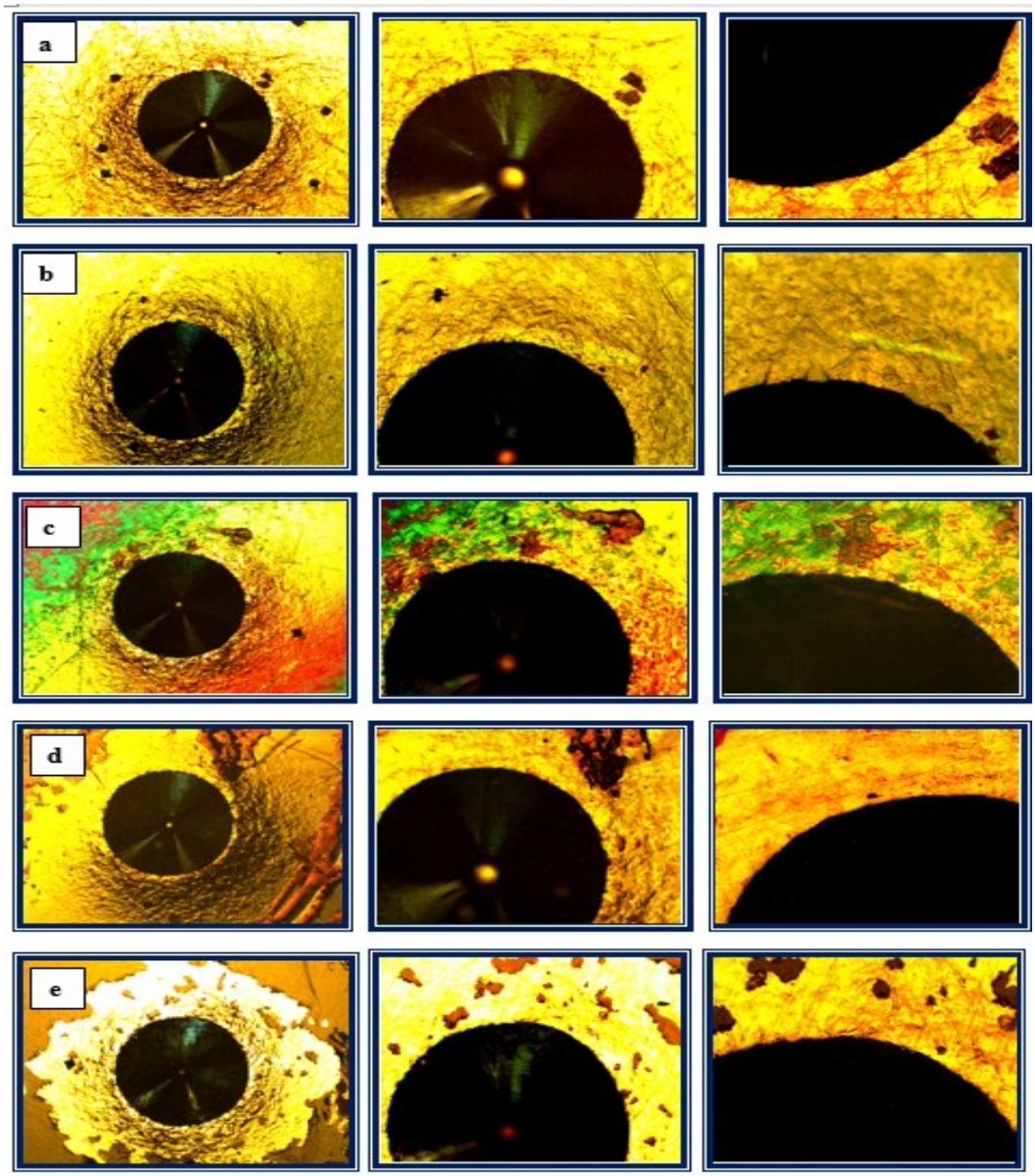

Figure 4.19 Optical photographs of Rockwell type - C effect an indentation for sputtered samples with Ta_2O_5 at: (R) un treatment (a) 2 (b) 4 (c) 6 (d) 8 (e) 10 hrs.

4.3.16 Corrosion Behavior

Corrosion behavior of sputtering samples is studied by potentiodynamic and cyclic polarization tests.

4.3.16.1 Potentiodynamic Polarization

Figure 4.20 shows the potentiodynamic polarization curves for base LDX 2101 DSS alloy and sputtered samples in the Ringer's solution at 37 ±1 °C for different treatment times. The corrosion current densities (i_{corr}) and corrosion potentials (E_{corr}) are derived from the potentiodynamic curves by employing Tafel extrapolation (Table 4.4). Also, the corrosion rates (CR) were also included in this Table.

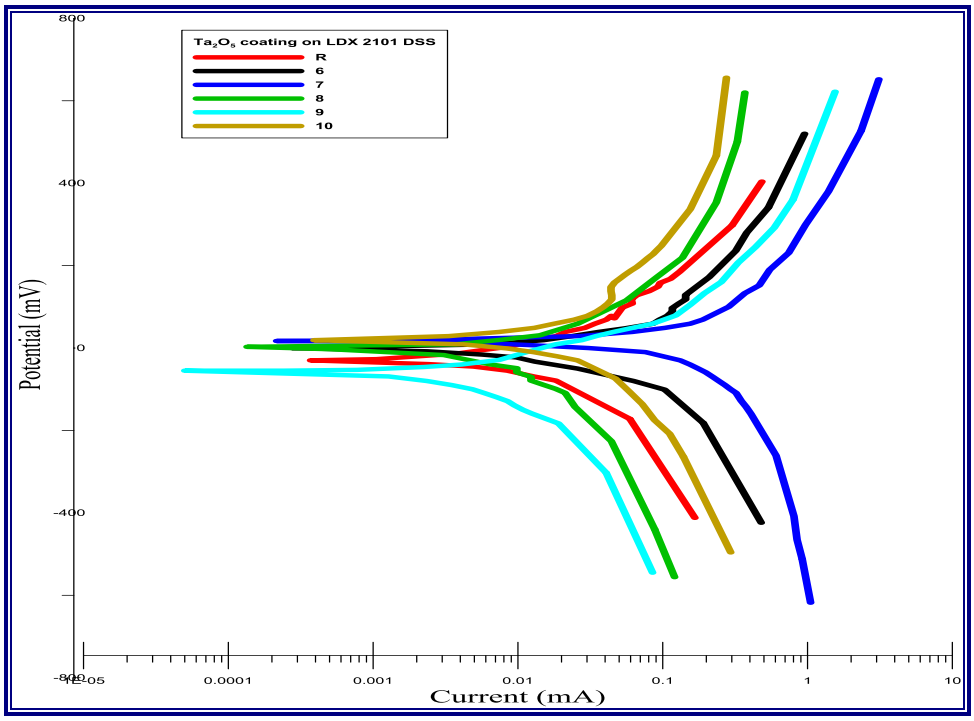

Figure 4.20 Potentiodynamic polarization curves of un treated LDX 2101 DSS and sputtered samples with Ta_2O_5 at different times in Ringer's solution at 37 ±1 °C.

It can be seen from the results obtained in Table 4.4, un–sputtered sample has corrosion current density (i_{corr} = 2.75 µA/cm^2), but the corrosion current density of all sputtered samples decreases, this means that sputtering with Ta_2O_5 coating layer provides a protective layer and barrier properties towards corrosion on the alloy surface [85] that would reduce the corrosion rate. The sputtering with lower time (2 hrs) results in incomplete deposition that produce a nonhomogeneous layer. The sputtering at 4 and 6 hrs, shows some micro cracks in the structure, (see Figure (4.13) – a, b and c), which leads to decrease current densities. When sputtering at 8 hrs, a lowest

corrosion current (i_{corr} = 0.102 µA/cm^2) is obtained and this result has the highest corrosion resistance between the other. This is attributed to dense structure of this coating layer and Ta_2O_5 film improves. In contrast, sputtering at 10 hrs has the lowest corrosion resistance than the other as a result of the thicker layer compared with the other samples. The corrosion tests reveal that the corrosion resistance of the Ta_2O_5 thin film coating is higher than that untreated LDX 2101 DSS after immersion in Ringer solution, which means that the substrate surface with a thin-film Ta_2O_5 layer notably enhances the passive layer's resistance. This study clearly suggests that using tantalum oxide reduces the risk of implant failure due to corrosion [86].

Table 4.4 Electrochemical parameters of the sputtered samples with Ta_2O_5 for LDX 2101 DSS at different times.

Sample no.	Condition	i_{corr} (µA/cm^2)	E_{corr} (mV)	CR(mpy)
R	Un treated	2.75	-34.52	1.329
6	2 hrs	2.530	-45.8	1.222
7	4 hrs	1.68	-25.4	0.811
8	6 hrs	1.38	-7.3	0.667
9	8 hrs	0.102	1.13	0.0492
10	10 hrs	2.72	7.9	1.314

Polarization resistance (Rp) measurements are used to determine the protective ability of sputtered ceramic layer since the registered Rp values are contrariwise proportional to the corrosion current (higher polarization resistance means lower corrosion current).

Based on Table 4.5, un–sputtered LDX 2101 DSS has low polarization resistance (Rp = 5.017 kΩ.cm^2). Sputtering led to increase in polarization resistance to (Rp = 101.832 kΩ.cm^2) at 8 hrs, which has lowest corrosion current density (0.102 µA/cm^2) led to lowest corrosion rate (0.0492).

Table 4.5 Polarization resistance of un–sputtered and sputtered LDX 2101 DSS samples with Ta_2O_5 coatings.

Sample no	Condition	i_{corr} (µA/cm^2)	βa (mV)	βc(mV)	Rp (kΩ.cm^2)
R	Un treated	2.75	80	-52.6	5.017
6	2 hrs	2.530	83.9	-159.4	9.005
7	4 hrs	1.68	85.1	-139.6	12.081
8	6 hrs	1.38	64.3	-103.4	14.435
9	8 hrs	0.102	50.3	-45.5	101.832
10	10 hrs	2.72	51.6	-84.4	5.118

4.3.16.2 Cyclic Polarization

The cyclic Potentiodynamic polarization of sputtered samples at different times has been investigated in the Ringer's solution at 37 ±1 °C as illustrated in Figure 4.21. It is clear that increasing sputtering time leads to increased pitting corrosion resistance up to 8 hrs.

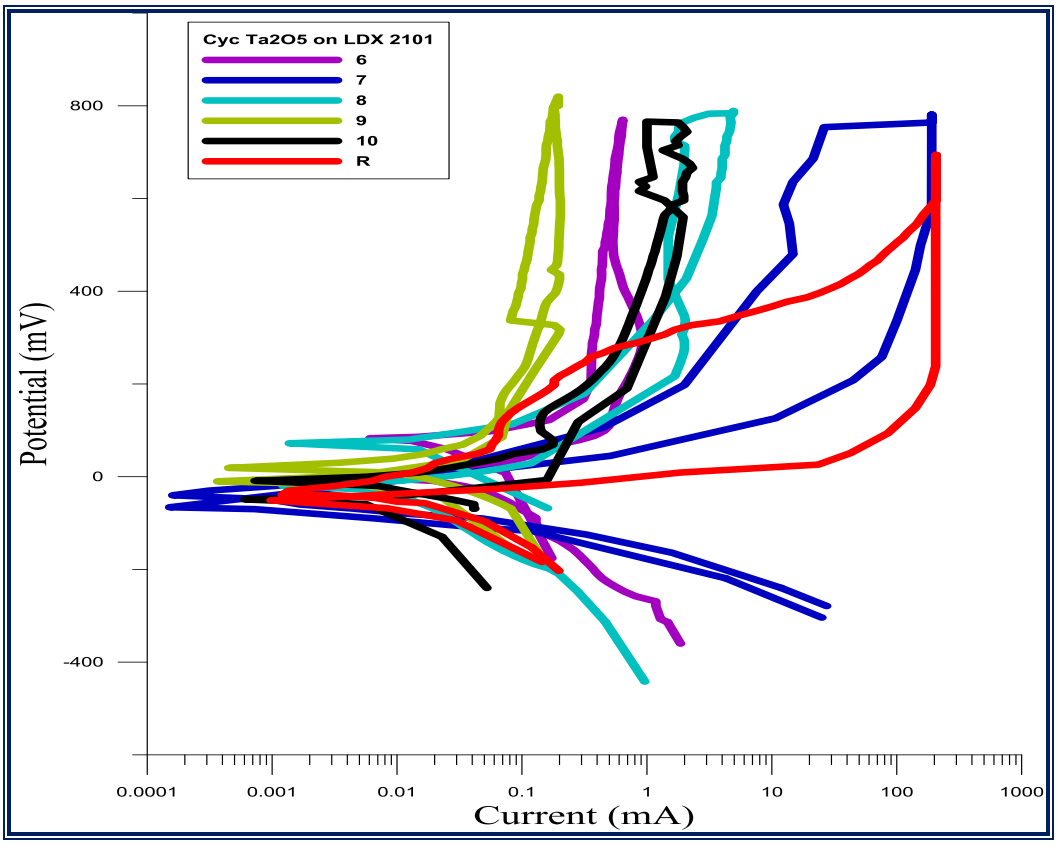

Figure 4.21 Cyclic polarization curves for un treated LDX 2101 DSS and sputtered samples with Ta_2O_5 at different times in Ringer's solution at 37 ±1 °C.

The sputtered sample at 10 hrs has the lowest pitting or break down potential and thus low resistance to pitting corrosion. This is due to the increase of coarse particles. But, the sputtered sample at 8 hrs has the highest pitting and protection potential with a close hysteresis loop where this polarization behavior tends to be resistance to the localized corrosion.

Table 4.6 contains values of Ep of an–sputtering and sputtered samples which are extracted from cyclic polarization curves. It indicated that when sputtering time increases, Ep increases then decreases at 10 hrs. Sputtering with Ta_2O_5 of LDX 2101 DSS increases resistance of pitting corrosion by a strong ability to act as barrier to prevent the localized corrosion attack of many aggressive ions appeared in Ringer's solution during the corrosion test [177]. Results obtained from potentiodynamic, and cyclic polarization tests reveal the excellent protection against corrosion provided by sputtering Ta_2O_5 coatings at 8 hrs. However, as cracking straight paths are not formed, the coating acts as an efficient protection to the base metal for the Ringer solution attack. The performance of the Ta-based coatings on LDX 2101 DSS suggests that new medical alloys coated with tantalum pentoxide will have an excellent performance and a large life time for orthopedic fields [178].

Table 4.6 Values of pitting potential for un–sputtered and sputtered samples with Ta_2O_5 at different times from cyclic polarization.

Sample no.	Condition	Ep (mV)
R	untreated	694
6	2 hrs	770
7	4 hrs	781
8	6 hrs	789
9	8 hrs	820
10	10 hrs	715

Part III: Tantalum Nitride Deposition by Plasma Sputtering Technique

4.3.17 Vickers Micro Hardness Test

The micro hardness initially increases with increasing sputtering time, then it decreases due to the thickness of sputtered layers, which is attributed to grain size, phase, residual stress, or the appearance of texture. The present TaN phase leads to increasing micro hardness. The residual stress is influenced by the stoichiometry, phase, film thickness, and deposition conditions [179][180]. Figure 4.22 shows micro hardness values of untreated and sputtered LDX 2101 samples with Tantalum Nitride.

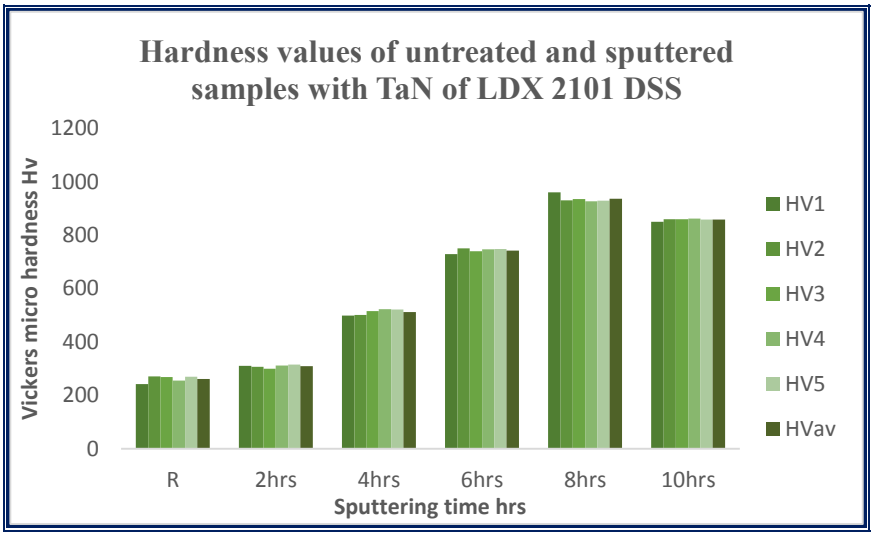

Figure 4.22 Histogram of hardness values for untreated and sputtered samples with TaN of LDX 2101 DSS.

4.3.18 Field Emission Scanning Electron Microscopy

The SEM surface micrograph in Figure 4.23 shows a smoother surface, typically observed in compact coatings grown with amorphous morphologies. It can be observed that the microstructure was densely packed and contained a homogeneous particle distribution, forming homogeneous coatings. As they appeared in Figure (4.23 - e) after 10 hrs, it can be observed that there are micro cracks and coarse particles. The use of

high sputtering time led to a considerable increase in the tendency for micro crack formation.

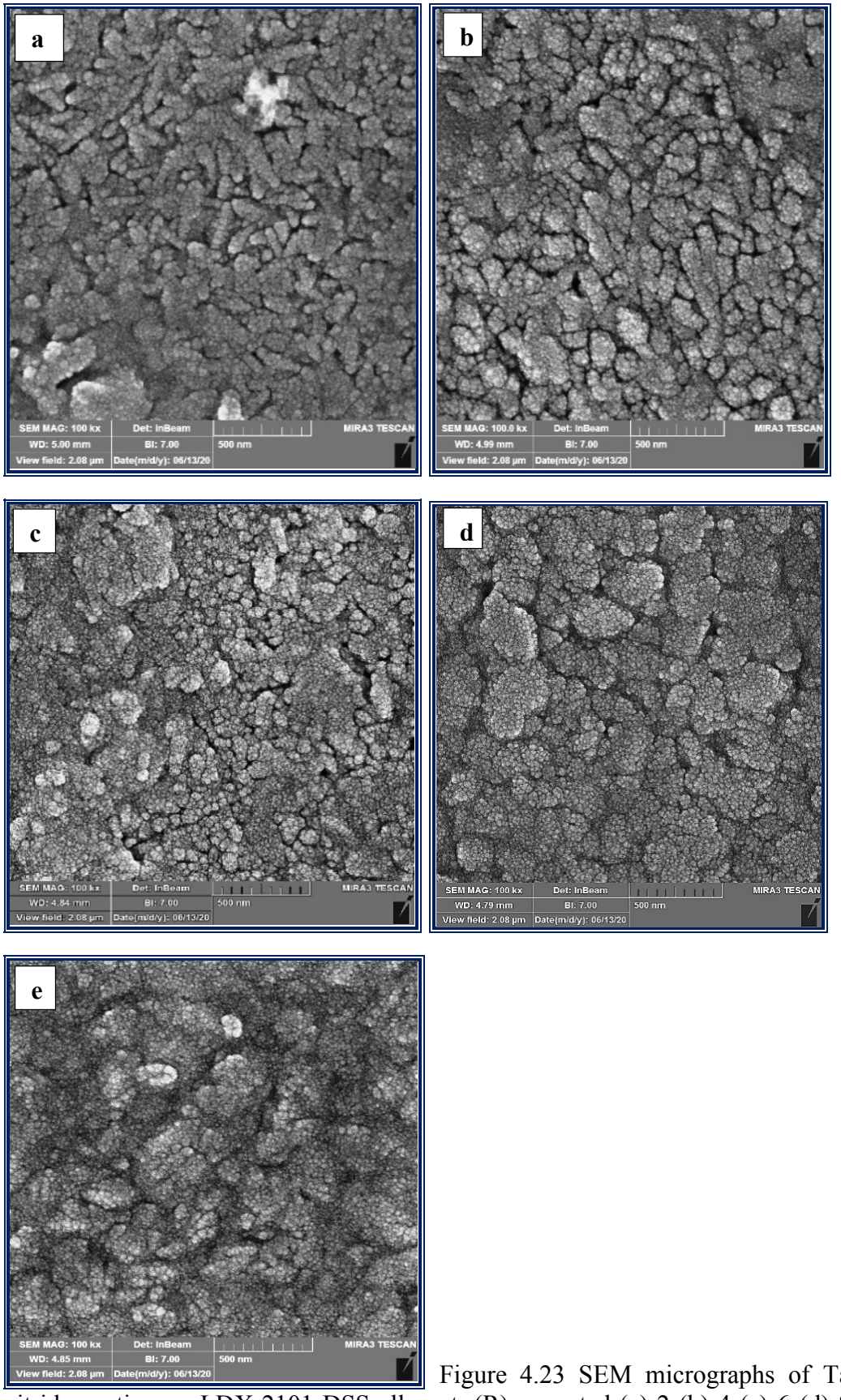

Figure 4.23 SEM micrographs of Tantalum nitride coating on LDX 2101 DSS alloy at: (R) uncoated (a) 2 (b) 4 (c) 6 (d) 8 (e) 10 hrs.

Figure (4.24) explains the cross-sectional topography of sputtered samples with TaN at (2,4,6,8 and 10) hrs. It can be noticed that the sputtered layer has a regular thin film structure of (27.44, 30.92, 31.43, 32.48 and 31.83) nm in thickness with higher compact, homogeneity and complete adhesion between the coating and the substrate. With the increase of sputtering time, thickness of coating layer increases significantly up to 8 hrs. As well as Figure (4.24) shows mapping of elements that present in sputtered TaN samples which are O, Cr, Fe, Ni, N and Ta that match with EDS analysis. The films are quite homogeneous and dense and no obvious micro-defects. Meanwhile, the films adhere tightly to the substrate. The results reveal that amorphous, homogeneous, compact, and adherent films composed of TaN. The thickness of coating layer increased then decreased with increasing sputtering time [181].

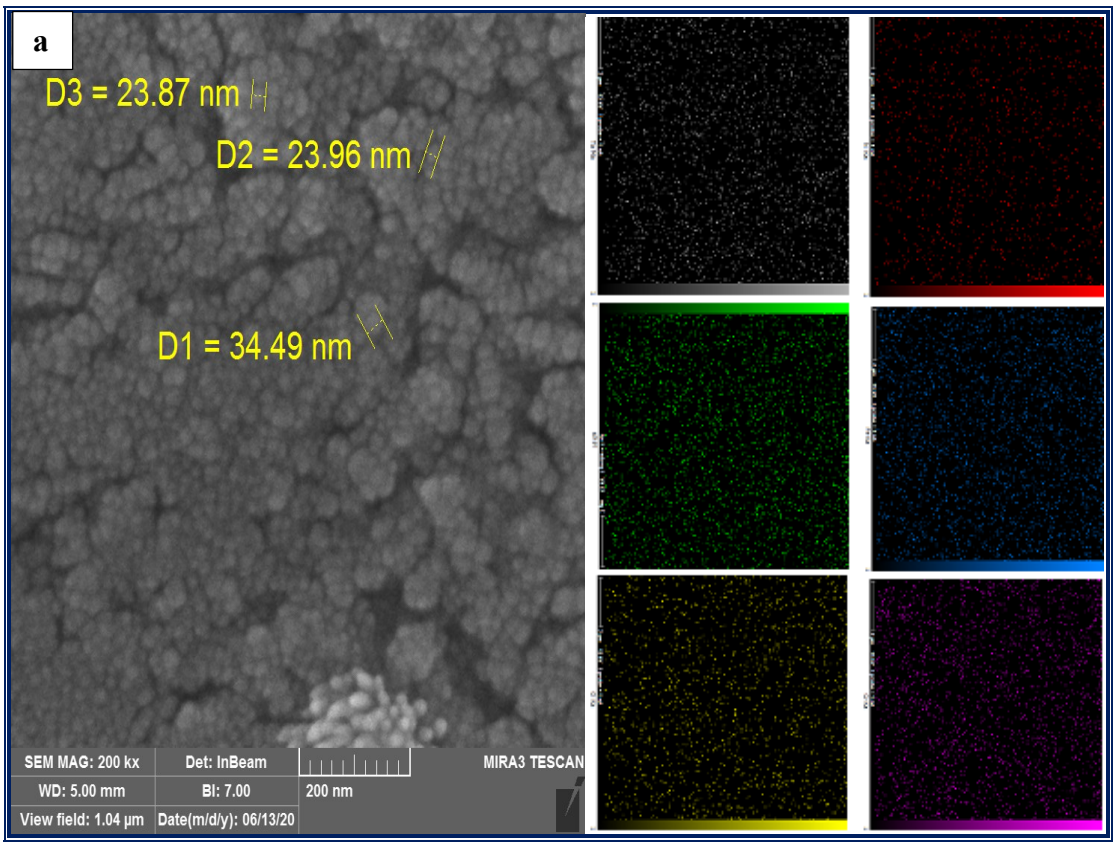

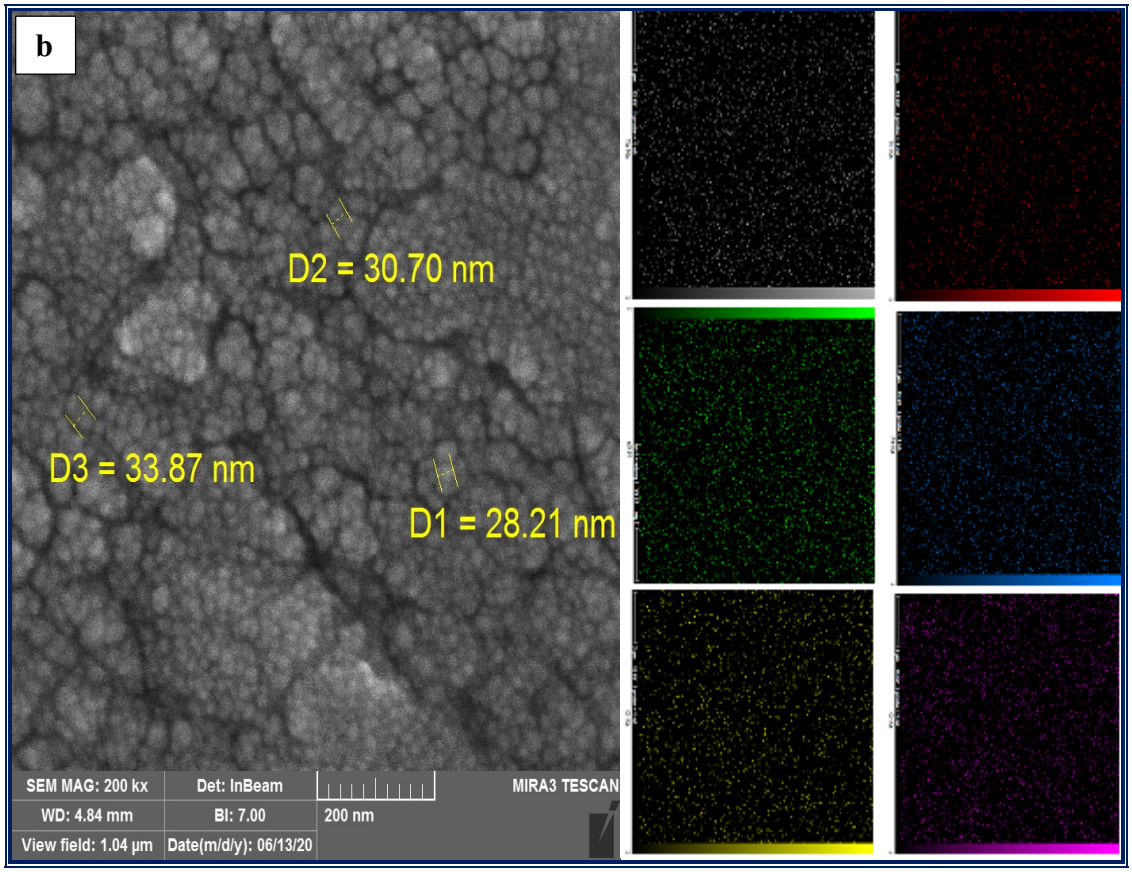
b
D2 = 30.70 nm
D3 = 33.87 nm
D1 = 28.21 nm
SEM MAG: 200 kx
Det: InBeam
MIRA3 TESCAN
WD: 4.84 mm
BI: 7.00
200 nm
View field: 1.04 µm
Date(m/d/y): 06/13/20

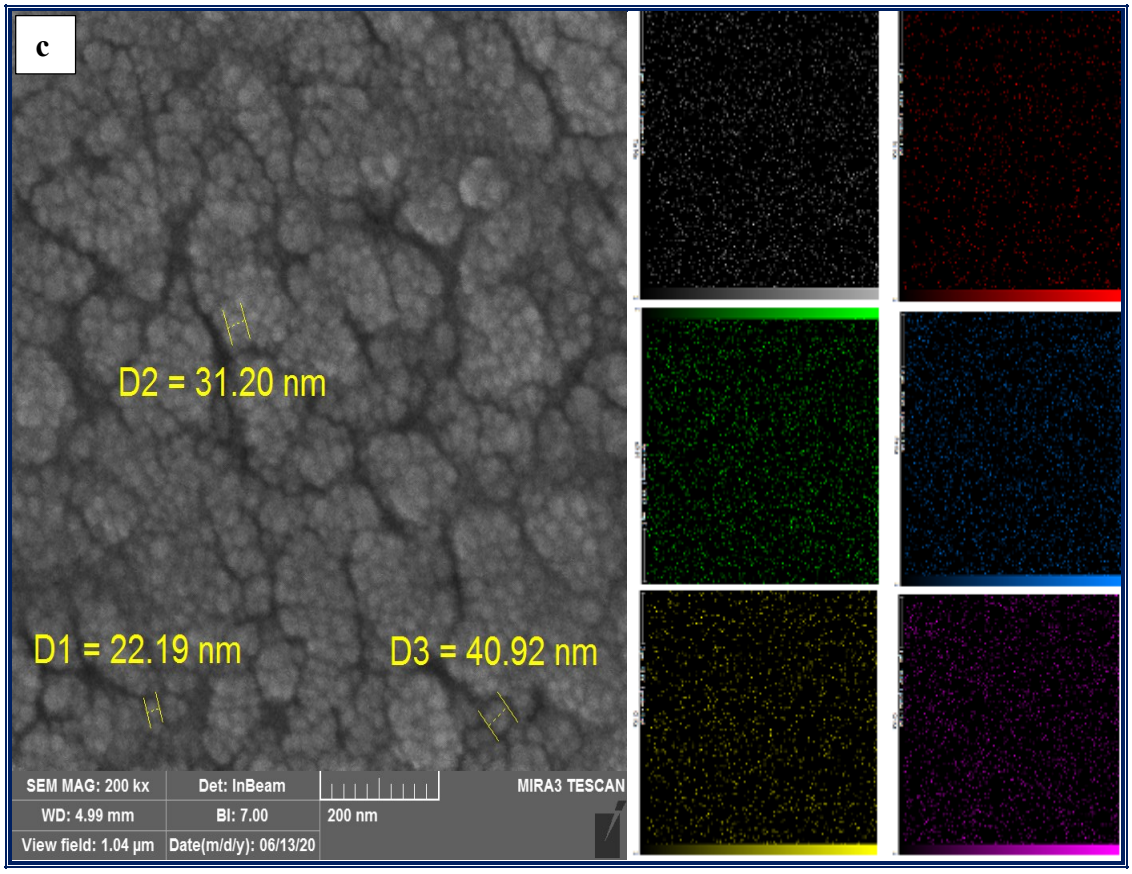
c
D2 = 31.20 nm
D1 = 22.19 nm
D3 = 40.92 nm
SEM MAG: 200 kx
Det: InBeam
MIRA3 TESCAN
WD: 4.99 mm
BI: 7.00
200 nm
View field: 1.04 µm
Date(m/d/y): 06/13/20

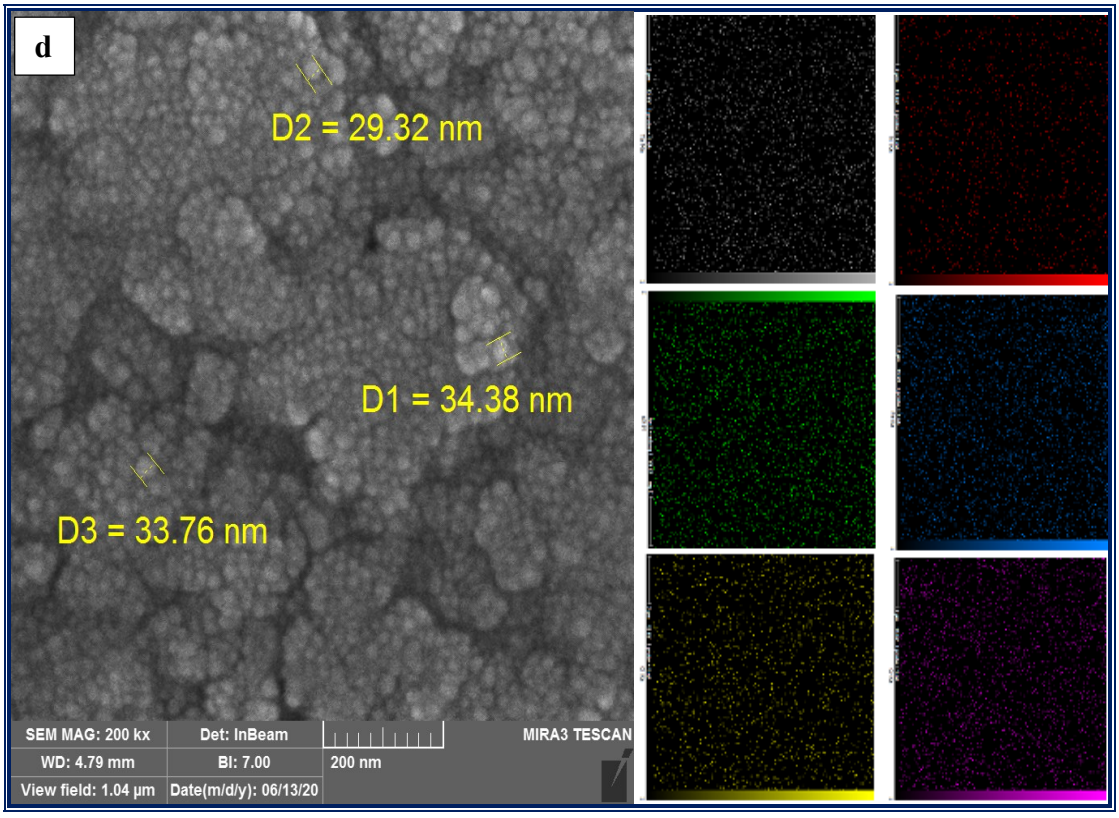

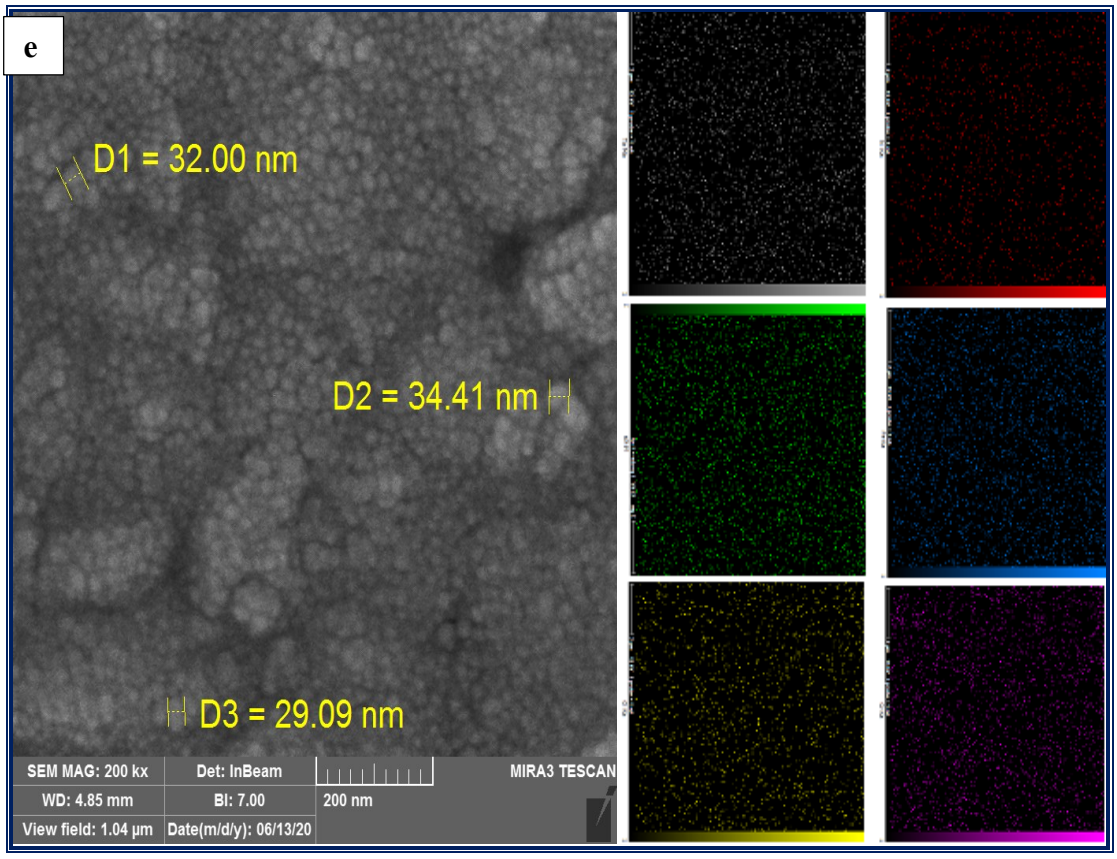

Figure 4.24 Cross-sectional SEM micrographs and EDS mapping of Tantalum nitride coating on LDX 2101 samples at: (a) 2 (b) 4 (c) 6 (d) 8 (e) 10 hrs.

4.3.19 Energy Dispersive Spectroscopy

The results of EDS analysis are shown in Figure 4.25, it can be seen that the main elements existing in the coatings are Fe, Cr, O, Ta and N. These elements existence approve the formation of successful Tantalum Nitride coating on the LDX 2101 DSS alloy. Moreover, there is no extra peaks different from TaN and this confirm the coating purity.

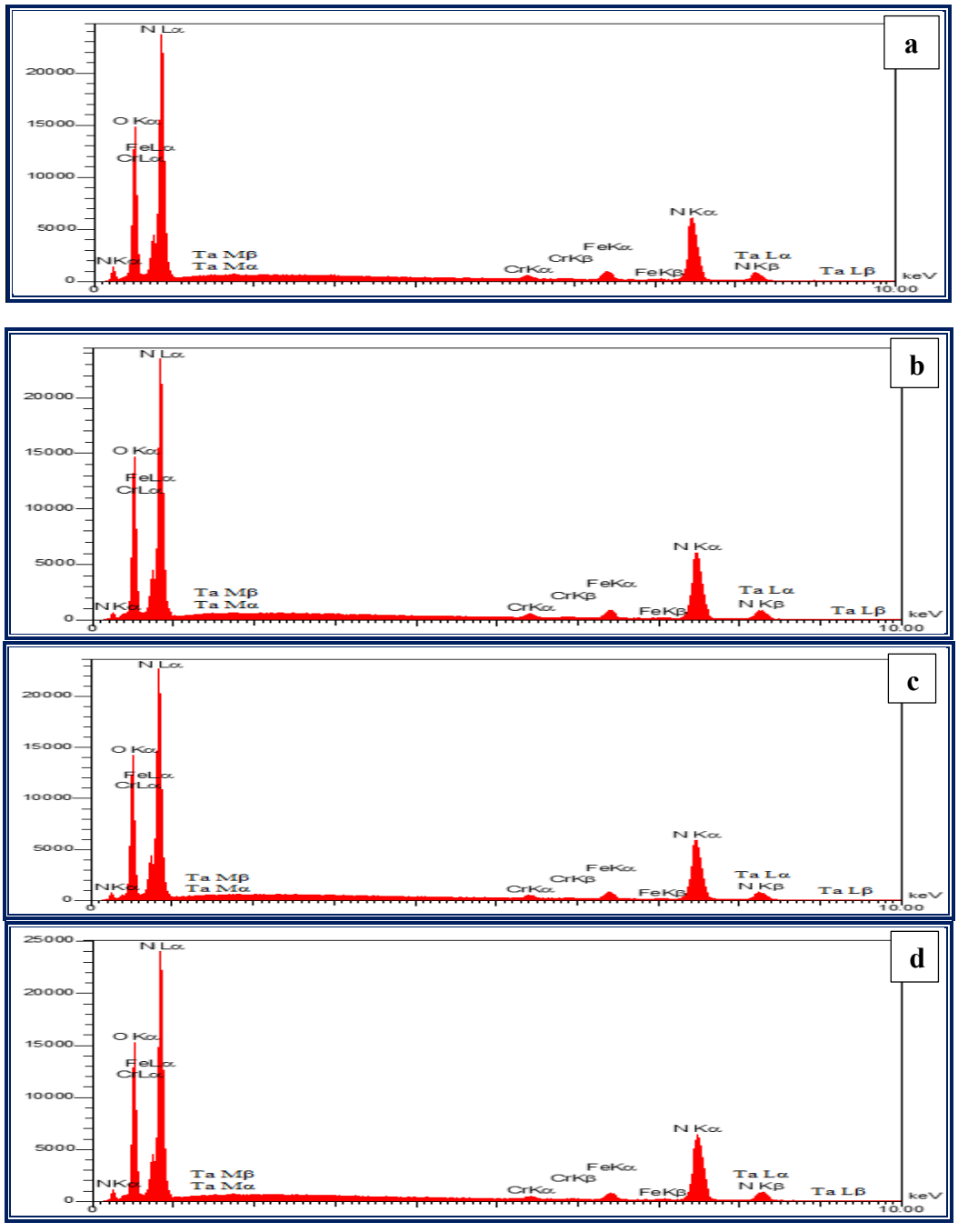

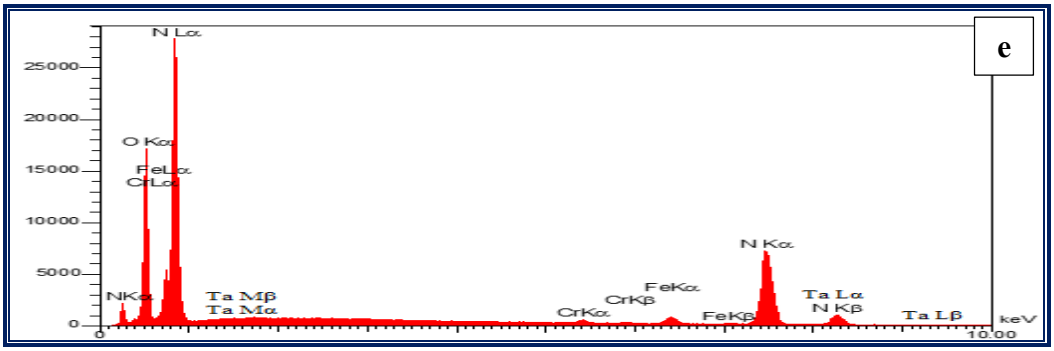

Figure 4.25 EDS analysis for sputtered samples with TaN at: (a) 2 (b) 4 (c) 6 (d) 8 (e) 10 hrs.

4.3.20 X-Ray Diffraction Analysis

XRD patterns of the uncoated LDX 2101 DSS sample and TaN coated samples by modified reactive plasma sputtering at different sputtering time (2, 4, 6, 8 and 10 hrs) are demonstrated in Figure 4.26 and these data are indexed according to the Powder Diffraction Files ferrite, austenite, TaN (JCPDS-ICDD file # 25-0922, 33-1391 and 33-1390) and TaN (JCPDS-ICDD file # 34-0977). The patterns of the plasma sputtered samples for 2, 4 and 6 hrs show wide peaks in the range of 2θ 20-40, which seems to be due to the formation of not fully crystalline TaN, whereas the patterns of the samples sputtered for 8 and 10 hrs show clear and prominent TaN peaks [129].

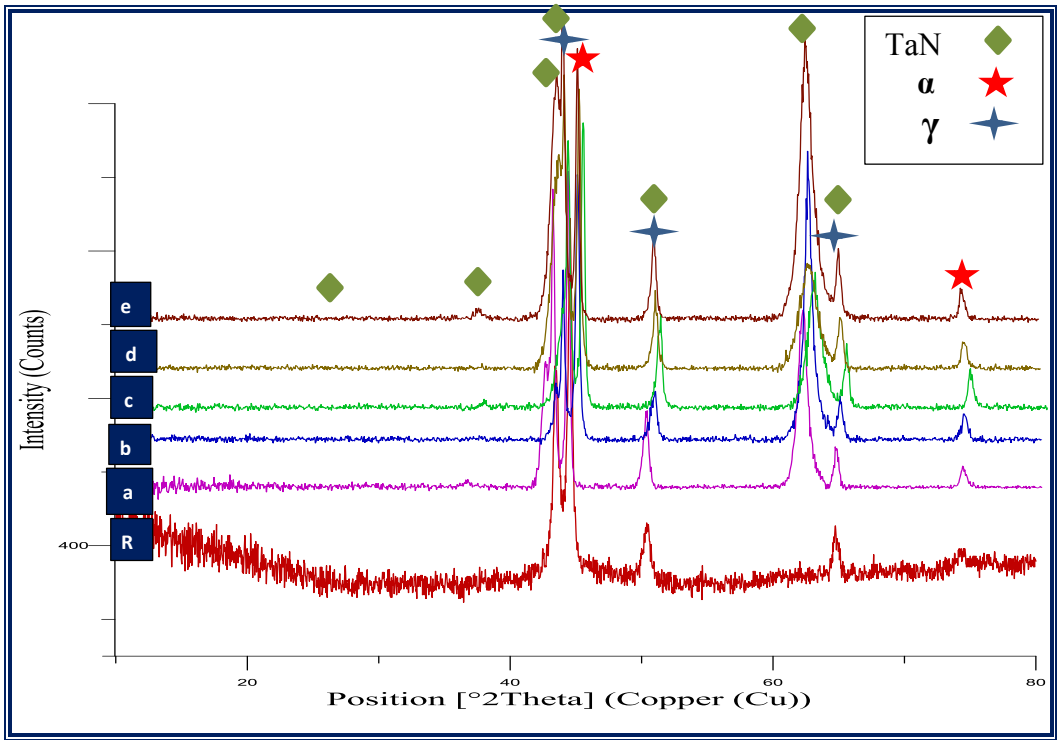

Figure 4.26 XRD patterns of coated LDX 2101samples with Tantalum nitride at: (R) un coated (a) 2 (b) 4 (c) 6 (d) 8 (e) 10 hrs.

4.3.21 Atomic Force Microscopy Analysis

The two-dimensional (2D) and three-dimensional (3D) AFM images of TaN films deposited at different deposition times are shown in Figure 4.27. The 2D images show the surface of the deposited TaN films is rather homogenous with the presence of a granular morphology. These morphological features seem to increase in size with time. In addition, the grains for films deposited at a higher time (10 hrs) are poor. Furthermore, the 3D images (Figure 4.27) show that, as time increases, the surface roughness first rises and then starts to drop (3.6, 4.14, 5.07, 8.36, and 7.2) nm, respectively. The surface of the film deposited at 2 hrs is quite smooth. With increasing time of sputtering, the surface roughness first increases until reaching a maximum value at 8 hrs. Above that time of 8 hrs, it decreases at 10 hrs. According to XRD, the simultaneous and competitive growth of c-TaN and N-rich nitride phases with distinct growth mechanisms could be responsible for the observed relatively rougher

surface at intermediate times. On the other hand, at low and high time, the deposition of one single phase is dominant. Moreover, the decrease in the surface roughness at high sputtering time can also be attributed to the lower film thickness (decrease in the deposition rate). Thick coatings may present dense columns that yield a rougher surface and leave (detrimental) open pores at the grain boundaries as a result of atomic followed deposition. Figure (4.27) also shows different particles distributions for the mentioned samples and the granularity accumulations for the coating layers with average diameters of (884.27, 915.56, 1030.23, 1100.66 and 1075.18) nm respectively [128].

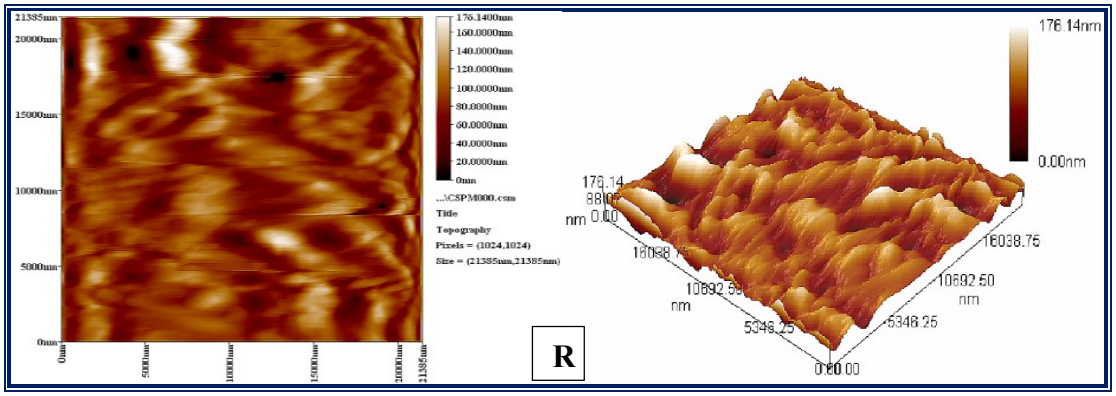

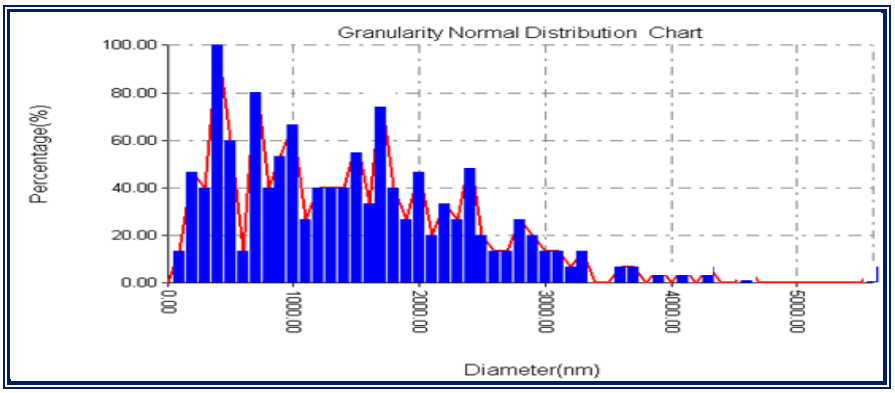

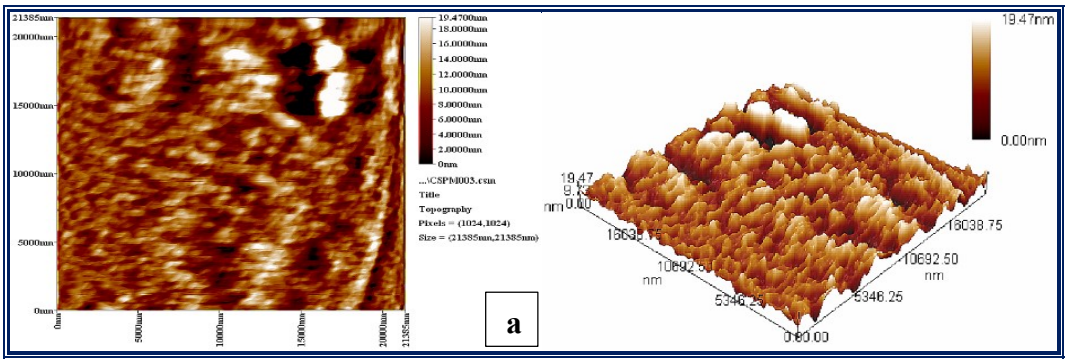

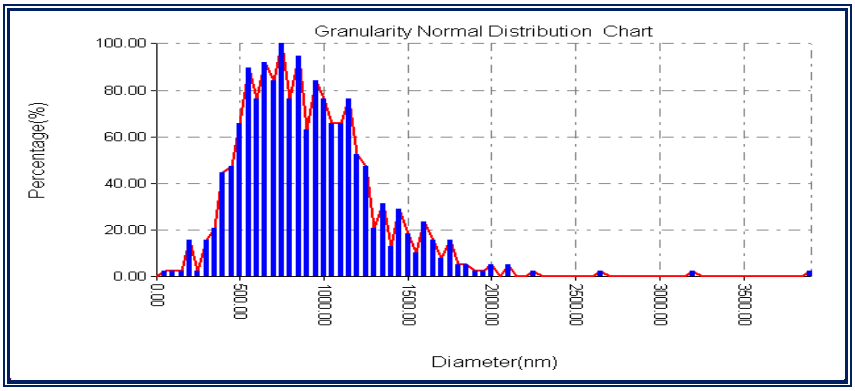
Granularity Normal Distribution Chart
Percentage(%)
100.00
80.00
60.00
40.00
20.00
0.00
0.00
500.00
1000.00
1500.00
2000.00
2500.00
3000.00
3500.00
Diameter(nm)

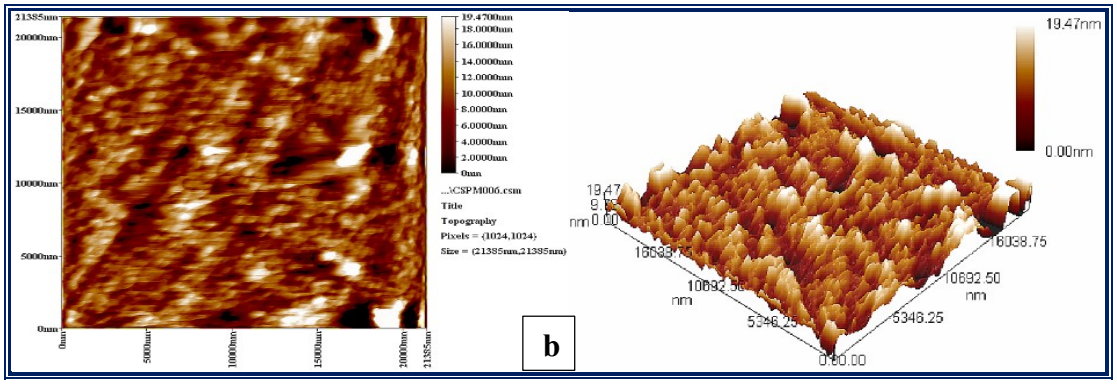
21385nm
20000nm
15000nm
10000nm
5000nm
0nm
19.4700nm
18.0000nm
16.0000nm
14.0000nm
12.0000nm
10.0000nm
8.0000nm
6.0000nm
4.0000nm
2.0000nm
0nm
...\CSPM006.csm
Title
Topography
Pixels = (1024,1024)
Size = (21385nm,21385nm)
19.47nm
0.00nm
16038.75
10692.50
nm
5346.25
0.00
b

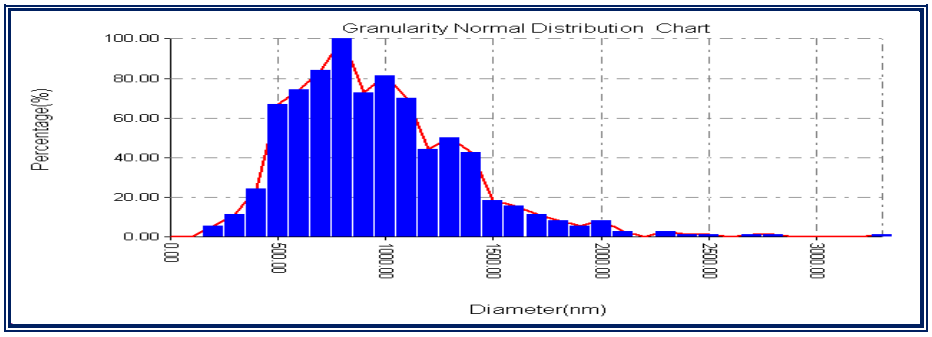
Granularity Normal Distribution Chart
Percentage(%)
100.00
80.00
60.00
40.00
20.00
0.00
0.00
500.00
1000.00
1500.00
2000.00
2500.00
3000.00
Diameter(nm)

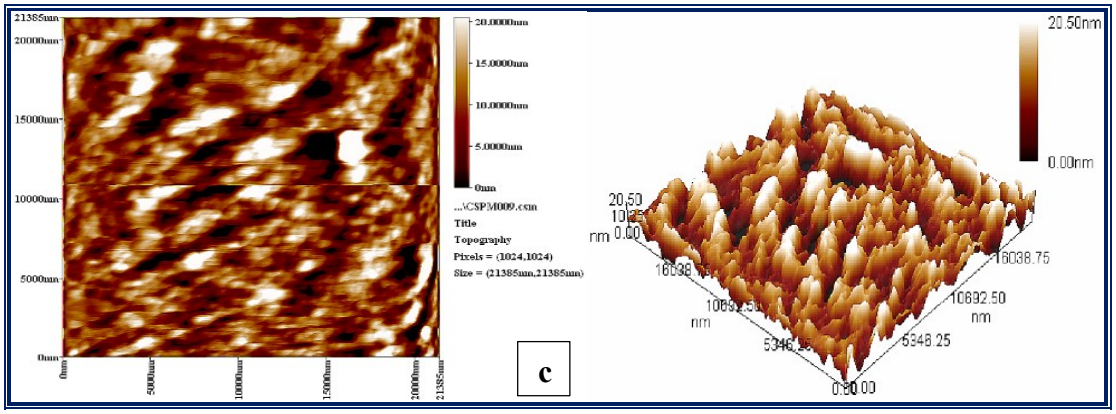
21385nm
20000nm
15000nm
10000nm
5000nm
0nm
20.0000nm
15.0000nm
10.0000nm
5.0000nm
0nm
...\CSPM009.csm
Title
Topography
Pixels = (1024,1024)
Size = (21385nm,21385nm)
20.50nm
0.00nm
16038.75
10692.50
nm
5348.25
0.00
c

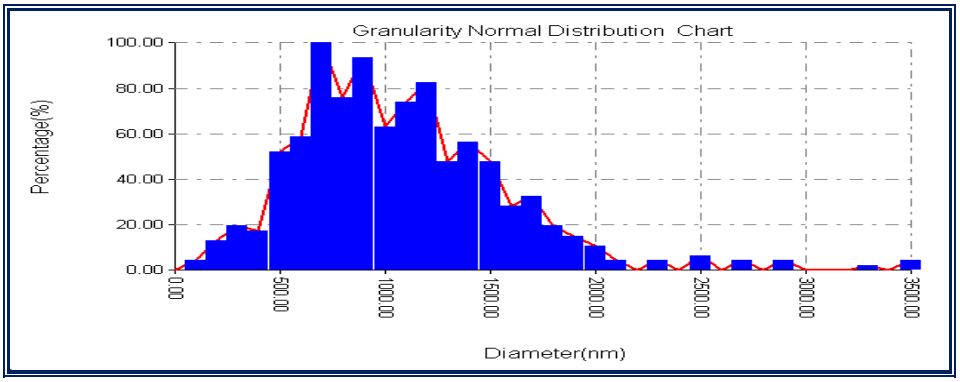
Granularity Normal Distribution Chart
Percentage(%)
100.00
80.00
60.00
40.00
20.00
0.00
0.00
500.00
1000.00
1500.00
2000.00
2500.00
3000.00
3500.00
Diameter(nm)

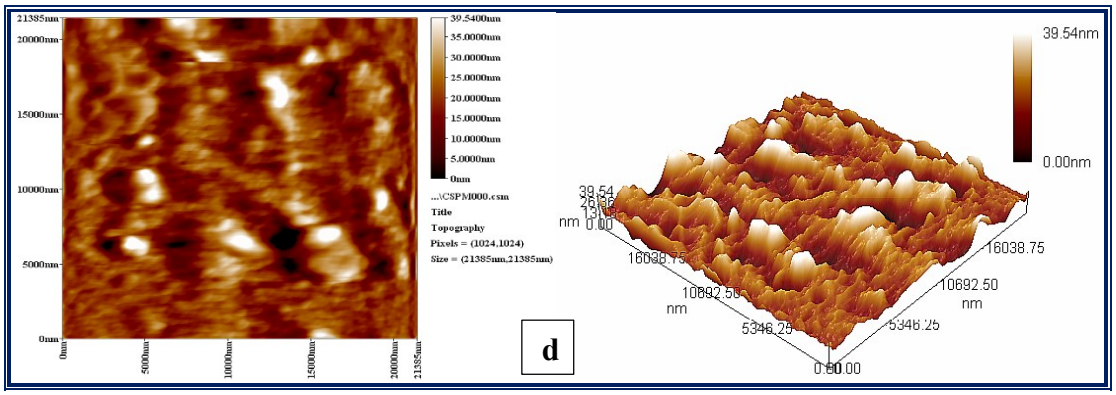
21385nm
20000nm
15000nm
10000nm
5000nm
0nm
39.5400nm
35.0000nm
30.0000nm
25.0000nm
20.0000nm
15.0000nm
10.0000nm
5.0000nm
0nm
...\CSPM000.csm
Title
Topography
Pixels = (1024,1024)
Size = (21385nm,21385nm)
39.54nm
0.00nm
16038.75
10692.50
5346.25
d

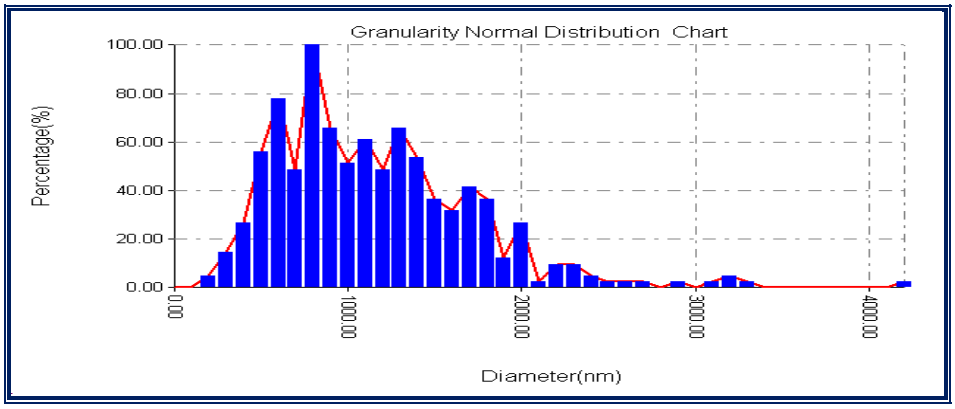
Granularity Normal Distribution Chart
Percentage(%)
100.00
80.00
60.00
40.00
20.00
0.00
0.00
1000.00
2000.00
3000.00
4000.00
Diameter(nm)

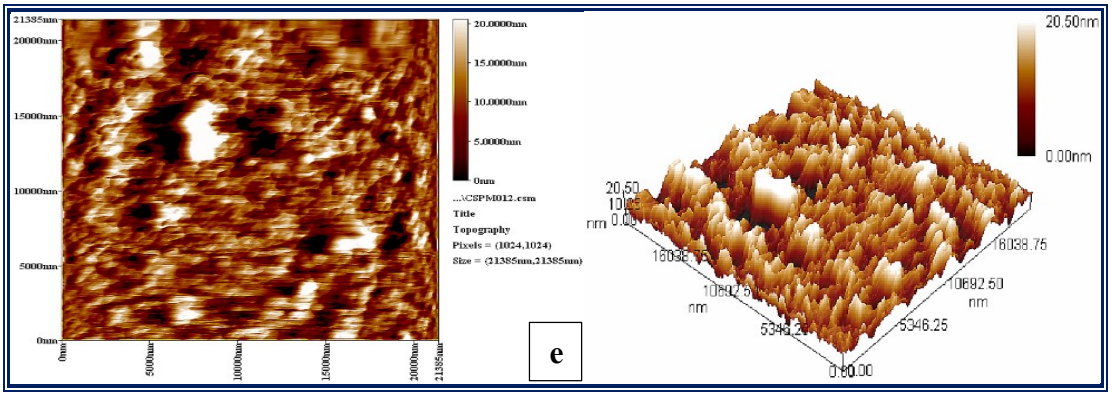
21385nm
20000nm
15000nm
10000nm
5000nm
0nm
20.0000nm
15.0000nm
10.0000nm
5.0000nm
0nm
...\CSPM012.csm
Title
Topography
Pixels = (1024,1024)
Size = (21385nm,21385nm)
20.50nm
0.00nm
16038.75
10692.50
5346.25
e

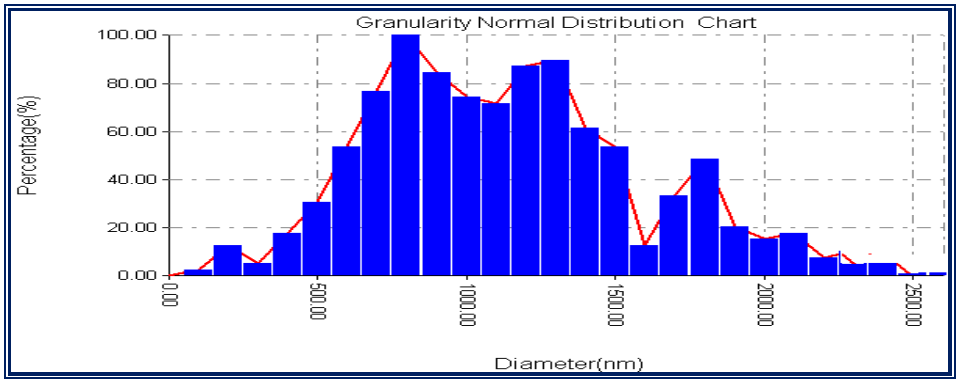

Figure 4.27 The topography of the Tantalum nitride coated samples with 3D performance images and granularity accumulation chart for particles at: (a) 2 (b) 4 (c) 6 (d) 8 (e) 10 hrs.

4.3.22 Antibacterial Test

Results of antibacterial test indicate that LDX 2101 DSS substrate without coating, in case of E. coli, some cell reduction as compared with control as shown in Figure 4.28. This suggests that there is some adhesion of microorganism cells to the particles of substrate, which may contribute to the overall reduction of cell number, so, it reduces the growth of bacteria. For sputtered samples, it has shown the highest antimicrobial activity, this refers to TaN coating active role in killing bacterial strains. According to the results illustrated in Figure 4.28 bacterial adhesion is significantly reduced for E. coli, which indicates that the bacterial strain may lose its replicating capacity, causing bacterial cell death. This means the presence of TaN completely kills bacterial strains, the bactericidal properties of TaN are due to the Ta ions release from the particles, which confers the activity of antimicrobial [182].

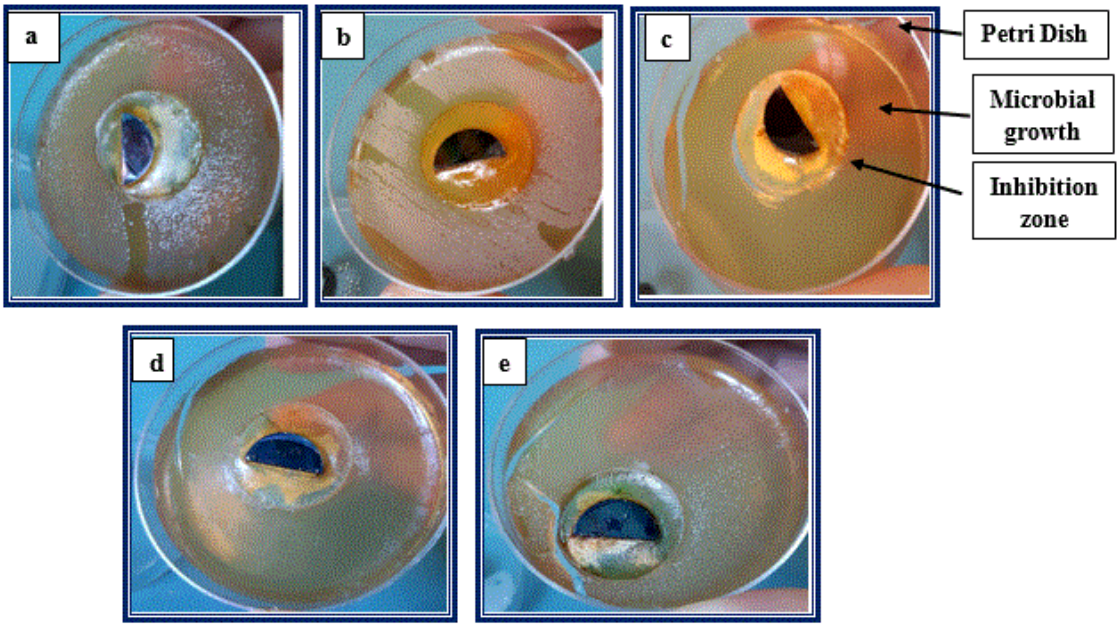

Figure 4.28 Optical photographs of antibacterial activity of E.coli performed for sputtered samples with TaN coating at: (a) 2 (b) 4 (c) 6 (d) 8 (e) 10 hrs.

4.3.23 Adhesion Test

Figure 4.29 shows the Optical microscope (OM) images of Rockwell C indentation with three different magnifications (5X, 10X, 20X) on the sputtered samples with TaN. Shallow and short cracks are observed around the indentation point in the sputtering samples with TaN at different deposition times (2, 4, 6, 8 and 10) hrs. Furthermore, no delamination is observed around the Rockwell C indentation effect. The only cracking on any of these films is located within the indentation and is minimal. All samples have an HF rating of 1 that implies all tantalum films and coatings deposited by sputtering in this study exhibit good adhesion regardless of thickness. All films and coatings exhibited good adhesion. The coatings also showed very little cracking indicating good adhesion to the substrate. The TaN coating exhibits good contact damage tolerance and sufficient adhesion strength to meet requirements for long term use in the human body under load bearing conditions [126].

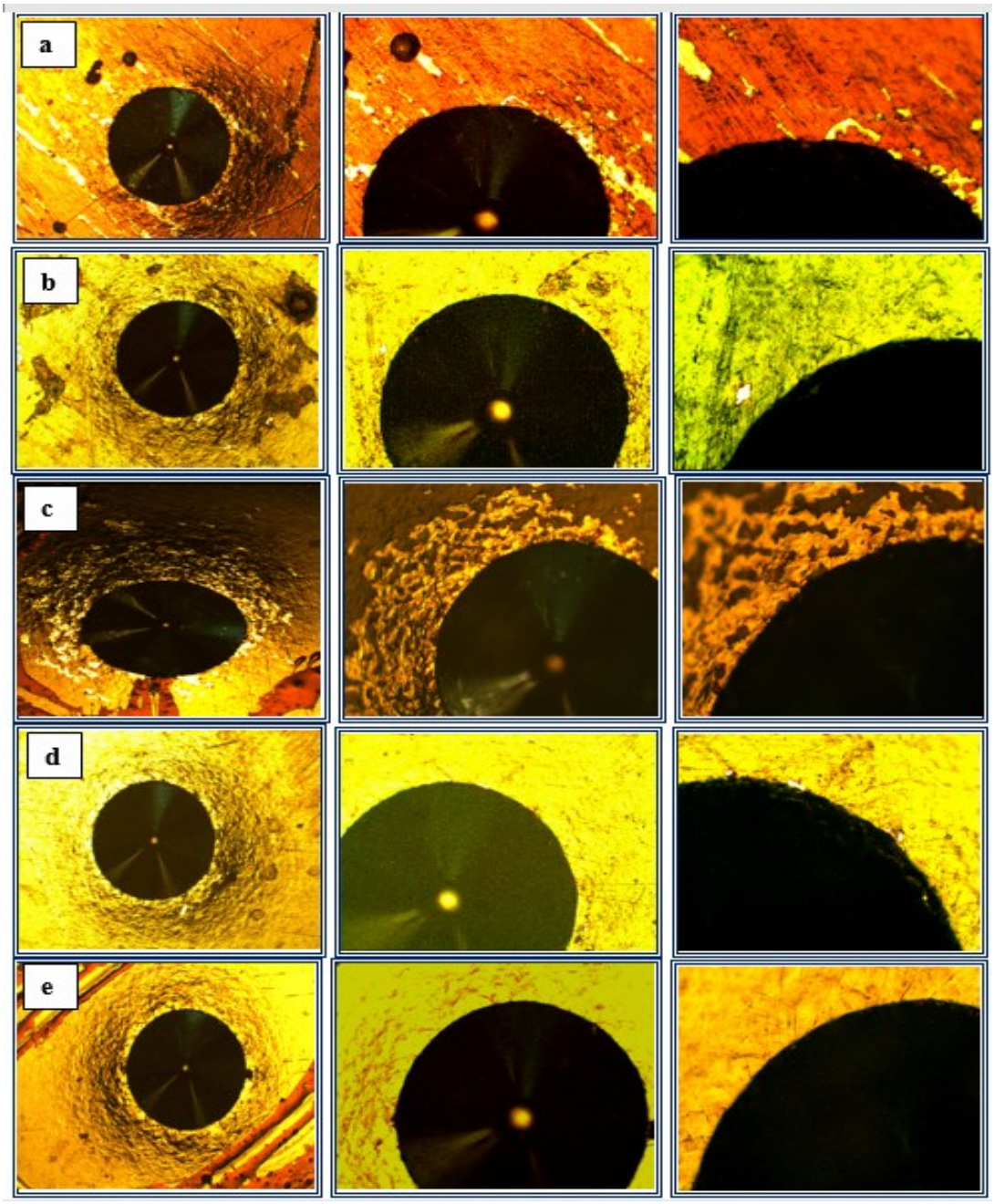

Figure 4.29 Optical photographs of Rockwell type - C effect an indentation for sputtered samples with TaN at: (R) un treated (a) 2 (b) 4 (c) 6 (d) 8 (e) 10 hrs.

4.3.24 Corrosion Behavior

Corrosion behavior of sputtering samples is studied by potentiodynamic and cyclic polarization tests.

4.3.24.1 Potentiodynamic Polarization

Figure 4.30 shows the potentiodynamic polarization curves for base LDX 2101 DSS alloy and sputtered samples with TaN in the Ringer's solution at

37 ±1 °C for different treatment times. The corrosion current densities (i_{corr}) and corrosion potentials (E_{corr}) are derived from the potentiodynamic curves by employing Tafel extrapolation (Table 4.7). Also, the corrosion rates (CR) were also included in this Table.

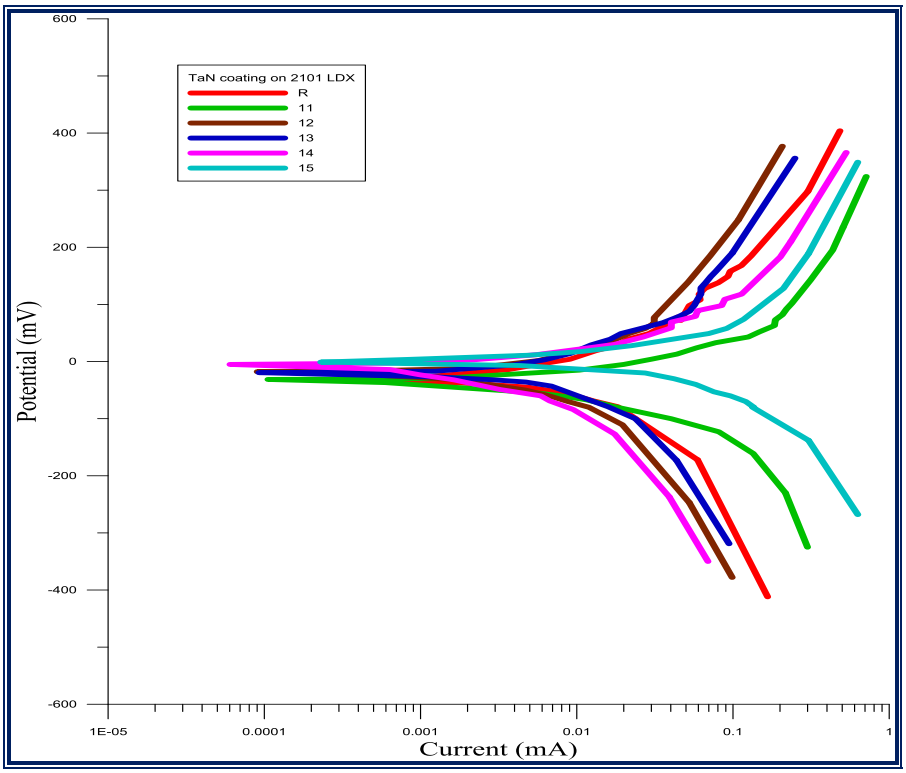

Figure 4.30 Potentiodynamic polarization curves of base LDX 2101 and sputtered samples with TaN of LDX 2101 at deposition time (2, 4, 6, 8 and 10) hrs.

It can be seen from the results obtained in Table 4.7, unmodified sample has corrosion current density (i_{corr} = 2.75 μA/cm^2), the sputtering with lower time (2 hrs) results in lacking deposition that not enough to produce a homogeneous layer, the low time treated samples show better corrosion resistance than the untreated sample. This mean that sputtering with TaN coating layer provide a protective passive layer on the alloy surface that would reduce the corrosion rate. But the corrosion current density of sputtered samples with TaN decreases at 2, 4, 6 up to 8 hrs then decreases at 10 hrs. When sputtering at 8 hrs, a lowest corrosion current (i_{corr} = 0.022 μA/cm^2) is obtained and this result has the highest corrosion resistance. This is attributed to dense structure of this coating layer [86].

Table 4.7 Electrochemical parameters of the sputtered samples with TaN for LDX 2101 DSS at different deposition times.

Sample no.	Condition	i_{corr} (µA/cm^2)	E_{corr} (mV)	CR (mpy)
R	Un treated	2.75	-34.52	1.329
11	2 hrs	2.191	-24.8	1.058
12	4 hrs	1.92	-7.3	0.927
13	6 hrs	1.38	-16.8	0.666
14	8 hrs	0.0456	-14.7	0.022
15	10 hrs	1.8	-16.3	0.869

In addition, coating at extension time leads to produce a coarse particles and inhomogeneity in the nitride layer that results in rough and poor deposit quality. On the other hand, sputtering at 10 hrs has the lowest corrosion resistance than the other as a result of the low layer thickness compared with the other samples. This is due to coarse nitride layer produced at higher deposition time during sputtering process in addition to the occurrence of fast-localized corrosion inside the cracks and pores as verified by cyclic corrosion.

Polarization resistance (Rp) measurements are used to determine the protective ability of sputtering samples since the registered Rp values are contrariwise proportional to the corrosion current (higher polarization resistance means lower corrosion current). The corrosion rate is directly related to the Rp.

Table 4.8 Polarization resistance of un–sputtered and sputtered LDX 2101 DSS samples with TaN.

Sample no.	Condition	Icorr (µA/cm^2)	βa (mV)	βc(mV)	Rp (kΩ.cm^2)
R	Un treated	2.75	80	-52.6	5.017
6	2 hrs	2.530	83.9	-159.4	9.446
7	4 hrs	1.68	85.1	-139.6	13.682
8	6 hrs	1.38	78.3	-103.4	14.038
9	8 hrs	0.102	64.3	-70.5	143.344
10	10 hrs	2.72	51.6	-84.4	5.118

According to Table 4.8, untreated LDX 2101 DSS has low polarization resistance (Rp = 5.017 $k\Omega.cm^2$). Sputtering process leads to increase in polarization resistance to (Rp = 143.344 $k\Omega.cm^2$) at 8 hrs which has lowest corrosion current density led to lowest corrosion rate.

4.3.24.2 Cyclic Polarization

The cyclic Potentiodynamic polarization of sputtered samples at different times has been investigated also in the Ringer's solution at 37 ±1 °C as illustrated in Figure 4.31. It is cleared that the sputtered sample at 8 hrs had the lowest pitting or break down potential and thus highest pitting and protection potential with an adjacent hysteresis loop where this polarization behavior tends to be resistance to the localized corrosion (Table 4.9). In addition, the lowest value of ΔE is obtained and consequently this sample would have the more resistance to pitting corrosion. Coating of TaN increases resistance to pitting corrosion of LDX by dissolution of nitrogen at the pit site and subsequent formation of ammonium ions NH_4^+ and NO_3^- in the metal interface which increases pH and thus slows down pit growth kinetics [105].

Based on the results from the potentiodynamic and cyclic polarization curves, it is supposing that the sputtered layer at 8 hrs had a strong ability to act as barrier to prevent the localized corrosion attack of many aggressive ions appeared in Ringer's solution during the corrosion test.

Table 4.9 Values of pitting potential for un–sputtered and sputtered samples with TaN at different times from cyclic polarization.

Sample no.	Condition	Ep (mV)
R	untreated	694
11	2 hrs	774
12	4 hrs	784
13	6 hrs	790
14	8 hrs	810
15	10 hrs	773

In light of its high electrochemical stability combined with good mechanical properties, the TaN coating has potential for the surface protection of metallic orthopedic devices. TaN coating could be passivated spontaneously in Ringer's physiological solution and showed a more positive Ecorr and lower i_{corr} .The performance of the Ta-based coatings on LDX 2101 DSS suggests that new medical alloys coated with tantalum nitride will have an excellent performance and a large lifetime for Orthopedic fields [178].

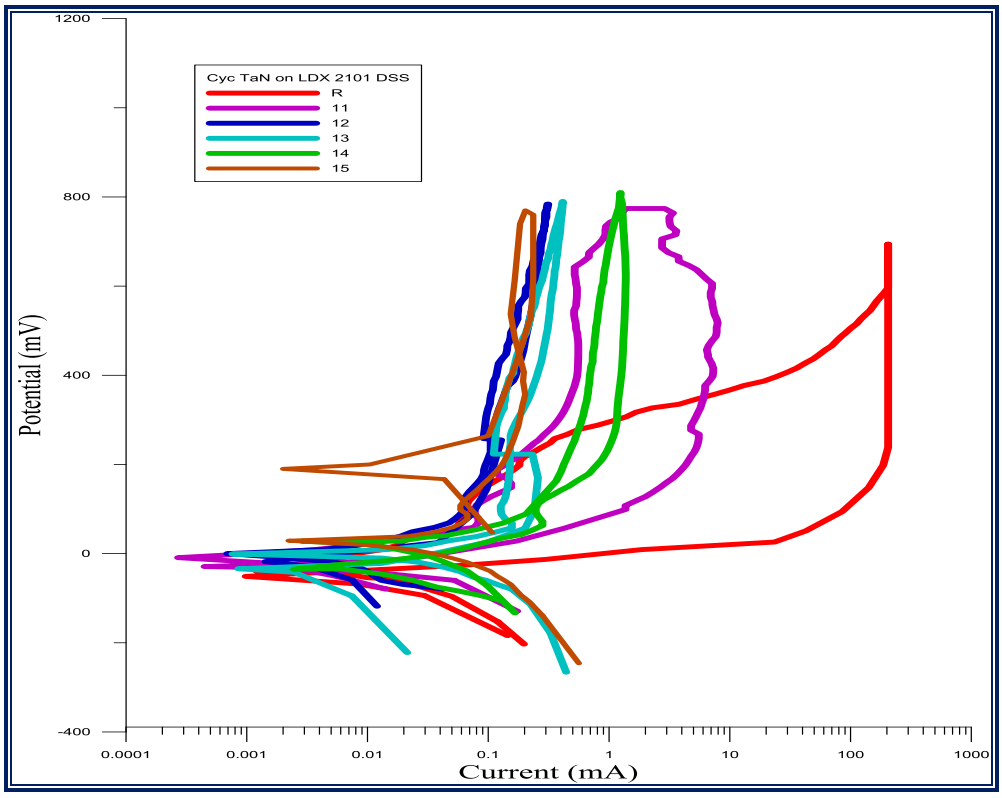

Figure 4.31 Cyclic polarization curves for untreated LDX 2101 DSS and sputtered samples with TaN at different deposition times in Ringer's solution at 37 ±1 °C.

4.4 Analysis and Optimization of Results by Grey Relational Analysis Method

A Grey relational analysis method was performed to optimize the responses. The obtained experimental results were analyzed using Minitab 16 software at a confidence level of 0.5%. Table (4.10) contains the

parameters of surface modifications techniques that used (surface modifications type (S.M), voltage (V), current (I) and time (t)) and the experimental results of responses (micro hardness (Hv), thickness (th), surface roughness (Ra) and corrosion rate (CR)). The steps used for multi-parametric optimization using the GRA are discussed below [183-187]:

Table 4.10 The parameters of surface modifications techniques that used and the experimental results of responses.

Processes Parameters					Experimental Results			
Exp no	**S.M**	**V**	**I**	**t**	**CR**	**th**	**Hv**	**Ra**
1	1	400	30	5	0.754	97.32	785.04	2.66
2	1	400	30	10	0.057	176.28	934.54	3.02
3	1	400	30	15	3.755	248.7	1196.82	4.38
4	1	400	30	20	5.446	200.06	999.96	6.78
5	1	400	30	25	7.558	113.67	984.16	8.25
6	2	3500	10	2	1.222	454.19	290.96	2.65
7	2	3500	10	4	0.811	784.92	339.2	2.71
8	2	3500	10	6	0.667	867.54	411.48	3.22
9	2	3500	10	8	0.0492	1.03	564.28	3.6
10	2	3500	10	10	1.314	2.07	588.46	6.11
11	3	3500	10	2	1.058	27.44	308.2	3.6
12	3	3500	10	4	0.927	30.92	511.96	4.14
13	3	3500	10	6	0.666	31.43	743.101	5.07
14	3	3500	10	8	0.022	32.48	934.54	8.36
15	3	3500	10	10	0.869	31.83	857.32	7.2

Step 1. Data Pre-Processing

The data is first to be normalized because of avoiding different units and to reduce the variability. It is essentially required since the variation of one data differs from other data. A suitable value is derived from the original value to make the array between (0 to 1). In general, it is a method of converting the original data to a comparable data. If the response is to be minimized, then smaller–the–better (or larger–the–better) characteristics is intended for normalization to scale it into an acceptable range by the following formula:

$$x^*_i(k) = \frac{\max\ x_i(k) - x_i(k)}{\max\ x_i(k) - \min\ x_i(k)} \quad \ldots\ldots\ldots\ldots\ldots\ldots\ldots\ldots (1)$$

$$x_i^*(k) = \frac{X_i(k) - \min X_i(k)}{\max X_i(k) - \min X_i(k)} \quad \ldots\ldots\ldots\ldots\ldots\ldots\ldots\ldots (2)$$

where, $i = 1,\ldots, m;\ k = 1,\ldots,n.$, m is the number of experimental data and n is the number of responses. xi(k) denotes the original sequence, *xi*(k)* denotes the sequence after the data preprocessing, max xi(k) denotes the largest value of xi(k), min xi(k) denotes the smallest value of xi(k), and x is the desired value. Table (4.11) shows The sequences of each performance characteristic after data processing.

Table 4.11 The sequences of each performance characteristic after data processing.

Normalized Sequence			
Ra	**Hv**	**th**	**CR**
0.001751	0.545426	0.888876	0.902866
0.064799	0.710463	0.797752	0.995356
0.302977	1	0.714175	0.504644
0.723292	0.782682	0.770308	0.280255
0.980736	0.76524	0.870007	0
0	0	0.477029	0.840764
0.010508	0.053253	0.095348	0.895303
0.099825	0.133045	0	0.914411
0.166375	0.301724	1	0.996391
0.605954	0.328417	0.9988	0.828556
0.166375	0.019032	0.969521	0.862527
0.260946	0.243967	0.965505	0.87991
0.423818	0.499129	0.964917	0.914544
1	0.710463	0.963705	1
0.796848	0.625218	0.964455	0.887606

Step 2. Grey Relational Coefficient (GRC)

Next step is to calculate grey relational coefficient, ξi(k) from the normalized values by the following formula as follows:

$$\xi_i(k) = \frac{\Delta_{\min} + \xi \Delta_{\max}}{\Delta_{oi}(k) + \xi \Delta_{\max}} \quad \ldots\ldots\ldots\ldots\ldots\ldots\ldots (3)$$

where, Δ0i is the deviation sequence of the reference sequence and the comparability sequence and

$$\Delta_{0i} = \left\| x_0(k) - x_i(k \right\| \quad \ldots\ldots\ldots\ldots\ldots\ldots\ldots (4)$$

where x_0 *(k)* implies the reference sequence and xi (k) termed as comparability sequence. Δ_{min} and Δ_{max} are the minimum and maximum values of the absolute differences (Δ_{0i}) of all comparing sequences. ζ is distinguishing or identification coefficient and the range is between (0 to 1). Usually, the value of ζ is taken as 0.5. The GRC for each experiment is shown in Table (4.12).

Table 4.12 Grey Relational Coefficient (GRC).

Grey Relation Coefficient (GRC)			
Ra	**Hv**	**th**	**CR**
0.333723	0.523794	0.818165	0.837333
0.348383	0.633283	0.711999	0.990797
0.417703	1	0.636274	0.502333
0.643743	0.697041	0.685221	0.409922
0.962901	0.680494	0.79366	0.333333
0.333333	0.333333	0.488772	0.758454
0.335685	0.345603	0.35596	0.82686
0.357098	0.365776	0.333333	0.853841
0.374918	0.417266	1	0.992833
0.559256	0.426773	0.997605	0.744664
0.374918	0.337617	0.942545	0.784346
0.403534	0.398079	0.935463	0.806334
0.464605	0.499565	0.934434	0.854034
1	0.633283	0.932323	1
0.711083	0.571571	0.933629	0.816468

Step 3. Grey Relational Grade (GRG)

To find out the grey relational grade (GRG) as follows:

$$\gamma_i = \frac{1}{n}\sum_{k=1}^{n} \xi_i(k) \quad \text{..... (5)}$$

where, γ_i is the required grey relational grade for ith experiment and n = number of response characteristics. The grey relational grade represents the level of correlation between the reference sequence and the comparability sequence and is the overall representative of all the quality characteristics. Thus the multi-response optimization problem is converted into single response optimization problem through grey relational analysis (Table 4.13).

Table 4.13 Grey relational grade and its order in the optimization.

Exp no	GRG	Rank
1	0.628254	10
2	0.671115	7
3	0.639078	8
4	0.608982	12
5	0.692597	4
6	0.478473	13
7	0.466027	15
8	0.477512	14
9	0.696254	3
10	0.682075	6
11	0.609857	11
12	0.635852	9
13	0.68816	5
14	0.891401	1
15	0.758188	2

Step 4. Optimization of process parameters

Grey relational analysis method used to obtain on the optimal alloy (the best experiment). Then an optimal level of process parameters is determined using higher grey relational grade that indicates the better product quality. To obtain this, average grade values for each level of process parameter is to be find out which can be shown as mean response

table. From, mean response table, higher values of average grade values are chosen as optimal parametric combination for multi-responses.

Figure 4.32 shows the influence of the surface modifications parameters on the responses through the main effect plots. The figures indicate that the parameters (V, I, and SM) have the lowest effect on the responses (Vickers hardness Hv, thickness th, surface roughness Ra and corrosion rate CR), while the time of surface modifications have the essential influence on the responses. The results of optimization and mechanical, surface and corrosion tests showed that the optimal parameters of surface modifications techniques are experimental no.14, where surface of sample modified using tantalum nitride sputtering technique with time (8 hrs), V (3500 v) and I (10 mA).

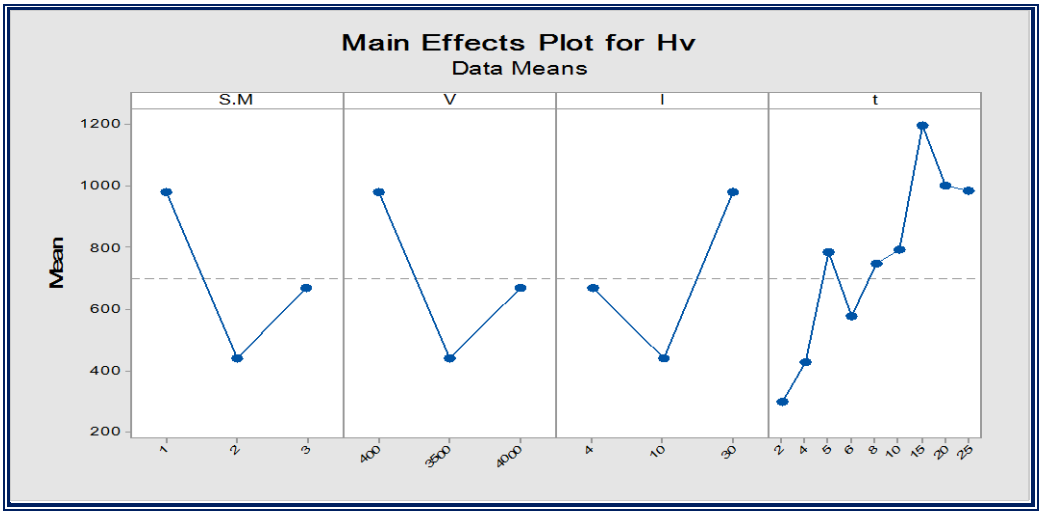

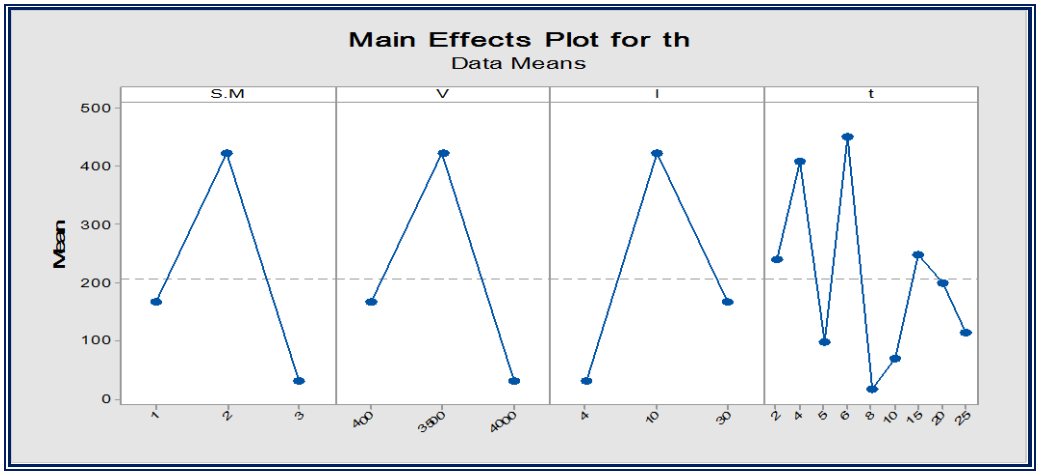

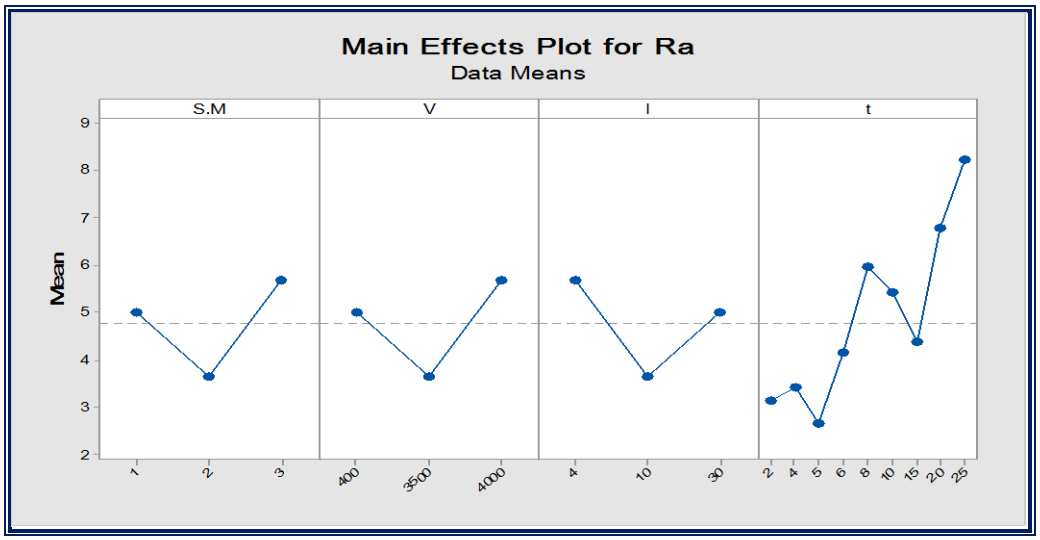

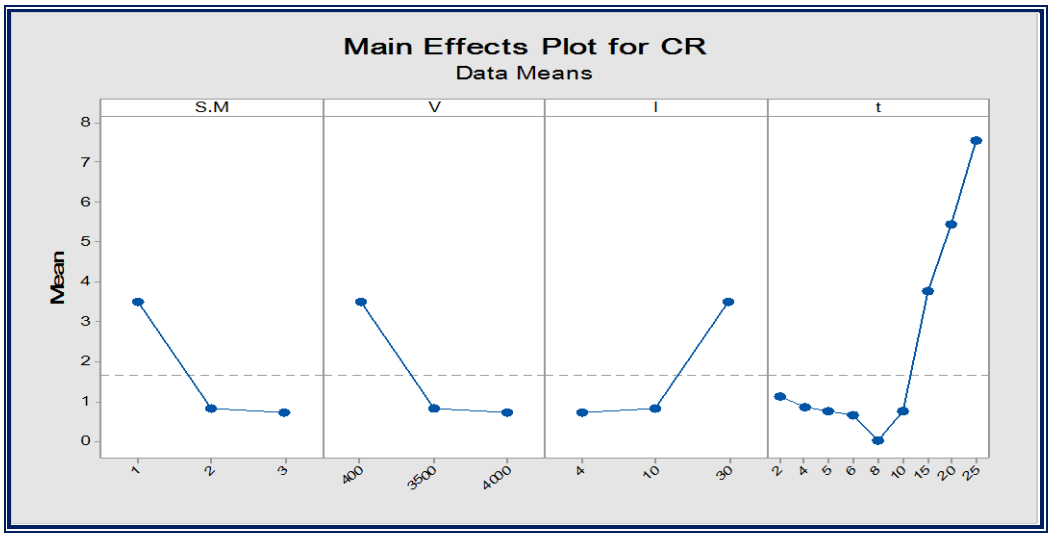

Figure 4.32. Effect of the surface modifications process parameters on (a) Vickers Hardness, (b) thickness (c) surface roughness (d) corrosion rate.

Chapter Five

Conclusions and Recommendations

5.1 Conclusions

In the current study, the plasma nitriding and reactive sputtering technique has been used to modify the surface of LDX 2101 DSS successfully by deposition a surface layer for biomedical applications. In view of the results, the following conclusions can be offered:

5.1.1 Plasma Nitriding

1. The average micro-hardness of the nitrided samples is higher than the hardness of untreated samples because of the existence of an expanded austenite phase.
2. SEM and FESEM results display a dense structure with an increase in the thickness of the nitrided layer up to 15 hrs, then decrease due to coarse particles and form a CrN phase.
3. The morphology of the nitrided layer is homogenous and crack-free when nitriding, with the optimum time at 10 hrs.
4. The XRD analysis shows a high degree of crystallinity in the crystal structure of the nitrided layer and contains expanded austenite phase.
5. The potentiodynamic and cyclic polarization results demonstrate that the plasma nitriding method on LDx 2101 DSS at 10 hrs has the lowest corrosion current density value (0.057 $\mu A/cm^2$) and highest corrosion resistance, and an improvement in the pitting corrosion resistance when immersed in the Ringer's solution.

5.1.2 Tantalum Pentoxide Deposition by Plasma Reactive Sputtering

1. The sputtered samples with Tantalum oxide have an average micro-hardness higher than the hardness of untreated samples due to the presence of an oxide layer.
2. SEM and FESEM results display a regular structure with an increase in the thickness of the deposited sputtered layer with increasing sputtering time.
3. The morphology of sputtered coatings is homogenous and defect-free when coated, with the optimum time at 8 hrs.
4. The XRD analysis shows a high degree of crystallinity and contains Ta_2O_5 phase in the crystal structure of the deposited layer.
5. The potentiodynamic polarization results demonstrate that the reactive sputtering with Ta_2O_5 method on LDX 2101 DSS at 8 hrs has the lowest corrosion current density (0.0492 $\mu A/cm^2$) and the highest corrosion resistance. In addition, the cyclic polarization results state that the coating at 8 hrs shows an improvement in the pitting corrosion resistance when immersed in the Ringer's solution.

5.1.3 Tantalum Nitride Deposition by Plasma Reactive Sputtering

1. The average micro-hardness of the sputtered samples with Tantalum nitride is higher than the hardness of unmodified samples due to the presence of a nitride layer on the surface. When the sputtering time exceeds 8 hours, the increase in hardness decreases.
2. The XRD analysis shows a tantalum nitride phase and a high degree of crystallinity in the crystal structure of the sputtered layer.
3. The coating morphology is homogenous and crack-free when coating, with the optimum time at 8 hrs.
4. The potentiodynamic polarization results demonstrate that the reactive sputtering with the TaN method on LDX 2101 DSS at 8 hrs has the lowest corrosion current density value (0.022 μA/cm2). In addition, the cyclic

polarization results state that the coating at 8 hrs shows an improvement in the pitting corrosion resistance when immersed in the Ringer's solution.

5. AFM topography shows spherical particles in a dense and homogenous film for the nitrided and sputtered samples. The roughness of the modified layer increases with increasing surface modification time.

6. The results The results of antibacterial analysis have confirmed that the plasma nitrided layer and the plasma sputtered coating reveal good antibacterial activity against gram negative E.coli. This antibacterial activity increases when surface treatment time increases. That makes these coatings safe and they can be used for orthopedic implant applications.

7. Adhesion strength results for modified samples compared with non-modified samples appear to be good adhesive for the nitrided layer and sputtered deposited layers with Ta_2O_5 and TaN.

8. Grey relational analysis method (GRA) results show the optimal surface modification parameters were obtained as experiment no. 14, which contains the following conditions: surface modification type is deposition of Tantalum Nitride by sputtering technique at time (8 hrs), V (3500 v) and I (10 mA).

9. The Minitab 17 software results indicate that the parameters (V, I, and SM) have the lowest effect on (Vickers hardness Hv, thickness th, surface roughness Ra, and corrosion rate CR), while the time of surface modifications has the essential influence.

5.2 Suggestions for Future Work

Based on the aforementioned results and conclusions, it is recommended that:

a. The effect of using alternating techniques, such as spray process, instead of plasma nitriding and plasma reactive sputtering on LDX 2101 DSS can be studied.

b. Study deposition of another coating biomaterial instead of Ta_2O_5 and TaN, such as ZnO, TiO_2 and Al_2O_3.

c. The effect of using alternating nitriding and sputtering parameters, such as temperatures and power, on LDX 2101 DSS can be studied.

d. The bioactivity, wettability, and metal ion release behavior of the nitrided and sputtered coated DSS for orthopedic applications may be investigated.

e. The Electrophoretic Deposition coating of HAp nanocomposite on Lean Duplex Stainless Steel for biomedical applications is to be further studied.

f. The effect of laser surface treatment on the morphology and corrosion resistance of 2101 Lean Duplex Stainless Steel may be scrutinized.

g. Using duplex layer (layer-by-layer) coating for nitriding and sputtering nanocomposite to enhance the resistance to pitting corrosion.

h. The tribo-corrosion behavior of modified LDX 2101 DSS with nitrided and sputtered deposited layers must be further pondered scientifically and experimentally.

References

[1] S. Bose and A. Bandyopadhyay, "Introduction to Biomaterials", *Characterization of Biomaterials, Elsevier*, 2013.

[2] U. Jammalamadaka and K. Tappa, "Recent advances in biomaterials for 3D printing and tissue engineering," *Journal of Functional Biomaterials*, vol. 9, no. 1, 2018.

[3] G. A. dos Santos, "The Importance of Metallic Materials as Biomaterials," *Advances in Tissue Engineering and Regenerative Medicine*, vol. 3, no. 1, 2017.

[4] W. Khan, E. Muntimadugu, M. Jaffe, and A. J. Domb, "Imlpantable Medical Devices," *Focal Controlled Drug Delivery*, pp. 33–59, 2014.

[5] Hendra Hermawan, Dadan Ramdan and Joy R. P. Djuansjah, "Metals for Biomedical Applications," *Intech*, vol. i, no. tourism, p. 13, 2016.

[6] Outokumpu, "Handbook of Stainless Steel," pp. 1–89, 2013.

[7] B. Alexander, "What's in Your Stainless Steel?," *EVAPCO*, 2019.

[8] Atlas Steels, "The Atlas Steels Technical Handbook of Stainless Steels," no. August, 2013.

[9] I. Baker, "Stainless Steel," *Fifty materials that make the world*, pp. 1–271, 2018.

[10] S. Arango Santander and C. M. Luna Ossa, "Stainless Steel: Material Facts for the Orthodontic Practitioner," *Revista Nacional de Odontología*, vol. 11, no. 20, 2015.

[11] International Stainless Steel Forum, "The Stainless Steel Family," *WWW.Worldstainless.Org*, vol. 32, no. 0, pp. 1–5, 2013.

[12] Aalco, "Stainless Steel Stainless Steel," *Carbon*, 2013.

[13] D. S. D. Kahar, "Duplex Stainless Steels-An overview," *International Journal of Engineering Research and Application,* vol. 07, no. 04, pp. 27–36, 2017.

[14] B. Alwin Mertens, S. Martinez De La Puente, and M. Doms, "Physical metallurgy of duplex steel and the issues for thick castings DUPLEX & CASTING," pp. 29–31, 2013.

[15] J. Chater, “Duplex stainless steels,” *Stainless Steel World, Springs*, vol. 41, no. 5, pp. 59–63, 2012.

[16] J. Charles, “Duplex families and applications : a review Part 1: From Duplex Pioneers up to 1991,” *Stainless Steel World*, *no. August,* pp. 1–5, 2015.

[17] V. Shamanth, K. S. Ravishankar, and K. Hemanth, “Duplex Stainless Steels: Effect of Reversion Heat Treatment,” *Stainless Steels and Alloy*, 2019.

[18] J. Charles, “Duplex families and applications : A review Part 2 : From 1991 to nowadays,” *Stainless Steel World*, pp. 67–70, 2015.

[19] J. Charles, “Duplex families and applications : a review Part 3:The lean duplex grades,” *Stainless Steel World,* pp. 1–4, 2015.

[20] TMR Stainless, "Practical Guidelines for the Fabrication of Duplex Stainless Steels", *International Molybdenum Association (IMOA)*, 2014.

[21] The Nickel Institute, “Stainless steels and specialty alloys for pulp, and biomass conversion: a practical guide for mill engineers,” 2nd, pp. 1–144, 2017.

[22] M. Knyazeva and M. Pohl, “Duplex Steels: Part I: Genesis, Formation, Structure,” *Metallography, Microstructure, and Analysis*, vol. 2, no. 2, pp. 113–121, 2013.

[23] R. Francis and G. Byrne, “Duplex Stainless Steels — Alloys for the 21st Century,” *Metals (Basel).*, pp. 1–23, 2021.

[24] “Specification Sheet : Alloy LDX 2101,” *Sandmeyer Steel Company*, vol. 2101, 2014.

[25] Paola Bassani, Marco Breda, Katya Brunelli, Istvan Mészáros, Francesca Passaretti, Michela Zanellato and Irene Calliari, “Characterization of a cold-rolled 2101 lean duplex stainless steel,” *Microscopy And Microanalysis*, vol. 19, no. 4, pp. 988–995, 2013.

[26] J. Chater, “Slowly but surely , duplex continues to penetrate more products,” *Stainless Steel World*, pp. 33–36, 2011.

[27] ISSF International Stainless Steel Forum, “Duplex Stainless Steels,” 2019.

[28] API 938C, “Use of duplex stainless steels in the oil refining industry,”

Second edition, American Petroleum Institute, no. April, p. 44, 2011.

[29] Aalco, "Stainless Steel LDX 2101," *Carbon*, 2018.

[30] D. D. Kiradzhiyska and R. D. Mantcheva, "Overview of Biocompatible Materials and Their Use in Medicine," *Folia medica*, vol. 61, no. 1. pp. 34–40, 2019.

[31] Narges Shayesteh Moghaddam, Mohsen Taheri Andani1, Amirhesam Amerinatanzi, Christoph Haberland, Scott Huff, Michael Miller, Mohammad Elahinia, David Dean, "Metals for bone implants: safety, design, and efficacy," *Biomanufacturing Rev.*, vol. 1, no. 1, pp. 1–16, 2016.

[32] Silvio José Gobbi, Gustavo Reinke, Vagner João Gobbi, Ynglid Rocha, Thiago Primo Sousa, Maycol Moreira Coutinho, "Biomaterial : Concepts and Basics Properties Biomaterial : Concepts and Basics Properties," *European International Journal of Science and Technology,* vol. 9, no. March, pp. 23–42, 2020.

[33] Silvio José Gobbi, Vagner João Gobbi and Ynglid Rocha, "Requirements for Selection/Development of a Biomaterial," *Biomedical Journal of Scientific Technical Research.*, vol. 14, no. 3, pp. 1–6, 2019.

[34] S. S. M. Tavares, J. M. Pardal, M. R. Da Silva, and C. A. S. De Oliveira, "Martensitic transformation induced by cold deformation of lean duplex stainless steel uns S32304," *Materials Research,* vol. 17, no. 2, pp. 381–385, 2014.

[35] W. Jin and P. K. Chu, "Orthopedic implants," in *Encyclopedia of Biomedical Engineering*, vol. 1–3, *Elsevier Inc*, 2019, pp. 425–439.

[36] R.I.M. Asri, W.S.W. Harun, M. Samykano, N.A.C. Lah, S.A.C. Ghani, F. Tarlochan, M.R. Raza, "Corrosion and surface modification on biocompatible metals: A review," *Materials Science and Engineering C*, vol. 77, pp. 1261–1274, 2017.

[37] M. Talha, Y. Ma, P. Kumar, Y. Lin, and A. Singh, "Role of protein adsorption in the bio corrosion of metallic implants – A review," *Colloids and Surfaces B: Biointerfaces*, vol. 176, *Elsevier*, pp. 494–506, 2019.

[38] R. B. Heimann, "Structure, properties, and biomedical performance of

osteoconductive bioceramic coatings," *Surface & Coatings Technology*, vol. 233, pp. 27–38, 2013.

[39] L. Rony, R. Lancigu, and L. Hubert, "Intraosseous metal implants in orthopedics: A review," *Morphologie*, vol. 102, no. 339. *Elsevier Masson SAS*, pp. 231–242, 2018.

[40] Mónica Echeverry-Rendón, Oscar Galvis, David Quintero Girald iménez-Piquéo, Juan Pavón, José Luis López-Lacomba, Emilio, "Osseointegration improvement by plasma electrolytic oxidation of modified titanium alloys surfaces," *Journal of Materials Science:Materials in Medicine*, vol. 26, no. 2, pp. 1–18, 2015.

[41] A. Parsapour, S. N. Khorasani, and M. H. Fathi, "Effect of Surface Treatment and Metallic Coating on Corrosion Behavior and Biocompatibility of Surgical 316L Stainless Steel Implant," *Journal of Materials Science Technology.*, vol. 28, no. 2, pp. 125–131, 2012.

[42] T. Hanawa, "Functionalisation of metallic surfaces for biomedical applications", *Surface Coating and Modification of Metallic Biomaterials, Elsevier Ltd*, 2015.

[43] S. Ghosh and S. Abanteriba, "Status of surface modification techniques for artificial hip implants," *Science and Technology of Advanced Materials*, vol. 17, no. 1, pp. 715–735, 2016.

[44] N. C. Verissimo, S. Chung, and T. J. Webster, "New nanoscale surface modifications of metallic biomaterials," *Surface Coating and Modification of Metallic Biomaterials*, pp. 249–273, 2015.

[45] M. Niinomi, "Design and development of metallic biomaterials with biological and mechanical biocompatibility," *Journal of Biomedical Materials Research - Part A*, vol. 107, no. 5, pp. 944–954, 2019.

[46] W. Murphy, J. Black, and G. Hastings, "Metallic Biomaterials: Introduction," *Handbook of Biomaterial Properties. Second Edition.*, pp. 1–676, 2016.

[47] M. Jäger, "Surface modifications of implants. Part 2: Clinical application," *Orthopade*, vol. 47, no. 5, pp. 445–458, 2018.

[48] Anna Sobiepanek, Joanna Baran, Małgorzata Milner-Krawczyk and

Tomasz Kobiela, “Different Types of Surface modification used for Improving the Adhesion and Interactions of Skin Cells,” *Open Access Journal of Biomedical Science*, vol. 2, no. 1, pp. 275–278, 2020.

[49] A. Nouri and C. Wen, "Surface Coating and Modification of Metallic Biomaterials"*, Woodhead Publishing Series in Biomaterials: Number 94, Elsevier Ltd*, 2015.

[50] G. Mani, "Surface properties and characterization of metallic biomaterials", *Surface Coating and Modification of Metallic Biomaterials*, *Elsevier Ltd*, 2015.

[51] M. Z. Ibrahim, A. A. D. Sarhan, F. Yusuf, and M. Hamdi, “Biomedical materials and techniques to improve the tribological, mechanical and biomedical properties of orthopedic implants – A review article,” *Journal of Alloys and Compounds*, vol. 714, pp. 636–667, 2017.

[52] Harjit Singh, Sunpreet Singh and Chander Prakash, "Current Trends in Biomaterials and Bio-manufacturing", *Biomanufacturing*, no. February. 2019.

[53] G. Agrawal, C., Ong, J., Appleford, M., & Mani, “Introduction to Biomaterials: Basic Theory with Engineering Applications (Cambridge Texts in Biomedical Engineering),” 2013.

[54] Z. Y. Qiu, C. Chen, X. M. Wang, and I. S. Lee, “Advances in the surface modification techniques of bone-related implants for last 10 years,” *Regenerative Biomaterials*, vol. 1, no. 1. pp. 67–79, 2014.

[55] J. Li and X. Liu, “Chemical surface modification of metallic biomaterials,” *Surface Coating and Modification of Metallic Biomaterials*, vol. 1, no. c, pp. 159–183, 2015.

[56] Q. Y. Liang Li, "Advanced Coating Materials", *Scrivener Publishing*, 2019.

[57] A. H. C. Poulsson, D. Eglin, and R. Geoff Richards, “Surface Modification Techniques of PEEK, Including Plasma Surface Treatment,” in *PEEK Biomaterials Handbook*, 2nd ed., Elsevier Inc., 2019.

[58] A. Dehghanghadikolaei and B. Fotovvati, “Coating techniques for functional enhancement of metal implants for bone replacement: A

review," *Materials (Basel).*, vol. 12, no. 11, 2019.

[59] B. Fotovvati, N. Namdari, and A. Dehghanghadikolaei, "On Coating Techniques for Surface Protection: A Review," *Journal of Manufacturing and Materials Processing*, vol. 3, no. 1, p. 28, 2019.

[60] A. Mahalwar, "Surface Modification: Approaches and Utilities," *Current Applied Polymer Science*, vol. 3, no. 2, pp. 98–111, 2019.

[61] J. A. Gan and C. C. Berndt, "Plasma surface modification of metallic biomaterials", *Surface Coating and Modification of Metallic Biomaterials*, 2015.

[62] F. Bottoli, "influence of steel composition and plastic deformation on the surface properties induced by low-temperature thermochemical processing," PhD Thesis, Technical University of Denmark, no. December, 2016.

[63] L. H. Paijan, M. N. Berhan, M. S. Adenan, N. F. M. Yusof, and E. Haruman, "Structural development of expanded austenite on duplex stainless steel by low temperature thermochemical nitriding process," *Advanced Materials Research*, vol. 576, pp. 260–263, 2012.

[64] Nsikan Dan, Patthi Hussain and Saeid Kakooei, "Nitriding of Duplex Stainless Steel for Reduction Corrosion and Wear," *Engineering Applications of Nanotechnology, Topics in Mining, Metallurgy and Materials Engineering,* pp. 1–31, 2017.

[65] G. Maistro, "Low-temperature ion nitriding of austenitic stainless steels", *PhD Thesis, Chalmers University of Technology*, 2018.

[66] R. Djellal, A. Saker, B. Bouzabata, and D. E. Mekki, "Thermal stability and phase decomposition of nitrided layers on 316L and 310 austenitic stainless steels," *Surface & Coatings Technology*, vol. 325, pp. 533–538, 2017.

[67] C. F. Hung, C. Z. Wu, W. F. Lee, K. L. Ou, C. M. Liu, and P. W. Peng, "The Effect of Nitrided Layer on Antibacterial Properties for Biomedical Stainless Steel," *Physics Procedia*, vol. 32, pp. 914–919, 2012.

[68] Yang Li, Shang-Zhou Zhang, Jian-Xun Qiu, Yong-Yong He, Jun-Jie Xiu, Qian-Wen Ye, Zhong-Li Liu, "Effect of Electric Potentials on

Microstructure, Corrosion and Wear Characteristic of the Nitrided Layer Prepared on 2Cr13 Stainless Steel by Plasma Nitriding," *Acta Metallurgica Sinica*, vol. 32, no. 6, pp. 733–745, 2019.

[69] M. T. Umemura, L. B. Varela, C. E. Pinedo, R. C. Cozza, and A. P. Tschiptschin, "Assessment of tribological properties of plasma nitrided 410S ferritic-martensitic stainless steels," *Wear*, vol. 426–427, no. April, pp. 49–58, 2019.

[70] D. Kovács, I. Quintana, and J. Dobránszky, "Effects of Different Variants of Plasma Nitriding on the Properties of the Nitrided Layer," *Journal of Materials Engineering and Performance*, vol. 28, no. 9, pp. 5485–5493, 2019.

[71] S. Koppula, P. Gugulothu, N. Sateesh, and R. Subbiah, "A review on AISI 2205 duplex stainless steel treated with plasma nitriding process," *Materials Today: Proceedings*, no. xxxx, 2020.

[72] A. P. Tschiptschin, A. S. Nishikawa, L. B. Varela, and C. E. Pinedo, "Thermal stability of expanded austenite formed on a DC plasma nitrided 316L austenitic stainless steel," *Thin Solid Films*, vol. 644, pp. 156–165, 2017.

[73] S. Zhao, L. Wang, J. Xu, and Y. Shan, "Surface modification of SS2205 duplex stainless steel by plasma nitriding at anodic potential," *Advanced Materials Research*, vol. 881–883, pp. 1263–1267, 2014.

[74] Yue Teng, Yuan-Yuan Guo, Min Zhang, Yong-Jie Yang, Zhen Huang, Yan-Wen Zhou, Fa-Yu Wu, Ying-Shuang Liang, "Effect of Cr/CrN x transition layer on mechanical properties of CrN coatings deposited on plasma nitrided austenitic stainless steel," *Surface & Coatings Technology*, vol. 367, no. March, pp. 100–107, 2019.

[75] A. P. Tschiptschin, L. B. Varela, C. E. Pinedo, X. Y. Li, and H. Dong, "Development and microstructure characterization of single and duplex nitriding of UNS S31803 duplex stainless steel," *Surface & Coatings Technology*, vol. 327, pp. 83–92, 2017.

[76] J. J. Jasinski, T. Fraczek, L. Kurpaska, M. Lubas, and M. Sitarz, "Investigation of nitrogen transport in active screen plasma nitriding

processes – Uphill diffusion effect," *Journal of Molecular Structure*, vol. 1164, pp. 37–44, 2018.

[77] H. Aghajani and S. Behrangi, "Plasma nitriding of steels", *Topics in Mining, Metallurgy and Materials Engineering*, 2017.

[78] M. Olzon-Dionysio, D. Olzon-Dionysio, M. Campos, W. T. Shigeyosi, S. D. de Souza, and S. de Souza, "Corrosion resistance of AISI 316L plasma nitrided at different temperatures and times," *Hyperfine Interactions*, vol. 240, no. 1, pp. 18–23, 2019.

[79] Elieser de Araújo Junior, Rafael Marinho Bandeira, Marcos Dorigão Manfrinato, Jéferson Aparecido Moreto, Roger Borges, Sandra dos Santos Vales, Paulo Atsushi Suzuki, Luciana Sgarbi Rossino, "Effect of ionic plasma nitriding process on the corrosion and micro-abrasive wear behavior of AISI 316L austenitic and AISI 470 super-ferritic stainless steels," *Journal of Materials Research and Technol*ogy, vol. 8, no. 2, pp. 2180–2191, 2019.

[80] A. M. Gatey, S. S. Hosmani, C. A. Figueroa, S. B. Arya, and R. P. Singh, "Role of surface mechanical attrition treatment and chemical etching on plasma nitriding behavior of AISI 304L steel," *Surface & Coatings Technology*, vol. 304, pp. 413–424, 2016.

[81] M. A. Maleque, P. H. Lailatul, A. A. Fathaen, K. Norinsan, and J. Haider, "Nitride alloy layer formation of duplex stainless steel using nitriding process," *IOP Conference Series: Materials Science and Engineering*, vol. 290, no. 1, pp. 0–6, 2018.

[82] P. Chhabra, "Surface Engineering and Coating Processes," *Thesis of Master of Technology, SSET Patiala Punjab INDIA*, pp. 1–66, 2016.

[83] M. Mozetič, "Surface modification to improve properties of materials," *Materials (Basel).*, vol. 12, no. 3, 2019.

[84] A Zykova, V Safonov, A Goltsev, T Dubrava, I Rossokha, N Donkov, S Yakovin, D Kolesnikov, I Goncharov and V Georgieva, "Surface modification of tantalum pentoxide coatings deposited by magnetron sputtering and correlation with cell adhesion and proliferation in in vitro tests," *Journal of Physics: Conference Series*, vol. 700, no. 1, 2016.

[85] H. R. Bakhsheshi-Rad, A. F. Ismail, M. Aziz, Z. Hadisi, M. Omidi, and X. Chen, “Antibacterial activity and corrosion resistance of Ta_2O_5 thin film and electrospun PCL/MgO-Ag nanofiber coatings on biodegradable Mg alloy implants,” *Ceramics International*, vol. 45, no. 9, pp. 11883–11892, 2019.

[86] B. Rahmati, A. A. D. Sarhan, W. J. Basirun, and W. A. B. W. Abas, “Ceramic tantalum oxide thin film coating to enhance the corrosion and wear characteristics of Ti-6Al-4V alloy,” *Journal of Alloys and Compounds*, vol. 676, pp. 369–376, 2016.

[87] Weihong Jin, Guomin Wang, Zhengjie Lin, Hongqing Feng, Wan Li, Xiang Peng, Abdul Mateen Qasim, Paul K. Chu, “Corrosion resistance and cytocompatibility of tantalum-surface-functionalized biomedical ZK60 Mg alloy,” *Corrosion Science*, vol. 114, pp. 45–56, 2017.

[88] P. Mandracci, F. Mussano, P. Rivolo, and S. Carossa, “Surface treatments and functional coatings for biocompatibility improvement and bacterial adhesion reduction in dental implantology,” *Coatings*, vol. 6, no. 1. 2016.

[89] Y. Oshida and Y. Guven, "Biocompatible coatings for metallic biomaterials", *Surface Coating and Modification of Metallic Biomaterials , Elsevier Ltd*, 2015.

[90] A. Bekmurzayeva, W. J. Duncanson, H. S. Azevedo, and D. Kanayeva, “Surface modification of stainless steel for biomedical applications: Revisiting a century-old material,” *Materials Science & Engineering C*, vol. 93, pp. 1073–1089, 2018.

[91] X. Li, W. Dou, L. Tian, and H. Dong, “Combating the tribo-corrosion of LDX2404 lean duplex stainless steel by low temperature plasma nitriding,” *Lubricants*, vol. 6, no. 4, 2018.

[92] G. Pintaude, A. C. Rovani, J. C. K. das Neves, L. E. Lagoeiro, X. Li, and H. S. Dong, “Wear and Corrosion Resistances of Active Screen Plasma-Nitrided Duplex Stainless Steels,” *Journal of Materials Engineering and Performance*, vol. 28, no. 6, pp. 3673–3682, 2019.

[93] M. Breda, M. Pellizzari, and M. Frigo, “σ-Phase in lean duplex stainless steel sheets,” *Acta Metall. Sin. (English Lett.*, vol. 28, no. 3, pp. 331–337,

2015.

[94] B. G. Pound, “Passive films on metallic biomaterials under simulated physiological conditions,” *Journal of Biomedical Materials Research A*, vol. 102, no. 5, pp. 1595–1604, 2014.

[95] Z. H. Feng, J. Y. Li, and Y. De Wang, “The Microstructure Evolution of Lean Duplex Stainless Steel 2101,” *steel research int.*, vol. 88, no. 12, pp. 1–10, 2017.

[96] E. Haruman, Y. Sun, and M. S. Adenan, “A comparative study of the tribocorrosion behaviour of low temperature nitrided austenitic and duplex stainless steels in NaCl solution,” *Tribology International,* vol. 151, no. January, p. 106412, 2020.

[97] Shucai Zhang, Huabing Li, Zhouhua Jiang, Binbin Zhang, Zhixing Li, Jingxi Wu, Sipeng Fan, Hao Feng, Hongchun Zhu “Effects of Cr and Mo on precipitation behavior and associated intergranular corrosion susceptibility of superaustenitic stainless steel S32654,” *Materials Characterization*, vol. 152, no. April, pp. 141–150, 2019.

[98] Hanme Yoon, Heon-Young Ha, Tae-Ho Lee, Sung-Dae Kim, Jae Hoon Jang, Joonoh Moon and Namhyun Kang, “Pitting corrosion resistance and repassivation behavior of c-bearing duplex stainless steel,” *Metals (Basel)*, vol. 9, 2019.

[99] M. Pan, X. Zhang, P. Chen, X. Bin Su, and R. D. K. Misra, “The effect of chemical composition and annealing condition on the microstructure and tensile properties of a resource-saving duplex stainless steel,” *Materials Science & Engineering A*, vol. 788, p. 139540, 2020.

[100] M. S. F. De Lima, S. M. De Carvalho, V. Teleginski, and M. Pariona, “Mechanical and corrosion properties of a duplex steel welded using Micro-Arc or Laser,” *Materials Research*, vol. 18, no. 4, pp. 723–731, 2015.

[101] L. Esteves, M. Cardoso, and V. de Freitas Cunha Lins, “Corrosion behavior of duplex and lean duplex stainless steels in pulp mill,” *Mater. Res.*, vol. 21, no. 1, 2018.

[102] L. Esteves, M. M. A. M. Schvartzman, W. R. Da Costa Campos, and V. F.

C. Lins, “Corrosion behavior of duplex stainless steel in industrial white liquor,” *Corrosion*, vol. 74, no. 5, pp. 543–550, 2018.

[103] A. A. Kazakov, A. I. Zhitenev, A. S. Fedorov, and O. V. Fomina, “Development of duplex stainless steels Compositions,” *CIS Iron and Steel Review*, vol. 18, pp. 20–26, 2019.

[104] M. Bernås, I. Westermann, R. Johnsen, C. Lauritsen, and M. Iannuzzi, “Effect of microstructure on the corrosion resistance of duplex stainless steels: Materials performance maps,” *NACE - International Corrosion Conference Series*, vol. 8, no. May, pp. 5476–5490, 2017.

[105] N. Mitsuo, T. Narushima, and M. Nakai, "Advances in Metallic Biomaterials: Tissues, Materials and Biological Reactions", *Springer Series in Biomaterials Science and Engineering, Vol.3*, 2015.

[106] H. Y. Ha, M. H. Jang, T. H. Lee, and J. Moon, “Interpretation of the relation between ferrite fraction and pitting corrosion resistance of commercial 2205 duplex stainless steel,” *Corrosion Science*, vol. 89, no. C, pp. 154–162, 2014.

[107] E. Bettini, U. Kivisäkk, C. Leygraf, and J. Pan, “Study of corrosion behavior of a 22% Cr duplex stainless steel: Influence of nano-sized chromium nitrides and exposure temperature,” *Electrochimica Acta,* vol. 113, pp. 280–289, 2013.

[108] S. Aribo, A. Neville, and X. Hu, “Pitting behaviour of lean Duplex stainless steels in marine and oilfield environments,” *the Society of Petroleum Engineers - SPE*, no. May 2016, pp. 95–102, 2012.

[109] C. Örnek, F. Léonard, S. A. McDonald, A. Prajapati, P. J. Withers, and D. L. Engelberg, “Time-dependent in situ measurement of atmospheric corrosion rates of duplex stainless steel wires,” *npj nature partner journals/Materials Degradation*, vol. 2, no. 1, pp. 0–15, 2018.

[110] F. Zanotto, V. Grassi, A. Balbo, F. Zucchi, and C. Monticelli, “Investigation on the corrosion behavior of lean duplex stainless steel 2404 after aging within the 650-850 °C temperature range,” *Metals (Basel).*, vol. 9, no. 5, 2019.

[111] F. Zanotto, V. Grassi, A. Balbo, C. Monticelli, and F. Zucchi, “Stress-

corrosion cracking behaviour of lean-duplex stainless steels in chloride/thiosulphate environments," *Metals (Basel).*, vol. 8, no. 4, pp. 1–16, 2018.

[112] Yadi Hu, Yuping Li, Yan He, JianWang, Xinglong Liu, Yong Zhang and Peide Han, "Effects of micro-sized ferrite and austenite grains on the pitting corrosion behavior of lean duplex stainless steel 2101," *Metals (Basel).*, vol. 7, no. 5, 2017.

[113] Z. Zhang, D. Han, Y. Jiang, C. Shi, and J. Li, "Microstructural evolution and pitting resistance of annealed lean duplex stainless steel UNS S32304," *Nuclear Engineering and Design*, vol. 243, pp. 56–62, 2012.

[114] S. Aribo, "Corrosion and Erosion-Corrosion Behaviour of Lean Duplex Stainless Steels in Marine and Oilfield Environments," *PhD Thesis, The University of Leeds,* 2014.

[115] Gulsen Akdogan and Mohammad Ghaith Almasry, "Corrosion Residue Debris Left by Implant Materials to the Patient's Body," *American Journal of Biomedical Science & Research,* vol. 6, no. 3, pp. 176–178, 2019.

[116] N. Mazinanian, "Metal release and corrosion resistance of different stainless steel grades in simulated food contact", *PhD Thesis, KTH Royal Institute of Technology*, 2016.

[117] E. Győri, I. Fábián, and I. Lázár, "Effect of the Chemical Composition of Simulated Body Fluids on Aerogel-Based Bioactive Composites," *Journal of composites science*, vol. 1, no. 2, p. 15, 2017.

[118] M. A. Farhan Zaludin, Z. A. Zahid Jamal, M. N. Derman, and M. Z. Kasmuin, "Corrosion analysis of hydroxyapatite coated magnesium in simulated body fluid (SBF), phosphate buffered saline (PBS), and Ringer's solution," *Materials Today: Proceedings*, vol. 16, pp. 1686–1691, 2019.

[119] L. N. Wang, A. Shinbine, and J. L. Luo, "Electrochemical behavior of CoCrMo implant in Ringer's solution," *Surface and Interface Analysis*, vol. 45, no. 9, pp. 1323–1328, 2013.

[120] A. Gilewicz, P. Chmielewska, D. Murzynski, E. Dobruchowska, and B. Warcholinski, "Corrosion resistance of CrN and CrCN/CrN coatings deposited using cathodic arc evaporation in Ringer's and Hank's

solutions," *Surface & Coatings Technology*, vol. 299, pp. 7–14, 2016.

[121] W. Huang, Z. Wang, C. Liu, and Y. Yu, "Wear and Electrochemical Corrosion Behavior of Biomedical Ti–25Nb–3Mo–3Zr–2Sn Alloy in Simulated Physiological Solutions," *Journal of Bio- and Tribo-Corrosion*, vol. 1, no. 1, pp. 1–10, 2015.

[122] H. K. Kang, T. M. Chu, P. Dechow, K. Stewart, H. M. Kyung, and S. S. Y. Liu, "Laser-treated stainless steel mini-screw implants: 3D surface roughness, bone-implant contact, and fracture resistance analysis," *The European Journal of Orthodontics*, vol. 38, no. 2, pp. 154–162, 2016.

[123] E. D. Gonzalez, C. R. M. Afonso, and P. A. P. Nascente, "Influence of Nb content on the structure, morphology, nanostructure, and properties of titanium-niobium magnetron sputter deposited coatings for biomedical applications," *Surface & Coatings Technology*, vol. 326, no. November, pp. 424–428, 2017.

[124] V. Meyer-Kobbe, K. Doll, M. Stiesch, R. Schwestka-Polly, and A. Demling, "Comparison of intraoral biofilm reduction on silver-coated and silver ion-implanted stainless steel bracket material: Biofilm reduction on silver ion-implanted bracket material," *Journal of Orofacial Orthopedics*, vol. 80, no. 1, pp. 32–43, 2019.

[125] A. M. Oje, A. A. Ogwu, A. I. Oje, N. Tsendzughul, and S. Ur Rahman, "A comparative study of the corrosion and ion release behaviour of chromium oxide coatings exposed to saline, Ringer's and Hank's physiological solutions," *Corrosion Science*, vol. 167, p. 108533, 2020.

[126] J. Cheng, J. Xu, L. L. Liu, and S. Jiang, "Electrochemical corrosion behavior of Ta2n nanoceramic coating in simulated body fluid," *Materials (Basel).*, vol. 9, no. 9, pp. 1–21, 2016.

[127] A. C. Hee, H. Cao, Y. Zhao, S. S. Jamali, A. Bendavid, and P. J. Martin, "Cytocompatible tantalum films on Ti6Al4V substrate by filtered cathodic vacuum arc deposition," *Bioelectrochemistry*, vol. 122, pp. 32–39, 2018.

[128] G. B. Melnikova, A. S. Petrovskaya, T. A. Kuznetsova, S. A. Chizhik, "Structure of Tantalum and Tantalum Oxide Coatings on Steel and Glass Surfaces," *International Journal of Nanoscience*, vol. 18, no. 3–4, 2019.

[129] H. J. Farhan, R. K. Jassim, and L. Thair, “Deposition of TaN Film on Commercial Pure Titanium Disk by Modified Reactive Plasma Sputtering Technique,” *Indian Journal of Forensic Medicine & Toxicology*, vol. 14, no. 1, pp. 1250–1254, 2020.

[130] J. Alphonsa, V. S. Raja, and S. Mukherjee, “Study of plasma nitriding and nitrocarburizing for higher corrosion resistance and hardness of 2205 duplex stainless steel,” *Corrosion Science*, vol. 100, pp. 121–132, 2015.

[131] A. S. Hammood, L. Thair, and S. H. Ali, “Corrosion Behavior Evaluation in Simulated Body Fluid of a Modified Ti–6Al–4V Alloy by DC Glow Plasma Nitriding,” *Journal of Bio- and Tribo-Corrosion*, vol. 5, no. 4, pp. 1–8, 2019.

[132] A. Biserova-Tahchieva, J. M. Cabrera, and N. Llorca-Isern, “Study of the thermochemical surface treatment effect on the phase precipitation and degradation behaviour of DSS and SDSS,” *Materials (Basel).*, vol. 13, no. 1, 2020.

[133] X. Tao, A. Matthews, and A. Leyland, “On the Nitrogen-Induced Lattice Expansion of a Non-stainless Austenitic Steel, Invar 36®, Under Triode Plasma Nitriding,” *Metallurgical and Materials Transactions A*, vol. 51, no. 1, pp. 436–447, 2020.

[134] M. E. Sotomayor, J. Sanz, A. Cervera, B. Levenfeld, and A. Várez, “Surface modification of a duplex stainless steel for plastic-metal hybrid parts,” *Archives of Materials Science and Engineering*, vol. 72, no. 2, pp. 86–93, 2015.

[135] M. Bobadilla and A. Tschiptschin, “On the nitrogen diffusion in a duplex stainless steel,” *Materials Research.,* vol. 18, no. 2, pp. 390–394, 2015.

[136] R. W. Gregorutti, J. E. Grau, F. Sives, and C. I. Elsner, “Mechanical, electrochemical and magnetic behaviour of duplex stainless steel for biomedical applications,” *Materials Science and Technology (United Kingdom)*, vol. 31, no. 15, pp. 1818–1824, 2015.

[137] A. S. Hammood, A. F. Noor, M. T. Alkhafagy, and I. Calliari, “Effect of Heat Treatment on Corrosion Behavior of Duplex Stainless Steel 2507 in Artificial Saliva,” *Metal Science and Heat Treatment*, vol. 61, no. 1–2, pp.

48–56, 2019.

[138] P. H. Lailatul and M. A. Maleque, “Surface Modification of Duplex Stainless Steel with SiC Preplacement Using TIG Torch Cladding,” *Procedia Engineering*, vol. 184, pp. 737–742, 2017.

[139] A. B. Tahchieva, N. Llorca-Isern, and J. M. Cabrera, “Duplex and superduplex stainless steels: Microstructure and property evolution by surface modification processes,” *Metals (Basel)*, vol. 9, no. 3, 2019.

[140] G. Lakshmi Prasanna, B. Tanya, R. Subbiah, and V. Vinod Kumar, “Effect of nitriding on duplex stainless steel - A review,” *Materials Today: Proceedings*, vol. 26, no. xxxx, pp. 950–955, 2019.

[141] A. S. Hammood, M. S. Naser, and Z. S. Radeef, “Electrophoretic Deposition of Nanocomposite Hydroxyapatite/Titania Coating on 2205 Duplex Stainless Steel Substrate,” *Jom*, vol. 73, no. 2, pp. 524–533, 2021.

[142] F. W. Abdulsada and A. S. Hammood, “Characterization of corrosion and antibacterial resistance of hydroxyapatite/silver nano particles powder on 2507 duplex stainless steel,” *Materials Today: Proceedings*, vol. 42, no. xxxx, pp. 2301–2307, 2021.

[143] Z. hui Feng, J. yuan Li, and Y. de Wang, “Mechanism of hot-rolling crack formation in lean duplex stainless steel 2101,” *International Journal of Minerals, Metallurgy and Materials*, vol. 23, no. 4, pp. 425–433, 2016.

[144] A. Ruiz, K. J. Fuentes-Corona, V. H. López, and C. A. León, “Microstructural and ultrasonic characterization of 2101 lean duplex stainless steel welded joint,” *Applied Acoustics*, vol. 117, pp. 12–19, 2017.

[145] J. Y. Maetz, S. Cazottes, C. Verdu, F. Danoix, and X. Kléber, “Microstructural Evolution in 2101 Lean Duplex Stainless Steel during Low- and Intermediate-Temperature Aging,” *Microsc. Microanal.*, vol. 22, no. 2, pp. 463–473, 2016.

[146] A. A. H. Ameri, J. P. Escobedo-Diaz, M. Z. Quadir, M. Ashraf, and W. Hutchison, “Strain rate effect on the mechanical response of duplex stainless steel,” *AIP Conference Proceedings*, vol. 1979, 2018.

[147] F. Tehovnik, B. Š. Batič, F. Vode, S. Malej, and J. Burja, “Nitrides and carbides in 2101 lean duplex stainless steel,” *Materials and technology*,

vol. 52, no. 6, pp. 821–826, 2018.

[148] M. Atapour, I. Odnevall Wallinder, and Y. Hedberg, "Stainless steel in simulated milk and whey protein solutions – Influence of grade on corrosion and metal release", *Electrochimica Acta*, vol. 331. Elsevier Ltd, 2020.

[149] Outokumpu Oyj., "Duplex and high-strength stainless steels," *Outokumpu Forta range datasheet*, pp. 1–16, 2016.

[150] L. H. Lin, S. C. Chen, C. Z. Wu, J. M. Hung, and K. L. Ou, "Microstructure and antibacterial properties of microwave plasma nitrided layers on biomedical stainless steels," *Applied Surface Science*, vol. 257, no. 17, pp. 7375–7380, 2011.

[151] E. Broitman and L. Hultman, "Adhesion improvement of carbon-based coatings through a high ionization deposition technique," *Journal of Physics: Conference Series*, vol. 370, no. 1, 2012.

[152] ASTM G102, "Standard Practice for from Electrochemical Measurements," *A*STM, vol. 89, no. Reapproved 2015, pp. 1–7, 2015.

[153] N. Perez, "Electrochemistry and Corrosion Science", *Second Edition. Springer*, 2016.

[154] A. de Albuquerque Vicente, I. L. dos Santos, A. B. Botelho Junior, D. C. Romano Espinosa, and J. A. Soares Tenorio, "Study of the Distribution of Cr, Mo, Ni and N in δ Ferrite and Austenite in Duplex Stainless Steels," *Saudi Journal of Engineering and Technology*, vol. 05, no. 04, pp. 156–162, 2020.

[155] Y. Huang and B. Young, "Mechanical properties of lean duplex stainless steel at post-fire condition," *Thin-Walled Structures*, vol. 130, no. June 2017, pp. 564–576, 2018.

[156] W. Dou, "Surface Modification of Lean Duplex Stainless Steels by Low Temperature Plasma Nitriding," *Master Thesis, University of Birmingham*, 2014.

[157] J. Yan, T. Gu, S. Qiu, J. Wang, J. Xiong, and H. Fan, "Phase Transformations During the Low-Temperature Nitriding of AISI 2205 Duplex Stainless Steel," *Metallurgical and Materials Transactions B*, vol.

46, no. 3, pp. 1461–1470, 2015.

[158] J. Wang, Y. Lin, Q. Zhang, D. Zeng, and H. Fan, “Effect of treatment time on the microstructure of austenitic stainless steel during low-temperature liquid nitrocarburizing,” *Metallurgical and Materials Transactions A*, vol. 45, no. 10, pp. 4525–4534, 2014.

[159] D Liu, G X Wu and L X Shen, “Effect of QPQ nitriding time on microstructure and wear resistance of SAF2906 duplex stainless steel,” *IOP Conf. Series: Materials Science and Engineering*, vol. 755, no. 1, 2017.

[160] K. Taherkhani and M. Soltanieh, “Investigation of nanomechanical and adhesion behavior for AlN coating and AlN/$Fe_{2-3}N$ composite coatings created by Active Screen Plasma Nitriding on Al 1050,” *Journal of Alloys and Compounds*, vol. 783, no. April, pp. 113–127, 2019.

[161] W. R. de Oliveira, B. C. E. S. Kurelo, D. G. Ditzel, F. C. Serbena, C. E. Foerster, and G. B. de Souza, “On the S-phase formation and the balanced plasma nitriding of austenitic-ferritic super duplex stainless steel,” *Applied Surface Science*, vol. 434, pp. 1161–1174, 2018.

[162] Y. Liu, B. Rath, M. Tingart, and J. Eschweiler, “Role of implants surface modification in osseointegration: A systematic review,” *Journal of Biomedical Materials Research Part A*, vol. 108, no. 3, pp. 470–484, 2020.

[163] Aleksandra Kocijan, Marjetka Conradi and Matej Hoˇcevar, “The Influence of Surface Wettability and Topography on the Bioactivity of TiO_2 / Epoxy Coatings on AISI 316L Stainless Steel,” *Materials*, 2019.

[164] E. Zhang, X. Zhao, J. Hu, R. Wang, S. Fu, and G. Qin, “Antibacterial metals and alloys for potential biomedical implants,” *Bioactive Materials,* vol. 6, no. 8, pp. 2569–2612, 2021.

[165] I. Ebrahimzadeh, F. Ashrafizadeh, and B. Sadeghi, “Scratch and indentation adhesion characteristics of multilayered PVD coatings before and after the heat treatment deposited by duplex process,” *Surface Topography: Metrology and Properties.*, vol. 7, no. 4, 2019.

[166] Y. Kayali and S. Taktak, “Characterization and Rockwell-C adhesion properties of chromium-based borided steels,” *Journal of Adhesion Science*

and Technology, vol. 29, no. 19, pp. 2065–2075, 2015.

[167] W. Ye and X. S. Tong, "Effect of Atmosphere Proportion and Nitriding Time on Plasma Nitriding of Duplex Stainless Steel," *Advanced Materials Research*, vol. 1061–1062, pp. 61–64, 2014.

[168] T. Bellezze, G. Giuliani, and G. Roventi, "Study of stainless steels corrosion in a strong acid mixture. Part 1: cyclic potentiodynamic polarization curves examined by means of an analytical method," *Corrosion Science*, vol. 130, pp. 113–125, 2018.

[169] J. C. De Lacerda, L. C. Cândido, and L. B. Godefroid, "Effect of volume fraction of phases and precipitates on the mechanical behavior of UNS S31803 duplex stainless steel," *Int. J. Fatigue*, vol. 74, no. 2015, pp. 81–87, 2015.

[170] B. Rahmati, Ahmed. A.D. Sarhan, E. Zalnezhad, Z.Kamiab, A. Dabbagh, D. Choudhury, W.A.B.W.Abas, "Development of tantalum oxide (Ta-O) thin film coating on biomedical Ti-6Al-4V alloy to enhance mechanical properties and biocompatibility," *Ceramics International*, vol. 42, no. 1, pp. 466–480, 2016.

[171] R. Alias, R. Mahmoodian, K. Genasan, K. M. Vellasamy, M. Hamdi Abd Shukor, and T. Kamarul, "Mechanical, antibacterial, and biocompatibility mechanism of PVD grown silver–tantalum-oxide-based nanostructured thin film on stainless steel 316L for surgical applications," *Materials Science & Engineering C*, vol. 107, p. 110304, 2020.

[172] M. Li, H. Cui, H. Wang, Z. Wang, and Y. Liu, "Performance Differences of Ta_2O_5 Films under Different Magnetron Sputtering Conditions," *Advances in Engineering, vol. 126, 5th International Conference on Machinery, Materials and Computing Technology (ICMMCT*), pp. 920–923, 2017.

[173] Y. Y. Chang, H. L. Huang, H. J. Chen, C. H. Lai, and C. Y. Wen, "Antibacterial properties and cytocompatibility of tantalum oxide coatings," *Surface & Coatings Technology*, vol. 259, no. PB, pp. 193–198, 2014.

[174] H. Moreira, A. Costa-Barbosa, S. M. Marques, P. Sampaio, and S.

Carvalho, “Evaluation of cell activation promoted by tantalum and tantalum oxide coatings deposited by reactive DC magnetron sputtering,” *Surface & Coatings Technology*, vol. 330, no. September, pp. 260–269, 2017.

[175] H. J. Farhan, R. K. Jassim, and L. Thair, “Deposition of Ta_2O_5 film on commercial pure titanium disk by modified reactive plasma sputtering technique,” *Medico-Legal Update*, vol. 20, no. 1, pp. 1036–1041, 2020.

[176] B. Rahmati, E. Zalnezhad, A. A. D. Sarhan, Z. Kamiab, B. Nasiri Tabrizi, and W. A. B. W. Abas, “Enhancing the adhesion strength of tantalum oxide ceramic thin film coating on biomedical Ti-6Al-4V alloy by thermal surface treatment,” *Ceramics International*, vol. 41, no. 10, pp. 13055–13063, 2015.

[177] V. Huynh, N. K. Ngo, and T. D. Golden, “Surface Activation and Pretreatments for Biocompatible Metals and Alloys Used in Biomedical Applications,” *International Journal of Biomaterials*, vol. 2019. 2019.

[178] A. P. Manso, F. F. Marzo, X. Garicano, C. Alegre, A. Lozano, and F. Barreras, “Corrosion behavior of tantalum coatings on AISI 316L stainless steel substrate for bipolar plates of PEM fuel cells,” *International Journal of Hydrogen Energy*, vol. 45, no. 40, pp. 20679–20691, 2020.

[179] D. Bernoulli, U. Müller, M. Schwarzenberger, R. Hauert, and R. Spolenak, “Magnetron sputter deposited tantalum and tantalum nitride thin films: An analysis of phase, hardness and composition,” *Thin Solid Films*, vol. 548, pp. 157–161, 2013.

[180] Y.-W. Baik, Sung-Il Kim, “Microstructural evolution of tantalum nitride thin films synthesized by inductively coupled plasma sputtering,” *Applied Microscopy*, vol. 50, no. 1, 2020.

[181] K. Babaei, A. Fattah-alhosseini, H. Elmkhah, and H. Ghomi, “Surface characterization and electrochemical properties of tantalum nitride (TaN) nanostructured coatings produced by reactive DC magnetron sputtering,” *Surfaces and Interfaces*, vol. 21, no. September, p. 100685, 2020.

[182] H. Cao, F. Meng, and X. Liu, “Antimicrobial activity of tantalum oxide coatings decorated with Ag nanoparticles,” *Journal of Vacuum Science &*

Technology A, vol. 34, no. 4, p. 04C102, 2016.

[183] A. Panda, A. K. Sahoo, and A. K. Rout, "Multi-attribute decision making parametric optimization and modeling in hard turning using ceramic insert through grey relational analysis: A case study," *Decision Science Letters*, vol. 5, no. 4, pp. 581–592, 2016.

[184] S. Kumar, B. Mitra, and N. Kumar, "Application of GRA method for multi-objective optimization of roller burnishing process parameters using a carbide tool on high carbon steel (AISI-1040)," *Grey Systems: Theory and Application.*, vol. 9, no. 4, pp. 449–463, 2019.

[185] M. Hrairi, J. I. Daoud, and F. Zakaria, "Optimization of incremental sheet metal forming process using grey relational analysis," *International Journal of Recent Technology and Engineering (IJRTE),* vol. 7, no. 6, pp. 246–252, 2019.

[186] H. H. Hlail and S. H. Al-Shafaie, "Multi-Response Optimization of Mechanical Properties of Al reinforced by Al_2O_3 and/or SiC using Grey Relational Analysis," *IOP Conference Series: Materials Science and Engineering*, vol. 671, no. 1, 2020.

[187] H. Al-Ethari, S. Abbas, and E. K. Zamel, "Optimization of Manufacturing Titanium-Magnesium alloy for Biomaterial Applications using Grey Relational Analyses," *IOP Conference Series: Materials Science and Engineering*, vol. 1094, no. 1, p. 012148, 2021.

Appendix A

Micro Hardness values of nitrided LDX 2101 samples

Sample no.	HV_1	HV_2	HV_3	HV_4	HV_5	HV_{av}
R	241.5	270.1	268.3	254.8	269.7	260.8
1_{5hrs}	874	707.7	770.4	738.1	835	785.04
2_{10hrs}	963.3	944.3	926	923.4	915.7	934.54
3_{15hrs}	1041.9	1166.2	1207.5	1292.7	1275.8	1196.82
4_{20hrs}	920.8	977.1	1011.7	1032.7	1057.5	999.96
5_{25hrs}	1035.8	918.3	903.2	980.5	1083	984.16

Appendix B

Micro Hardness values of sputtered LDX 2101 samples with Tantalum Oxide

Sample no	HV1	HV2	HV3	HV4	HV5	HV_{av}
R	241.5	270.1	268.3	254.8	269.7	260.8
6_{2hrs}	283.5	317.4	284.4	282.2	287.3	290.96
7_{4hrs}	330.8	307.3	420.9	311.7	325.3	339.2
8_{6hrs}	391.9	427.2	399.9	415.8	422.6	411.48
9_{8hrs}	608.1	511.5	525.7	598.4	577.7	564.28
10_{10hrs}	577.4	592.3	553.9	598.5	620.2	588.46

Appendix C

Micro Hardness values of sputtered LDX 2101 samples with Tantalum Nitride

Sample no.	HV1	HV2	HV3	HV4	HV5	HVav
R	241.5	270.1	268.3	254.8	269.7	260.8
11 $_{2hrs}$	310	306.5	299.5	311.7	314.9	308.52
12 $_{4hrs}$	498.9	501.56	515.2	523	521.67	512.066
13 $_{6hrs}$	728.99	750.01	739.32	746.83	748.21	743.51
14 $_{8hrs}$	960.1	930.75	935.05	927.16	929.41	936.494
15 $_{10hrs}$	850.23	860.1	859.4	862.02	858.43	858.036

Appendix D

Elements Percent of nitrided layer on LDX 2101 DSS.

No.	Condition	Fe%	Cr%	O%	N%	Ni%
A	5 hrs	66.6	20.83	8.15	2.87	1.50
B	10 hrs	65.72	20.16	9.40	2.89	1.85
C	15 hrs	53.96	16.35	23.71	3.60	2.38
D	20 hrs	52.92	17.30	21.53	4.59	3.66
E	25 hrs	66.35	22.76	5.60	2.54	2.75

Appendix E

Elements Percent of Ta_2O_5 coating on LDX 2101 DSS.

No.	Condition	Fe%	Cr%	O%	Ni%	Ta%
A	2 hrs	2.13	0.46	31.17	0.31	65.94
B	4 hrs	2.10	0.59	30.86	0.29	66.15
C	6 hrs	2.44	0.43	30.36	0.32	66.46
D	8 hrs	0.67	0.33	34.31	0.50	64.19
E	10 hrs	1.34	0.42	33.65	0.64	63.95

Appendix F

Elements Percent of TaN coating on LDX 2101 DSS**.**

No.	Condition	Fe%	Cr%	O%	Ta%	N%
A	2 hrs	3.49	1.18	44.25	7.63	43.45
B	4 hrs	3.27	1.17	44.85	4.27	46.43
C	6 hrs	3.14	1.07	44.65	3.83	47.32
D	8 hrs	2.64	0.81	44.56	7.13	44.87
E	10 hrs	2.16	0.61	43.81	10.51	42.91

Appendix G

جمهورية العراق

وزارة التخطيط
الجهاز المركزي للتقييس والسيطرة النوعية

العدد : ٤٢٢٤
التاريخ م : ٧/١٠/٢٠٢١
هـ : / /

رئاسة الجهاز
مديرية براءات الاختراع والنماذج الصناعية
القسم الاداري

العراق يقرأ (٢٠٢١)

الى / جامعة بابل / كلية هندسة المواد

م/ تـــأييـــد

يهدي الجهاز أطيب تحياته .....
نؤيـــد استلام طلب براءة الاختـــراع المرقم (٥٢٥/ ٢٠٢١) في ٢٠٢١/١٠/٧ والموســـوم :
(تعديل الخواص السطحية للفولاذ المقاوم للصدأ المزدوج في التطبيقات الطبية)
والمودع من قبل السادة المدرجة اسمائهم في ادناه :

١- م٠ نسرين داخل فهد
جامعة الكوفة / كلية الهندسة / قسم هندسة المواد
٢- ا٠د٠ جاسم محمد سلمان
جامعة بابل / كلية هندسة المواد / قسم هندسة المعادن
٣- ا٠د٠ علي سبع حمود (متوفي)
جامعة الكوفة / كلية الهندسة / قسم هندسة المواد

وحالياً قيد اجراءات الفحص والتقييم، وبناء على طلبهم زودناهم بهذا التأييد

مـــع التقـــدير

نعيم احمد اسماعيل
مدير القسم الاداري
ع/ مسجل براءات الاختراع والنماذج الصناعية
٢٠٢١/١٠/

صورة منه الى /
- م٠ نسرين داخل فهد / جامعة الكوفة / كلية الهندسة / قسم هندسة المواد ٠٠٠٠مع التقدير
- مديرية براءات الاختراع والنماذج الصناعية/ القسم الفني /للحفظ في اضبارة الطلب اعلاه

العراق - بغداد - الجادرية - ص . ب (١٣٠٣٢) - البريد الالكتروني : www.cosqc.gov.iq
هاتف ٨٤ / ٨٣ / ٨٢ / ٨١ / ٧٧٨٥١٨٠ تليفاكس ٧٧٦١٩٨١ cosqc@cosqc.gov.iq

الخلاصة

سبيكة (LDX 2101) من سبائك الفولاذ المقاوم الصدأ ذات محتوى كروم (21%) ونيكل (1%) تمتاز بخصائص ميكانيكية قوية ومقاومة تآكل جيدة وتطبيقات صناعية شتى، أعطت نسبة النيكل المنخفضة لهذه السبيكة ميزة طبية إيجابية (اقل من الفولاذ المقاوم للصدأ 316L) لان كمية ايونات النيكل السامة المنبعثة داخل جسم الانسان ستكون منخفضة، إضافة الى كلفتها المنخفضة نسبيا (حيث تعتبر من أرخص أنواع الفولاذ المقاوم للصدأ لقلة عناصر السبك الموجودة في السبيكة وبضمنها النيكل الباهظ الثمن).

ان ضعف الالتحام العظمي في انسجة العظام وما يترتب من ذلك من مخاطر التلامس السطحي ما بين الغرسة المعدنية وسوائل جسم الانسان يؤدي الى تآكل شديد وحاد. ولتجاوز هذه المحددات تم في هذه الاطروحة اجراء معاملات سطحية مختلفة على السبيكة المذكورة ثم دراسة تأثير نوع المعاملة السطحية ومتغيرات تلك المعاملة على تحسين الخواص الميكانيكية وخواص السطح والتوافقية الحياتية والاندماج العظمي والنشاط ضد البكتريا ومقاومة الالتصاق ومقاومة التآكل للطبقة السطحية المتكونة نتيجة لتلك المعاملات السطحية وتحديد القيم المثلى لتلك المتغيرات.

تم استخدام ثلاث معاملات تعديل سطحي لسبيكة الفولاذ المقاوم الصدأ المزدوج (LDX 2101 DSS) وبظروف مختلفة لكل معاملة، تقنية النتردة بالبلازما عند فولتية (400) فولت وتيار (30) ملي امبير مع ازمان (5,10,15,20,25) ساعة وترسيب أوكسيد التنتالوم بتقنية الترذيذ بالبلازما عند فولتية (3500) فولت وتيار (10) ملي امبير مع ازمان (2,4,6,8,10) ساعة وترسيب نتريد التنتالوم بتقنية الترذيذ بالبلازما عند فولتية (3500) فولت وتيار (10) ملي امبير وازمان (2,4,6,8,10) ساعة.

تم دراسة الخصائص الميكانيكية للطبقة السطحية باستخدام اختبار صلادة فيكرز الميكروي، اما الخصائص السطحية تم دراستها بالمجهر الالكتروني الماسح ومجهر القوة الذرية إضافة الى فحص التركيب الكيمياوي لتوزيع العناصر الموجودة في سطح الطبقة المتكونة باستخدام التحليل الطيفي للطاقة المشتتة اما الاطوار المتكونة نتيجة المعاملات السطحية على الطبقة المتكونة تم تحليلها بواسطة حيود الاشعة السينية.

بعد ذلك تم دراسة اختبار الطبقة السطحية في مقاومتها للبكتريا الضارة وأيضا تم اختبار مقاومتها للالتصاق. وأخيرا تم دراسة سلوك العينات المعاملة سطحيا في المائع المحاكي لجسم الانسان (Ringer solution) باستخدام اختبارات جهد الدائرة المفتوحة والاستقطاب الديناميكي الكهروكيمياوي الحركي والدوري.

اظهرت النتائج تحسنا بنسبة (65%, 52%, 85%) في قيم الصلادة لكل العينات المعاملة سطحيا. وبينت صور المجهر الالكتروني الماسح تكوين طبقة سطحية ذات بنية متماسكة كثيفة وخالية من الشقوق او العيوب. أوضحت نتائج فحص حيود الاشعة السينية ومجهر المسح الالكتروني تكوين اطوارا معدنية جديدة في الطبقة السطحية (S, Ta_2O_5, TaN) وعدم وجود تحلل طوري مما يشير الى ان ظروف المعاملة السطحية كانت جيدة.

نتائج مجهر القوة الذري أوضحت زيادة في قيم الخشونة السطحية للعينات المعاملة سطحيا مع زيادة زمن المعاملة.

أوضحت نتائج فحص السلوك المضاد للبكتيريا مع سلالات بكتريا E.Coli، ان الطبقة المترسبة من المعاملات السطحية لها تأثير قوي مضاد لمنع نمو البكتيريا. اما نتائج اختبار مقاومة الالتصاق أوضحت ان الطبقة المترسبة لكل أنواع المعاملات السطحية المستخدمة لها قوة التصاق مقبولة.

نتائج منحنيات الاستقطاب أظهرت زيادة في مقاومة التآكل للعينات المعاملة سطحيا مقارنة مع العينات غير المعاملة حيث كشفت النتائج أن أفضل حالة نتردة بالبلازما كانت عن زمن (10) ساعة حيث تمتلك الطبقة المنتردة أقل معدل تأكل (0.057 mpy) في محلول رينجر، بينما كانت أفضل حالة لترسيب أوكسيد التنتالوم بتقنية الترذيذ بالبلازما كانت عند زمن (8) ساعة حيث تمتلك الطبقة المترسبة اقل معدل تآكل (0.0492 mpy)، من ناحية أخرى كانت أفضل حالة لترسيب نتريد التنتالوم بتقنية الترذيذ بالبلازما عند زمن (8) ساعة حيث تمتلك الطبقة المترسبة اقل معدل تأكل (0.02 mpy).

وأخيرا تم استخدام طريقة (grey relational analyses) لتحديد أمثل الظروف للمعاملات السطحية (نوع المعاملة السطحية، فولتية، تيار، زمن) والاستجابة (معدل التآكل، سمك الطبقة السطحية، صلادة فيكرز، الخشونة السطحية). ولإنجاز هذه الدراسة تم استخدام برنامج (Minitab17 Microsoft). تم تسجيل التجربة 14، التي تمتلك معاملة سطحية هي ترسيب نتريد التنتالوم بتقنية الترذيذ بالبلازما وزمن (8) مع فولتية (3500) فولت وتيار (10) ملي امبير هي القيم المثالية لعوامل الاستجابة.

المعاملات والتعديلات السطحية التي تم استخدامها لتطوير السبيكة (LDX 2101 DSS) الفولاذ المقاوم للصدأ المزدوج في الخواص الميكانيكية والسطحية ومقاومة التآكل ستفي بالمتطلبات المستقبلية لتطبيق السبيكة كمنافس قوي وبديل بالتطبيقات الطبية الحيوية بتقويم العظام.

جمهورية العراق

وزارة التعليم العالي والبحث العلمي

جامعة بابل

كلية هندسة المواد

قسم هندسة المعادن

التعديل السطحي للفولاذ المقاوم للصدأ المزدوج LDX 2101 في التطبيقات الطبية الاحيائية

اطروحة مقدمة إلى مجلس كلية هندسة المواد/ جامعة بابل

وهي جزء من متطلبات نيل درجة الدكتوراه فلسفة في

هندسة المواد/ هندسة المعادن

اعدت من قبل الطالبة

نسرين داخل فهد دلي

بإشراف

أ.د. جاسم محمد سلمان **أ.د. علي سبع حمود**

1442 هـ **2021 م**